Rapid Granular Flows in an Inclined Chute

Alexander James Holyoake

This dissertation is submitted
for the degree of Doctor of Philosophy

December 2011

Trinity College
and
Department of Applied Mathematics and Theoretical Physics
University of Cambridge

This document is the result of my own work and includes nothing which is the outcome of work done in collaboration, except where specifically indicated in the text. No part of this dissertation has been submitted for any other qualification.

Alexander James Holyoake

Rapid Granular Flows in an Inclined Chute

Alexander James Holyoake

Abstract

The aim of this thesis is to investigate the flow of granular materials on steep slopes. These occur naturally as snow avalanches and rock slides and are also important industrially. The flow of grains down inclined planes has been widely studied but nearly all work has focussed on relatively low slope angles where steady, fully developed flows occur after a short distance. Nearly all granular flow models have a maximum value for the friction and therefore predict flows on steeper slopes will accelerate at a constant rate until the interaction with the ambient fluid becomes important. This thesis tests this prediction by investigating flows over a much greater range of slope angles. We perform chute flow experiments on steep slopes with two different basal conditions, one smooth and one rough. We report on dense flows that are steady in time and are from 4 to 130 particle diameters in depth on slopes ranging from 30° to 50°. Though these flows do not vary in time, all but the flows on the rough base at the lowest inclinations accelerate down the chute. A recirculation mechanism sustains flows with a maximum mass flux of $20\,\mathrm{kg\,s^{-1}}$, allowing observations to be made at multiple points for each flow over an indefinite period. Flows with Froude number in the range 0.1–25 and bulk inertial number 0.1–2.7 were observed in the dense regime, with surface velocities in the range 0.2–$5.6\,\mathrm{m\,s^{-1}}$. Previous studies have focussed on $I \lessapprox 0.5$. We numerically solve a rheology that is qualitatively sucessful at modelling equilibrium flows (Jop, Forterre & Pouliquen, 2006, *Nature*, **441**, 167-192) and find a generally poor agreement with our experimental data. Our data does not suggest that there is a maximum value of friction, but that steady flows may be possible on much steeper slopes than previously realized.

We also observe a transverse inelastic collapse of the flow, which is investigated using Lun's kinetic theory with appropriate boundary conditions. This theory has sucessfully predicted Rayleigh-Bénard type longitudinal vortices. We also observe these in our experiments and a transition to an unstable, possibly turbulent dilute regime, which are left as subjects for possible future study.

Acknowledgements

The work presented in this thesis would not have been possible without the support of the G.K. Batchelor laboratory group. I am particularly indebted to my doctoral supervisor Jim McElwaine for his advice and patience over the last few years. He has taught me to look at the big picture whenever possible instead of becoming focused on a multitude of small problems. It is perhaps regrettable that I wasn't able to spend more time investigating the maths behind the phenomena rather than solving problems essentially technical in nature.

I also owe a large debt of gratitude to Stuart Dalziel for his technical guidance and for always making himself available for solving lab and mathematical problems. I would also like to thank Colm-cille Caulfield for helpful chats about matters other than experiments.

Ioanna Vlahou has been a constant help over the last few years, from regular technical discussions to proof reading, catering and helping to keep me sane. I would also like to thank my office mates, especially Imran Coomaraswamy and Rosie Oglethorpe who have always been on hand for help with the odd laboratory and MATLAB problem.

I am grateful to the DAMTP technicians, David Page-Croft, John Milton, Neil Price, Colin Hitch, Trevor Parkin and Rob Raincock, without whom the chute would not have been built and evolved into the state that it is in today.

Lastly, I would like to thank the National Environment Research Council for my doctoral research grant, the Engineering and Physical Sciences Research Council for funding the construction of the equipment, as well as Trinity College and DAMTP for their support.

AJH

Contents

List of Figures

List of Tables

1

Introduction

1.1 Motivation

Granular matter has fascinated the minds of many since ancient times. Indeed, Archimedes (circa 200 B.C.) calculated the number of grains of sand that would fill the universe as he knew it, producing the oldest research paper for which we still have proof of existence. Some one hundred years later Lucretius, the Latin philosopher was possibly the first to ponder flowing grains:

> *One can scoop up poppy seeds with a ladle as easily as if they were water and, when dipping the ladle the seeds flow in a continuous stream...*
>
> (Lucretius, tr. Duran, 2000)

Indeed, throughout history granular materials have played a significant role in daily life. The age-old processes of farming, mining and construction each deal

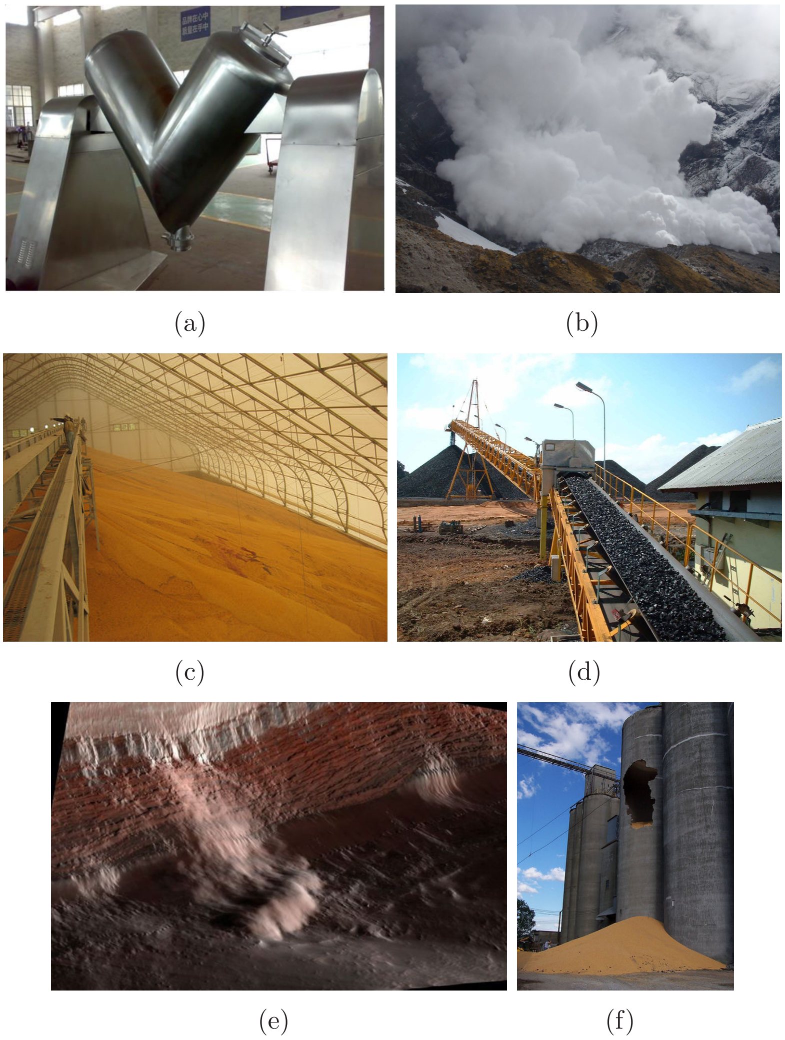

Figure 1.1: *Examples of industrial and geophysical granular processes. (a) V-mixer used to mix two species of particle countering the effects of segregation. (b) Large powder snow avalanche. (c) Transportation of granular materials in a cornshed. (d) Coal conveyor. (e) Martian avalanche. (f) Collapsed grain silo.*

with manufacturing, transporting and manipulating granular materials. Each year in the United States alone, it is estimated that more than one trillion kilograms of granular material are manipulated by the pharmaceutical, food and chemical industries (van Cleef, 1991). Most of these will be transported, poured or mixed and stored in piles, silos or other containers at some point. In fact, the only substance that man manipulates more than granular materials is water (de Gennes, 1999).

Despite the prevalence of granular flows in everyday life, there is still a lack of fundamental understanding of why this class of material behaves as it does. Small gains in the understanding of granular flows can potentially give a significant improvement in how we handle powders and grains on a daily basis. We still manipulate granular materials in often clumsy and dangerous ways — in industry, unwanted small particles that are a by-product of manufacturing can be toxic and explosive. We battle against elements of the granular phenomenology such as segregation in order to avoid structural inhomogeneities in building materials, to make sure our drugs are evenly mixed, and to efficiently transport materials from one place to another.

Granular materials and flows are also ubiquitous in the natural world. Each year approximately 200 people lose their lives due to snow avalanches (Armstrong *et al.*, 1992), and a substantial amount of property is lost to avalanches, debris flows and earthquakes. The American Avalanche Association estimates that of the order of one million snow avalanches fall each year in the world, and the insurance claims by the Swiss alone are of the order of £40 million annually, with the capital invested for direct and indirect prevention many times higher. With the combination of increased population pressure in areas of high avalanche risk, and the melting of permafrost, which may increase the likelihood of avalanches occurring, understanding these flows has never been more important. Effective defences can save lives as well as provide a substantial economic benefit.

Natural granular flows are not limited to snow avalanches and debris flows. They are also found in submarine avalanches (Klaucke *et al.*, 2004) and potentially devastating volcanic ash flows such as the Mount St. Helens eruption in 1980 Voight *et al.* (1985). This released $2.5\,\mathrm{km}^3$ of material killing 60 people, spreading widespread destruction with an estimated ultimate cost of around 1 billion USD.

These flows can also be found extraterrestrially, examples of which are interstellar dust clouds and Martian avalanches (Treiman & Louge, 2004).

Even in the area of space exploration, the importance of granular materials should not be underestimated. Any objects landing on a planet must know how to deal with the technological challenges that the granular surface may present (Louge, 2009; Treiman & Louge, 2004).

1.2 Complexity

Even a cursory glance at the granular literature reveals that the field is in a state of flux. Real granular flows can be subject to a plethora of complicating forces. These include adhesion, cohesion, van der Waals forces, magnetic forces and capillary forces from the interstitial fluid. Indeed, even without any of these effects, the description of a dry, cohesionless granular material still represents a challenge and the question of which equations should be used in a given situation is still controversial. Many phenomena remain unexplained by any model. As such, in this thesis we restrict our analysis to large particles such that electrostatics have a negligible influence and the case where moisture and interstitial fluids do not affect the dynamics.

A naïve first look at the physics of dry granular materials suggests that they should be simple to analyse — they are assemblies of large, macroscopic particles with no cohesive forces. Yet, despite this apparent simplicity granular materials remain poorly understood.

A number of effects complicate the use of traditional continuum thermo- and hydro-dynamical principles. A lack of separation of scales between typical flow lengths and the size of the constitutive particles means that continuum models often cannot capture important regions where the flow is thin. The inelasticity of the particles causes dissipation which means that a normal thermodynamical energy balance involving a temperature does not exist. As the important length scale in granular flows is the particle diameter d , which typically is of the order 10^{-6}–$10^{-3}\,\mathrm{m}$, the relevant energy scale is given by the energy required to raise the particle by a diameter or so, i.e $mgd \sim 10^{-11}$ J for sand. In contrast, the thermodynamic energy (at room temperature) $kT \sim 10^{-21}$ J (where k is the Boltzmann constant), which is 10 orders of magnitude smaller than the potential energy scale. Since inelasticity renders any thermal motion unimportant when compared to the dynamical forces acting on the grains, the system can be considered athermal. The lack of a temperature distribution means that the particles are unable to explore the phase space and arrive at a ground state in the same way as a conventional gas or liquid. This can be observed when pouring sand onto a flat surface: the ground state of the system occurs when the potential energy is minimised, i.e. when the particles form a monolayer. However, with granular matter this ground state will not be reached unless external forces are applied and therefore the pile of granular material can exist indefinitely. Moreover, the angle of the slope that the pile forms can take one of many values, indicating that this process is not only metastable, but also multistable. As a result, as each configuration of particles has its own unique properties, repeatability of granular flows are often difficult to achieve, especially for flows near the static threshold. The lack of thermodynamic equilibrium means that standard entropic arguments, which usually facilitate mixing, are no longer valid and are easily outweighed by dynamical effects. As a result, we see phenomena such as segregation occurring whereby typically larger particles in a mixture of granular species will float to the top when subjected to some kind of agitation and therefore sees a decrease in entropy. An example of this effect can be seen in figure 1.2 where flow is self-agitated by shearing in a thin layer on the free surface.

In fact, it is an open question in the study of granular physics if a single set of constitutive relations will ever capture the wide spectrum of granular behaviours. As a result, granular physicists do not have the same framework as fluid dynamicists, who can exploit the ubiquitous and well-tested Navier-Stokes equations. Depending on the mode of deformation, granular material can behave as a gas, liquid or solid. Indeed, all three phases can exist in a flow simultaneously and the distinction between the three is not well-defined. Figure 1.3 shows the flow of ball bearings on a pile and serves well to introduce the three main phases of granular materials.

It can be seen that the particles at the free surface of the flow form a dilute

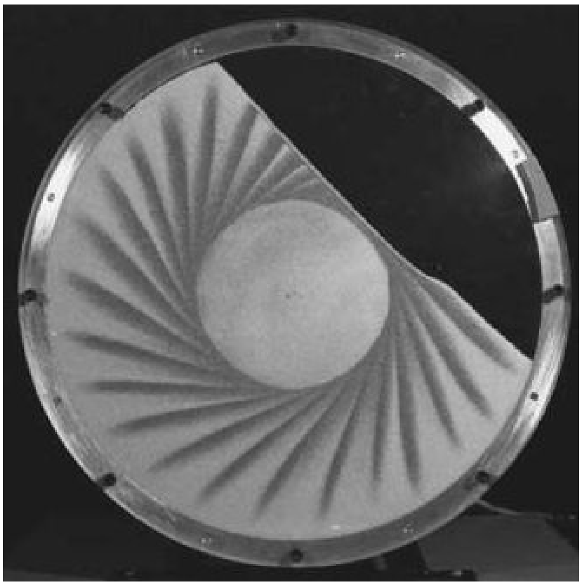

Figure 1.2: *Shear-induced segregation in a rotating drum. White particles are larger than the dark ones. The dynamics in the drum are also affected by the hysteresis of granular flows via the avalanche instability, and the propagation of a shock up the interface as the flow arrests. Reproduced from Gray & Thornton (2005).*

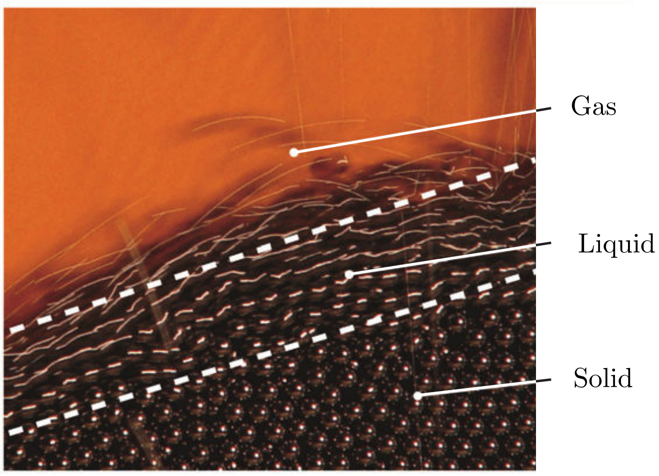

Figure 1.3: *A flow with the gaseous, fluid and solid phases of granular motion present. Reproduced from Forterre & Pouliquen (2008).*

layer, and the lack of cohesive forces between particles has led to an analogy with a molecular gas (Lun *et al.*, 1984), taking inspiration from the dense gas theory of Chapman & Cowling (1939). This assumes that the particles interact through instantaneous binary collisions as the diluteness of the particles makes the probability of multi-body collisions vanishingly small. We say that a granular medium in this mode of deformation is in the *kinetic regime*. A kinetic theory can be derived for granular materials and could be used to derive constitutive relations for this peculiar material. We can do so by defining a *granular temperature*, which is a measure of the fluctuations of the particles' velocity about their mean (Lun *et al.*, 1984; Campbell, 1990). However, the inelasticity of the particles complicates the situation significantly, as it leads to the dissipation of energy and condensation of the gas, unless energy is continually supplied to the ensemble and therefore the standard thermo- and hydro-dynamic laws are some what modified.

At the base of the flow in figure 1.3, the flow is very slow and the dynamics are governed by enduring contacts and force chains, caused primarily by the inter-particle friction. As such, a granular material deforming in this way behaves much like a plastic solid. Although for static assemblies of granular materials under very low shear, the assembly responds as an elastic solid (Brown & Richards, 1970). This is in contrast to the dominant transfer mechanism of binary collisions of the kinetic regime. A visualisation of the force chains in a system can be seen in figure 1.4, which uses a monolayer of photo-elastic particles which are placed under compression. These force chains span the entire system, indicating that a local rheology may not be capable of accurately capturing the assembly's behaviour. It also indicates a strong heterogeneity in the system. The difficulty in emptying granular media from containers can primarily be attributed to these force chains bridging over the aperture, causing flow to stop altogether and jamming the system.

For higher shear rates, the solid exhibits a yield stress which is typical of a Coulombic nature (de Coulomb, 1773), where the shear stress in a given direction $|\tau|$ is proportional to the normal stress $|p|$, and yields when the criterion

$$|\tau| = \mu|p| \tag{1.1}$$

is met for some value of μ. This phase of granular materials has been studied in

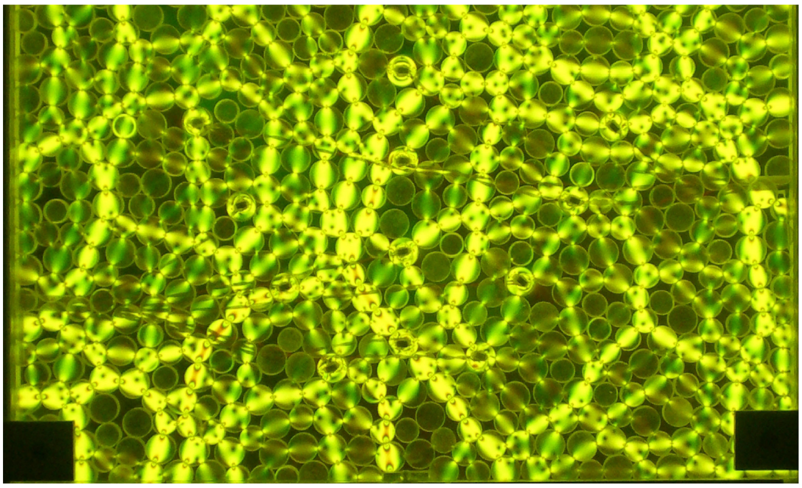

Figure 1.4: *Force chains in a 2D granular assembly of photo elastic particles under compression. The particles consist of an elastic disc with a polarising filter on each face. When the particle is deformed, the filters align allowing light through. Reproduced from Bassett* et al. *(2011).*

depth by the solid mechanics community and is well described by critical-state and plasticity theories (Nedderman, 2005; Schofield & Wroth, 1968). We refer to such slow flows as being in the *creeping* or *quasi-static* regime. In addition to the phases of gas, solid and liquid, grains can also exhibit a slow creeping flow, analogous to a glass (Jaeger *et al.*, 1989). Deep in a granular pile with a flow on its surface there are slow agitations that produce an exponential tail to the velocity profile.

In the region between the kinetic and quasi-static regimes we observe granular material flowing as a liquid. In this case, the interactions between particles are governed by collisions, frictional interactions and geometric entanglement of the particles. This last mechanism can be observed by performing simulations of frictionless particles and noting that the resultant flow is still found to exhibit a macroscopic friction coefficient Denlinger & Iverson (2004). Persistent contacts and force chains can also play a role, as the volume fraction is only slightly less than that of the solid phase. In a broad sense, dense granular flows can be placed in the visco-plastic family of materials, as a flow threshold exists and a shear rate dependence is observed, which gives it a viscous-like behaviour.

This intermediate regime is the one that has been most lacking a satisfactory theoretical explanation, with competing theories each having significant drawbacks. This regime will be the main focus of this thesis. Apart from these difficulties in describing even an ideal granular material theoretically, the experimental verification of these theories is also beset with numerous complicating factors. Micromechanical theories invariably place assumptions on the constitutive particles in order to make any analysis tractable. A canonical example of this is the shape of the particles, which are usually assumed to be mono-disperse and spherical. Even if a source of truly spherical particles could be found, experiments are usually conducted with slightly polydisperse mixtures in order to avoid ordering and crystallisation (a first-order phase transition to an ordered state) which are infrequently seen in natural flows. A disadvantage of this is that the particle diameter, which is one of the important length scales in the problem, is not well defined, making the comparison to theory more difficult. Spherical particles are rare in natural contexts; sand and gravel instead are angular and irregular. Experimental studies typically use either natural sand, which is typically rough and angular, or spherical ballotini. The dynamics of these two types of particles can be strikingly different. For example, the use of monodisperse ballotini in Pouliquen (1999*b*) suppresses a frontal fingering instability as seen in figure 1.5. The shape of the particles is known to have an effect on packing densities (Cho *et al.*, 2006) and can therefore affect the dynamics of the flow. For example, the yield stress needed to break a static pile of ordered grains is known to be higher than that for polydisperse grains Bardenhagen *et al.* (2000).

Other problems with micromechanical models in granular physics are caused by the a high number of material parameters used. These include, but are not limited to, the restitution, tangential restitution and friction caused by asperities on the surface of the grains and particle elasticity. While these can be accounted for theoretically, accurately measuring them presents a significant experimental challenge to the point of being unfeasible and they are usually distributions rather than single numbers. Instead, we typically rely on macroscopically measured parameters that characterise overall behaviour.

The history dependence, or hysteresis of granular materials also presents a difficulty for the experimentalist. The preparation of sand before an experiment is conducted can affect the results greatly. Reynolds (1885) first identified that

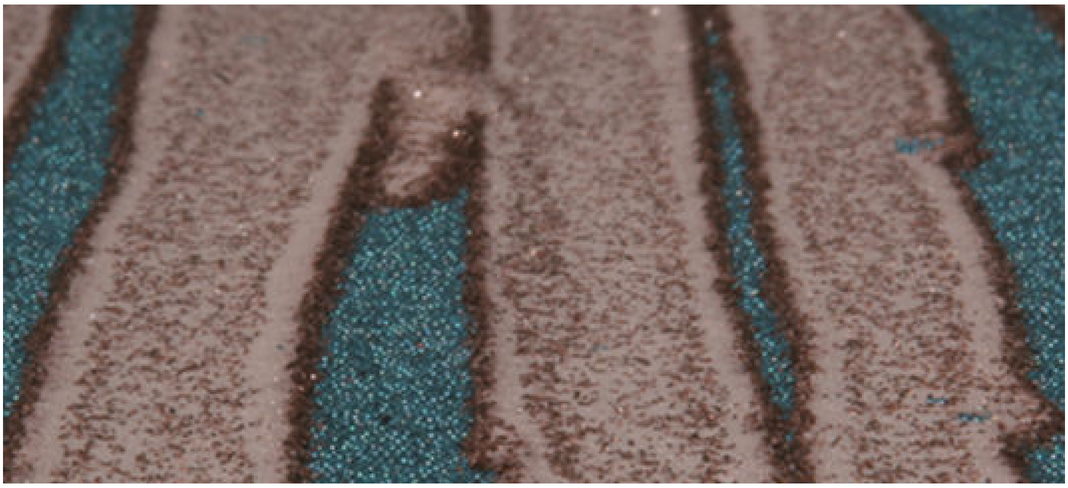

Figure 1.5: *A bidisperse granular avalanche exhibits a frontal instability which evolves into levée-channelized fingers. Also seen is the segregation of the large particles to the edge of the levée. From the Manchester Centre for Nonlinear Dynamics.*

packed grains need to dilate so that they can flow over each other. Indeed, the volume fraction ϕ, i.e. the proportion of space that is occupied by the particles, can greatly affect the dynamics. A mono-dispersed mixture has a theoretical maximum packing of $\phi_{\mathrm{max}} = 0.74$ (face-centred cubic packing) but, in practice, packings no higher than $\phi_{\mathrm{rcp}} \approx 0.64$ (random close packing) are seen. This latter packing can be approached by taking a sample of granular material and vibrating or tapping the sample until it compacts. As this happens, the volume fraction of the material increases as does the yield stress. On the other hand, if a sample is prepared by sprinkling the sand lightly, then a packing fraction of $\phi_{\mathrm{rlp}} \approx 0.56$ (random loose packing) is approached. To reach lower ϕ, we must input energy to the flow and the coordination number (i.e. the average number of particles that an individual grain is in contact with) decreases until we enter the kinetic regime, in which it approaches 0. The need of the grains to dilate before flowing can produce shear localisation in some situations in the form of slip bands which are typically 5–10 particle diameters thick and are largely independent of the flow geometry. Importantly, the flow thresholds are also strongly affected by the boundary conditions and, in general, granular flows exhibit many interesting phenomena when approaching a flow transition. Experimentally, we see that the velocity does not decrease steadily to 0 but slows down and suddenly freezes.

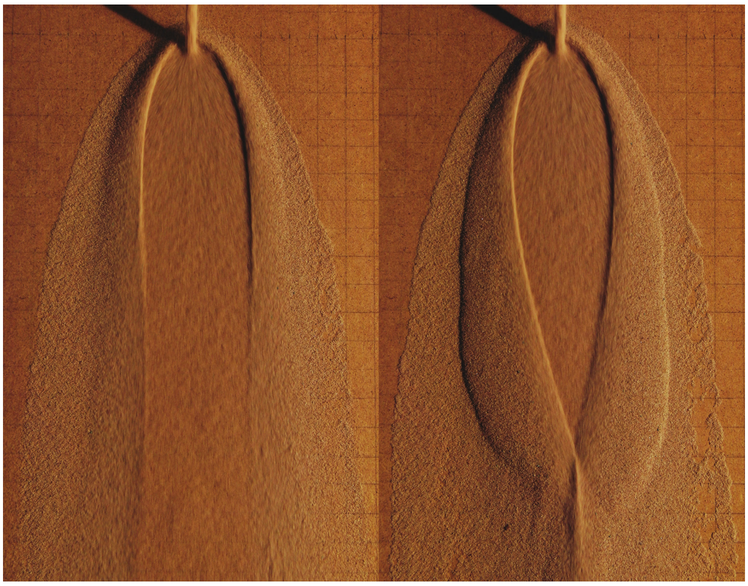

Figure 1.6: *Two behaviours of a granular jet impinging on a rigid, smooth and flat surface. Both exhibit a granular jump above the point of impingement. The second picture also shows a teardrop shaped granular shock. Johnson & Gray (2011)*

This is indicative of the traction at the base weakening as the velocity increases, and is related to the increased strength of the material when it is packed more tightly (Pouliquen, 1999*b*). The ability of the flow to arrest is responsible for a rich variety of phenomena including levée formation and self channelisation of flows (Delannay *et al.*, 2007; Mangeney *et al.*, 2007) as seen in figure 1.5. One major effect of this is that it can serve to increase the run-out of an avalanche.

Dense granular flows have a very rich phenomenology, only a small subset of which is mentioned here. Other effects include shocks or jumps (see figure 1.6), interfacial Kapitza waves (Forterre, 2006), roll waves (Forterre & Pouliquen, 2003) and longitudinal vortices (Börzsönyi *et al.*, 2009; Forterre & Pouliquen, 2001) analogous to Rayleigh-Bénard convection, and many more.

1.3 Developments

Although granular materials received some attention prior to the 20$^{\text{th}}$ century, the modern field of granular analysis began with Bagnold (1941), who studied and deduced laws for aeolian transport of sand describing the formation and movement in the Libyan desert. He used collisional arguments to uncover two fundamental relations of granular flows, namely that the shear and normal stresses obey the scalings

$$\tau = \rho_p d^2 f_1(\phi)\dot{\gamma}^2 \quad \text{and} \quad p = \rho_p d^2 f_2(\phi)\dot{\gamma}^2. \tag{1.2}$$

Here, τ is the shear stress in the granular material and p is the particle pressure, while $\dot{\gamma}$ is the shear rate, ϕ the volume fraction, and ρ_p the density of a single particle. The stress on a single particle is proportional to the number of particles hitting it in unit time, multiplied by the momentum change imparted by a single collision. As both of these are proportional to the shear rate, and the projected area over which this momentum transfer happens is proportional to d^2, we recover the forms (for some unknown functions f_i of the non-dimensional ϕ). However, it must be noted that these relations also arise purely through dimensional reasoning, and so hold over a much wider range of circumstances than originally envisioned by Bagnold. It is from this scaling that the *Bagnold profile* of a granular flow in equilibrium gets its name. Such arguments predict that the volume fraction is constant since in a steady flow the shear force must balance the gravitational forcing which gives rise to the relationship

$$\frac{\tau}{p} = \frac{f_1(\phi)}{f_2(\phi)} = \tan\theta. \tag{1.3}$$

In such a flow a hydrostatic balance holds such that the pressure $p \sim z$, the distance from the base. As we have $\dot{\gamma} \sim \partial_z u$, the depth dependence of the velocity profile is given by

$$u(z) = A(\theta, \phi)\sqrt{gd}\left(1 - \left(1 - \frac{z}{h}\right)^{3/2}\right). \tag{1.4}$$

We note that this 3/2 law is in contrast to the parabolic dependence seen for viscous flows. The function A also depends on material parameters and boundary conditions. We shall exploit this profile in our analysis of chute flows in chapter 4.

After Bagnold's seminal work, the field progressed slowly until the 1980s, with the advent of two different kinds of models for dry, cohesionless granular materials.

The first family of models fall under the aforementioned kinetic theory and they attempt to describe dilute granular flows such that the dominant momentum transfer mechanism is through collisions. They are motivated by the traditional stochastically-averaged description of classical gases. The canonical paper for the derivation of this theory is by Lun *et al.* (1984), although the model was also developed independently at a similar time by Jenkins & Savage (1983) and Haff (1983), amongst others. In this model, expressions for the transport of a generic field by collisional means are deduced together using an analogue for the thermodynamic temperature known as the *granular temperature* (Ogawa *et al.*, 1980). This is given by the variation of the grains' velocities about their mean. A key assumption of the theory is that particle interactions are binary and instantaneous, which effectively limits the application of the classic theory to low volume fractions — as the average density increases, multi-body interactions become more common to the point that contacts may persist indefinitely. The pairwise particle distribution function is supplemented with a dense gas correction in the form of the radial distribution function. As mentioned previously, a key difference between granular kinetic theory and the traditional theory is the inelasticity of the particles — any successful theory must take this dissipation into account. It is noted that in order for the kinetic description to be valid to real flows for long times, energy must be supplied to the system or it will condense.

The theory can incorporate a rate-independent stress tensor to include particle–particle friction effects (Johnson *et al.*, 1990; Anderson & Jackson, 1992; Hutter & Rajagopal, 1994) and can qualitatively predict the existence of steady, fully developed flows for a range of inclinations as per the experimental data. One of the major drawbacks is that direct quantitative comparison with experiments is difficult since many parameters introduced in the models are hard to measure reliably, and there is a particular difficulty that arises when attempting to formulate the correct boundary conditions.

A number of extensions to the theory have been made over the years including the effect of particle roughness in two dimensions (Jenkins & Richman, 1985) and the effect of inter-particle friction (Johnson *et al.*, 1990). However, the latest incarnations of the theory extend their applicability to higher volume fractions by assuming an infinite friction between particles and including the tangential restitution into an effective normal restitution. They also introduce a heuristically derived correlation length (Jenkins, 2007; Berzi *et al.*, 2011) which accounts for the overestimation of the inelastic dissipation of the traditional theory at high volume fractions. This approach gives good agreement with experimental results by Jop *et al.* (2005) amongst others, and compensates for the failure of the instantaneous and binary collision assumptions. We use a version of the traditional kinetic theory in chapter 5 to describe a volume fraction variation seen experimentally. We choose to use this as the volume fraction in the sparse regions is low enough for traditional kinetic theory to be applicable in principle.

The second family of models does not rely on micro-mechanical material parameters to describe the flow. Instead, a more phenomenological approach is adopted. Often, these models are framed in terms of depth-integrated equations of motion, much like the shallow water or Saint-Venant equations (de Saint-Venant, 1871). Indeed, one of the first papers to take this approach ignored the internal shear of the material completely (Savage & Hutter, 1989) and so the issue of defining a stress tensor and the form of the rheology was not encountered. These depth-integrated flows rely on the horizontal (slope parallel) variations being much smaller than the vertical (slope normal) variations. We discuss these models and their assumptions in more detail in chapter 4. Although many models have been proposed over the intervening years, we choose to concentrate on a recent model that has had much success in giving good quantitative predictions for steady flows: the $\mu(I)$ rheology proposed by Jop *et al.* (2006). This rheology uses dimensional analysis and data from experiments to give a rheology modelled using a Coulomb friction criterion. We discuss the successes and shortcomings of the $\mu(I)$ rheology in the following chapters.

The addition of computing power to the theoretician's arsenal over the last 20 or so years has proved to be especially beneficial to the field of granular mechanics. The combination of the lack of constitutive relations and the physical opacity of a typical granular flow means that it is particularly hard to infer the behaviour of the internal structure of the flow. Simulations in granular flows fall broadly into two categories. The first is the computation of models with non-trivial boundary conditions, such as the application of a depth-integrated model over a curved terrain (e.g. Pouliquen & Forterre, 2002; Denlinger & Iverson, 2004), and serves primarily as a tool for verifying the model against experimental data. We present such a simulation in chapter 2. The second class of simulations model individual particles and their interactions with each other and the boundary directly, otherwise known as discrete element modelling (DEM). With this class of simulation, we follow the motion of each individual particle, giving direct access to otherwise inaccessible fields such as the internal stress and flow structure. This type of modelling can provide the opportunity to identify important flow mechanisms allowing for a suitable phenomenological model to be proposed. These simulations are dependent on the contact model, but macroscopic behaviours are qualitatively the same for a broad variety of interactions (Delannay *et al.*, 2007). These interactions are typically modelled as a spring and dashpot assembly. The time step used is of the order of 1/20 of a collision time and the simulations are therefore very computationally expensive (Silbert *et al.*, 2001; Börzsönyi *et al.*, 2009; Baran *et al.*, 2006; Berzi *et al.*, 2011; Chevoir *et al.*, 2001) and cannot yet be used to model very large flows.

The experimentalist has also benefited from the introduction of computing power to the field. At the cutting edge, nuclear magnetic resonance imaging is used to examine internal velocity and concentration fields of assemblies of grains (Nakagawa *et al.*, 1993) directly. However, a more common application of computing power in granular laboratories is Particle Image Velocimetry which is used to accurately and quickly measure the velocities at the surface of a granular material. We exploit this technique, along with using an accurate measurement of the flow height in chapter 4, to draw comparisons with theoretical predictions. These two fields are essential in describing the dynamics of a gravity driven free surface granular flow such as the ones we present in chapter 4.

1.4 Aims and Structure

As we have indicated, the derivation of a comprehensively successful granular model may not be possible. Existing models have only been tested on a limited range of experiments and so it is important to see if these models give good predictions under different circumstances. As an example, nearly all granular models predict a maximum value for the friction and so they will predict flows that accelerate indefinitely on slopes higher than a critical angle. However, this hypothesis has not been thoroughly investigated primarily on account of the experimental difficulty of maintaining a flow for a sufficient time to make the multiple measurements needed to track its evolution. We aim to analyse such flows to see if the prediction of maximum friction is correct using the simple geometry of the inclined chute. This not only provides a good basis for studying natural gravity flows such as debris flows and avalanches, but is directly relevant to industrial transport contexts. As a result, it has formed the basis of many experimental studies (Ahn *et al.*, 1991, 1992; Patton *et al.*, 1987; Louge & Keast, 2001; Delannay *et al.*, 2007) with a variety of surface conditions. These studies focus on fully developed flows where all quantities are constant in time and where there is no flow development down the slope. These are inevitably on shallow angles and for small flow heights and mass fluxes. It is not clear whether steady flows exist on higher inclinations or for deeper flows, albeit with a longer relaxation time to the steady state.

Natural granular flows are rarely found on shallow slopes which would allow them to quickly reach a steady state. Instead they are often found to be in a different regime to that traditionally examined in the lab. As such the applicability of existing granular models is limited. It is therefore important that these models are tested for higher inclinations and deeper flows. It is our aim to quantify how dry granular flows behave in such a situation, and present and analyse data for steeper ($30^\circ < \theta < 55^\circ$) and deeper ($q < 20\,\mathrm{kg\,s^{-1}}$) flows than those traditionally examined in the laboratory.

Chapter 2 describes the $\mu(I)$ rheology and the steps leading to its derivation. We give a numerical solution to the rheology for a chute flow. We give the details of the experimental design, measurement systems, calibration routines, data collection and processing in chapter 3, before presenting our observations in chapter 4. We also give a comparison with the $\mu(I)$ numerical solution, discuss the cause of any discrepancies, and look for alternate scalings that collapse the data. Chapter 5 deals with an instability seen in a reasonably large proportion of our data. For sufficiently fast flows we see two dilute regions appear near the walls of the chute. We develop a model based on granular kinetic theory to discuss the mechanism behind the phenomenon. Our conclusions are drawn in chapter 6 where we also suggest directions forward for the questions that this work has not answered.

2

The $\mu(I)$ rheology

With the variety of approaches mentioned in chapter 1, it is clear that there is no consensus on how to model dense granular flows. Indeed, while some models provide good agreement with one set of experiments, they fail when applied to others. Moreover, there remain many granular phenomena that remain unexplained by any model. Some of these models are complicated mathematically, derived using microscopic physical reasoning, but have poor agreement with real flows. Others are phenomenological with no physical grounding at all. Recently, however, a rheology has been proposed by Jop *et al.* (2006), which sits somewhere in between these two categories and uses a combination of dimensional analysis, macroscopic physical reasoning and experimental curve fitting to posit a simple and full three dimensional rheology for dense granular flows. We refer to this rheology as the $\mu(I)$ rheology.

In this chapter we introduce this rheology, the experiments which motivate it, and its application to steady, fully developed flows. We also implement a numerical solution so that we can compare its predictions to the accelerating flows we observe experimentally in chapter 4.

2.1 Motivation

The full three-dimensional $\mu(I)$ rheology given in Jop *et al.* (2006) is an extension of the shallow water model presented in Pouliquen & Forterre (2002), which is in turn based on phenomenological scaling laws of steady flows on inclined planes observed in Pouliquen (1999*b*), which we turn our attention to now.

2.1.1 Friction of a steady flow

Pouliquen (1999*b*) experimentally determined the variation of the mean velocity $\widehat{u}$ as a function of the inclination θ, the thickness of the layer h, and the roughness of the bed: the various non-dimensional groups in this problem enabled him to construct a flow rule governing the flows. These groups are

$$\mathrm{Fr} = \frac{\widehat{u}}{\sqrt{gh\cos\theta}}, \qquad n = \frac{h}{d}, \qquad \theta, \tag{2.1}$$

which are the Froude number, the non-dimensional height and the inclination angle respectively. We are assuming that the particles are sufficiently stiff so that they only dimensional quantities they provide are a length scale d (the diameter for spherical particles) and their density ρ_p, with the elastic time scale considered sufficiently small as to happen instantaneously compared to any time scales for momentum transfer.

This early work focused on determining the range of parameters for which steady flows were observed. It was discovered that, on a rough base, there was a limited region in the parameter space (θ, n) where such flows were observed. For sufficiently high θ all flows accelerated, and for sufficiently low θ flows came to rest. For the intermediate inclinations the flow reached a constant velocity and flow height for a range of flow rates depending on the total mass of the flow. The results were found to depend sensitively on the basal roughness. However, it was noted for each of these steady flows, once the mass source had been removed from the experiment (by shutting the gate at the top of the slope), the flow's height slowly decreased along with the velocity, and a deposit of constant height was left behind. This height was defined as $h_{\mathrm{stop}}(\theta)$. Figure 2.1 shows typical h_{stop} curves for varying θ for four combinations of particle and basal conditions, and these are

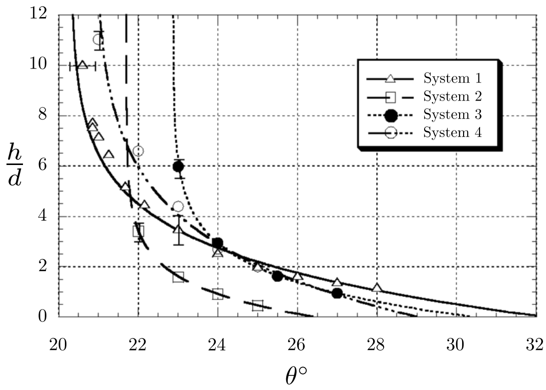

Figure 2.1: *The function $h_{\text{stop}}(\theta)$ for 4 particle/basal condition combinations. The lines are the best fit of equation 2.8 to the data. Figure reproduced from Pouliquen (1999b).*

independent of the flowing conditions used to generate the deposit. Importantly, this is independent of the velocity of the flow.

The h_{stop} curves have two important features — at an angle θ_1 there is an asymptote, which corresponds to point at which the friction of the system of grains is greater than the tangent of the inclination. This causes a heap to form, which effectively has an infinite equilibrium height. The second important feature is that there is a point $\theta_2 > \theta_1$ where $h_{\text{stop}} = 0$. Above this angle, the gravitational forcing is greater than the available friction, and no stable deposit can occur.

When plotting the non-dimensional quantities in equations (2.1), no data collapse was observed, however, introducing the length scale h_{stop} allowed the data to be collapsed very straightforwardly.

The robustness of the scaling can be seen in figure 2.2 which plots the collapse for 4 bead/basal condition combinations over the range of inclinations for which steady flows were possible. This collapse allows us to bypass any microscopic characterisation of either the base or the granular material itself, as the information is all encoded in the $h_{\text{stop}}(\theta)$ function.

With such experiments it is also possible to define another length scale h_{start}, which is the height at which the flow will start moving from rest. This is also found to be a function of the inclination (Mangeney *et al.*, 2007), however it is interesting to note that $h_{\text{stop}} \neq h_{\text{start}}$, which gives a good indication of the presence of hysteresis of granular materials and demonstrates a difference between static

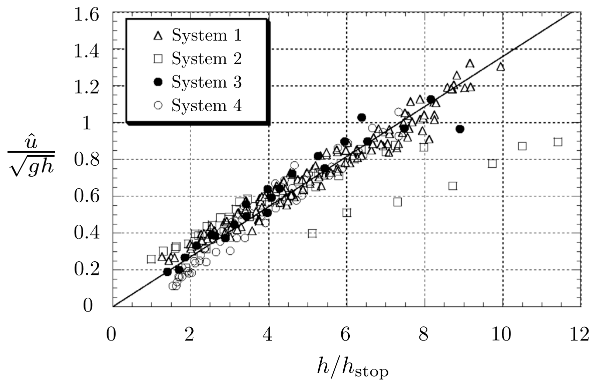

Figure 2.2: $\frac{\widehat{u}}{\sqrt{gh}}$ *as a function of* $h/h_{\text{stop}}(\theta)$ *for the four systems of beads over all inclinations for which steady flows are possible. Reproduced from Pouliquen (1999*b*).*

and sliding friction. It is this difference that is responsible for the avalanching instability seen in shallow flows on inclined planes.

Using the collapse seen in figure 2.2 motivated Pouliquen (1999*b*), we introduce the flow rule

$$\frac{\widehat{u}}{\sqrt{gh}} = \beta \frac{h}{h_{\text{stop}}(\theta)}, \tag{2.2}$$

with $\beta = 0.136$ for the spherical particles that were used in his experiments. We note that, for angular particles, the flow rule actually takes the form $\frac{\widehat{u}}{\sqrt{gh}} = \alpha + \beta h/h_{\text{stop}}$, and the effects of this will be discussed in section 2.2.

From the scaling property in equation (2.2) some information about the forces governing the steady flows can be ascertained to give a rudimentary rheology. Taking a slice of material and balancing the forces acting on it, we can write

$$\tau = \rho g h \sin\theta, \tag{2.3}$$

where $\rho g h \sin\theta$ is the gravitational forcing which, if the flow is steady, must be balanced by a basal shear stress, τ. The average density, ρ is given by the particle density multiplied by the volume fraction, i.e.

$$\rho = \rho_p \phi. \tag{2.4}$$

Given that the normal stress at the base (assuming a hydrostatic balance) is

$p = \rho g h \cos\theta$, we obtain a simple friction law

$$\frac{\tau}{p} = \tan\theta = \mu_b\left(\frac{\widehat{u}}{\sqrt{gh}}, n\right), \tag{2.5}$$

where the basal friction coefficient is μ_b.

As the flow slows and approaches arrest, we have by definition that $h \to h_{\text{stop}}$. As the forces must balance in both a constant velocity flow and a static deposit, the basal friction coefficient must obey

$$\mu_b = \mu_{\text{stop}} = \tan(\theta_{\text{stop}}(h)), \tag{2.6}$$

where the angle θ_{stop} is defined as the inverse of the $h_{\text{stop}}(\theta)$ function. As such, we can write the friction law

$$\mu_b\left(\frac{\widehat{u}}{\sqrt{gh}}, n\right) = \mu_{\text{stop}}\left(h\frac{\beta h}{\frac{\widehat{u}}{\sqrt{gh}}}\right). \tag{2.7}$$

To complete this simple frictional picture, the functional dependence of $h_{\text{stop}}(\theta)$ is obtained experimentally. A suitable fit is given by Pouliquen & Forterre (2002) as

$$\frac{h_{\text{stop}}(\theta)}{d} = B\frac{\tan\theta - \mu_2}{\mu_1 - \tan\theta}, \tag{2.8}$$

which is specified in terms of the frictional limits $\mu_1 = \tan\theta_1$ and $\mu_2 = \tan\theta_2$ and a constant B all of which only depend on the material and the boundary condition. Any form that shares the properties at θ_1 and θ_2 and is monotonically decreasing as discussed above will suffice just as well. Combining equations (2.8) and (2.7) gives a friction dependence of

$$\mu\left(\frac{\widehat{u}}{\sqrt{gh}}, n\right) = \frac{\mu_1 + \mu_2\frac{\widehat{u}}{\sqrt{gh}}\frac{B}{\beta n}}{1 + \frac{\widehat{u}}{\sqrt{gh}}\frac{B}{\beta n}}. \tag{2.9}$$

It is important to note at this point that this expression is not a result of properties of the material bulk, but rather is a manifestation of the interaction between the material and the basal surface. This functional form, along with some other mechanisms to handle flows for which $h < h_{\text{stop}}$, is used by Pouliquen & Forterre

(2002) in a shallow water description to predict the spreading of a granular mass to good effect.

2.1.2 Towards a local description

Although the formulation presented in the previous section gives good agreement with granular flows on planes in a depth-averaged framework, it cannot be thought of as a rheology as it only contains the material-boundary interaction encoded within it. Indeed, applying results derived from plane shear to a generic flow geometry is not *a priori* justified. The next step in extending the h_{stop} results to a full rheology is due to MiDi (2004), who gathered experimental results for the six most frequently studied granular experiments, as pictured in figure 2.3. Their goal was to identify features common to all of the experiments, such as the effective friction and any flow thresholds, with the aim of extracting the underlying behaviour of the material.

Three scales that influence the flow were identified: a scale over which the particle–particle interaction occurs governed by the deformation of the grains, a particle-size scale which governs the local rearrangement of the particles, and the scale of the system.

They note that, away from flow transitions, the microscopic particle–particle friction, restitution and roughness have very little effect on the larger scale kinematics of the flow (for non-extreme values) and indeed only serve to modify the effective friction coefficient. This means that, on a local scale, the flow is not governed by a length scale associated with the deformation or inelastic dissipation of the particles. For large systems this leaves the particle length scale d as the only other natural choice for scalings. As such, we take this as an assumption in the $\mu(I)$ rheology.

We assume that in a homogeneous simple shear flow in a large system (such that the boundaries have negligible influence on the internal flow), the only fields that govern the flows are the strain rate $\dot{\gamma}$, the pressure p, and the shear stress τ. In doing this, we implicitly assume that the granular temperature T does not play a role, and therefore the local generation of the kinetic agitations balances the dissipation. As the only mass in the problem is the particle mass, the flow is independent of the material density, and no internal stress scale exists. These

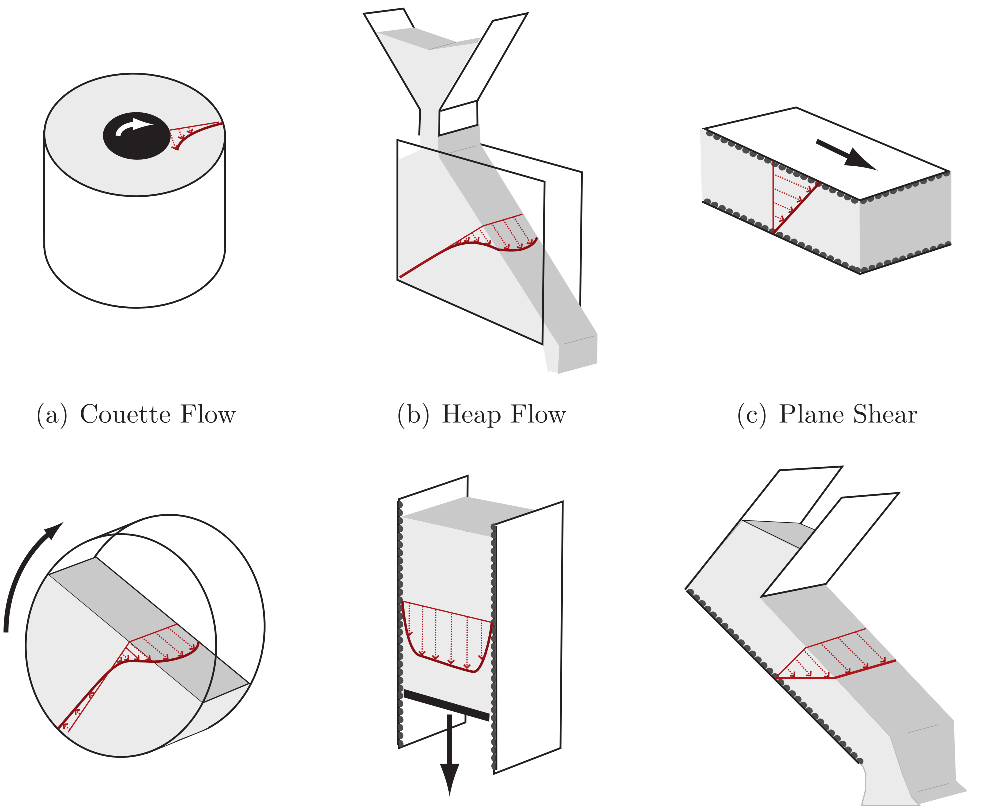

(a) Couette Flow (b) Heap Flow (c) Plane Shear

(d) Rotating Drum (e) Vertical Chute (f) Inclined Plane / Chute

Figure 2.3: *Various flow geometries for which the $\mu(I)$ rheology has been tested. Reproduced from Forterre & Pouliquen (2008).*

fields strongly constrain the form of any local rheological law on dimensional grounds (da Cruz *et al.*, 2005; Lois *et al.*, 2005). Combinations of these fields can produce precisely two dimensionless groups, namely the effective friction

$$\mu = \frac{\tau}{p} \tag{2.10}$$

and the parameter

$$I = \frac{\dot{\gamma} d}{\sqrt{p/\rho}}. \tag{2.11}$$

We call I the *inertial number*, defined as the square root of the Savage number or the Coulomb number which have both been mentioned in the literature previously and introduced as the ratio of the collisional stress to the total stress (Savage, 1984; Ancey *et al.*, 1999). This non-dimensional number can be described as the ratio of two time scales at the particle level. These are given by

$$T_{\dot{\gamma}} = \frac{1}{\dot{\gamma}}, \tag{2.12}$$

the time taken for a layer of shearing particles to move a distance d, and

$$T_p = d\sqrt{\frac{p}{\rho}}, \tag{2.13}$$

a confinement timescale that corresponds to the time taken for the pressure to push the particle back to its original level after having to move up to pass the particles below it. The inertial number I is then given by

$$I = \frac{T_{\dot{\gamma}}}{T_p}. \tag{2.14}$$

A graphical description of the two timescales can be seen in figure 2.4. Importantly, we note that this definition of I only holds for rigid particles as for softer particles the elastic time scale affects the scaling (Campbell, 2002).

The interpretation of I in this way gives a correspondence between its value and the type of flow that it characterises. For slow, quasi-static flows, the movement between layers of particles is slow, whereas the confinement time is relatively fast as the particles' inertia has little effect, and therefore I is small. Conversely, flows

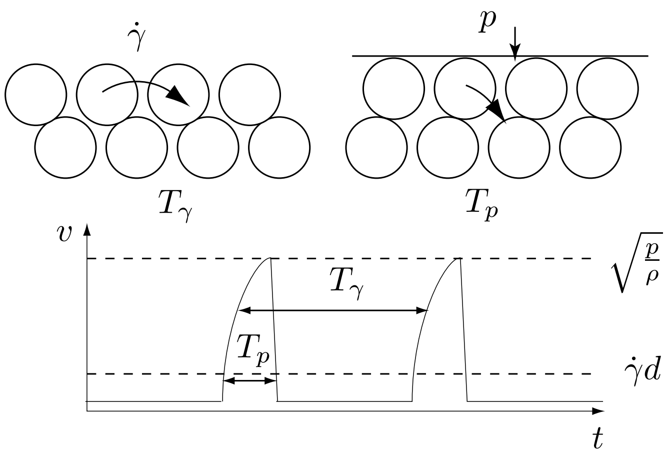

Figure 2.4: *Schematic showing the physical meaning of the deformation time scales T_p and $T_{\dot{\gamma}}$. Reproduced from MiDi (2004).*

with large shear rates such that the particle inertia overcomes the confinement force, are agitated and (probably) dilute. These flows correspond to a large value of I.

In the picture painted above, we can also argue that the volume fraction ϕ should be a slaved variable of I. Using the timescales introduced above we can reason for a crude trend as I varies (Pouliquen *et al.*, 2006). By considering the movement of a single bead over a layer, we can see that the maximum volume fraction $\phi_{\max}$ is attained when the particle's centre is as low as possible, i.e. when the particle is lying as much as possible in the space between the particles below. However, when shear is applied, the particle is forced to rise in order to move over the particles below, thus leaving the empty space until it lies fully on top of a particle below, at which point the volume fraction attains its minimum $\phi_{\min}$. Given that the typical time for rearrangement is $T_{\dot{\gamma}}$, and the time the particle stays trapped is $T_{\dot{\gamma}} - T_p$, the time averaged volume fraction is given by

$$\phi = \frac{T_{\dot{\gamma}}\phi_{\min} + (T_p - T_{\dot{\gamma}})\phi_{\max}}{T_p}, \tag{2.15}$$

equating to a dependency of

$$\phi = \phi_{\max} - (\phi_{\max} - \phi_{\min})I. \tag{2.16}$$

However, this variation of ϕ is only applicable where the particles are largely in contact with each other and for small I. This suggests that, as I grows, the flow will indeed become dilute and the reasoning used above will break down and the linear relationship will not hold. Typical values are taken as $\phi_{\text{max}} = 0.6$ and $\phi_{\text{min}} = 0.5$ (Baran *et al.*, 2006; Pouliquen *et al.*, 2006; MiDi, 2004), indicating a rather weak dependence over the range of I that has been investigated in the past.

It has been known since some of the earliest studies of granular media that granular flows exhibit dilatancy effects when flow is initiated, so that the particles can slide over one another (Reynolds, 1885). However, once this transition has occurred, the volume fraction in the bulk changes only weakly. This has been verified with both simulations (Silbert *et al.*, 2001) and experiments (Louge & Keast, 2001). At the boundaries, however, some minor but interesting effects still occur, which we shall discuss in more detail in section 2.2. Despite this, numerous experimental and numerical studies (Rajchenbach, 2003; Louge & Keast, 2001; Jenkins, 2007) suggest that the approximation $\phi = \text{const.}$ is acceptable.

Under the assumption that the rheology is local and governed by the fields above, the effective friction of equation (2.10) must be a function of the inertial number, and we may extend our results obtained from plane shear to a general rheology for granular materials.

However, this new local rheology should produce the experimental scalings given in the previous section, specifically the basal friction law in equation (2.9). Our strategy to get the functional dependence of $\mu(I)$ is to depth-integrate the flow assuming this rheology so that we may compare it to the aforementioned friction law.

The steady plane shear flows for which the basal friction law applies, the force balance

$$\mu(I(z)) = \tan\theta \tag{2.17}$$

must be obeyed. In our coordinate system we take $z = 0$ at the basal surface and $z = h$ at the free surface. This implies that I is constant throughout the depth and is a function of θ alone and therefore constant in a given flow. The definition

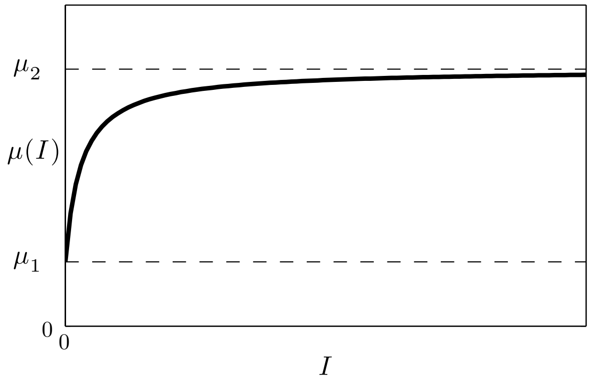

Figure 2.5: *A typical* $\mu(I)$ *curve.*

of I in equation (2.11) allows us to integrate the velocity profile to obtain

$$\frac{u(z)}{\sqrt{gd}} = \frac{2}{3} I(\theta)\sqrt{\cos\theta}\frac{(h^{3/2} - (z-h)^{3/2})}{d^{3/2}}, \tag{2.18}$$

which recovers the Bagnold velocity profile. We now integrate 2.18 once again to obtain

$$I = \frac{5}{2}\frac{\mathrm{Fr}}{n} \tag{2.19}$$

Substituting this into the basal friction law (2.9) gives the relationship

$$\mu(I) = \mu(I)|_{z=0} = \frac{\mu_1 I_0 + \mu_2 I}{I_0 + I}, \tag{2.20}$$

where I_0 is given by

$$I_0 = \frac{5}{2}\frac{\beta}{B\sqrt{\cos\theta}}. \tag{2.21}$$

This analysis of steady, plane shear flow motivates the choice to take equation (2.20) as a definition for a rheology applicable to all dense granular flows. The two parameters μ_1 and μ_2 are dependent on the material and are given by determining the range of inclinations for which h_{stop} exists. On the other hand, I_0 obviously depends on the flow geometry, but for cases other than plane shear flow it is not clear *a priori* what form that this should take. Usually I_0 is assumed to be a constant, i.e. another material parameter. This can be done for steady shear flows as the dependence on the inclination is rather weak over the limited range for which steady flows are possible. For experiments with glass beads as used by the papers referenced here, I_0 is taken to be around 0.3. As we shall subsequently see, the precise value of I_0 will not affect our conclusions of the suitability of the $\mu(I)$ rheology to high speed granular flows. For this reason, we will not dwell on how this parameter varies.

A one-dimensional rheology capturing the above behaviour can therefore be stated as

$$\tau = \mu(I) p \operatorname{sign}\left(\frac{\partial u}{\partial z}\right) \tag{2.22}$$

when there is shear present (i.e. $\partial_z u \neq 0$). We have introduced the quantity $\partial_z u$ to ensure that the friction acts to oppose the shear in the material. This one-dimensional rheology has two important characteristics. Firstly, there exists a yield stress $\tau = \mu_1 p$, below which no flow is possible. In general, such a threshold introduces considerable complications to the solution of such a flow: for any areas where there is no shear, the stresses become ill-defined and depend on the detailed history of deformation. The shear stress in these areas obeys the inequality

$$\tau < \mu_1 p. \tag{2.23}$$

To deal with these areas rigorously we can introduce a yield surface along which the stress balances the yield stress. We then calculate the movement of the plug region as a whole by considering the stresses on the boundary.

The second characteristic is that μ is bounded above as $I \to \infty$, indicating that there is a limit to the friction that the granular material can exhibit. Above this limit, the model gives a strong prediction that, in the absence of additional forces such as air resistance, the material will accelerate indefinitely. It is the main purpose of this thesis to see if its predictions hold for higher inclinations and values of I than previously tested.

2.1.3 Three dimensional rheology

The one-dimensional $\mu(I)$ rheology provides a sufficient framework to compare to the averaged development of flows down an inclined chute. However, it gives no information about the internal structure of the flow. Jop *et al.* (2006) generalised this rheology to a full tensorial formulation to predict both the cross slope and depth dependence of the flow on a heap. We take coordinates such that $z = 0$ at the base and $z = h$ at the free surface, x increases down the slope and y completes the xyz right handed triad. The stress tensor (which takes the same form as in Schaeffer, 1987) is thus given by

$$\sigma_{ij} = -p\delta_{ij} + \tau_{ij} \qquad \text{with} \qquad \tau_{ij} = \eta(|\dot{\gamma}|, p)\dot{\gamma}_{ij}, \tag{2.24}$$

where p is the pressure, τ the shear stress, δ_{ij} the Kronecker delta or identity tensor, and $\dot{\gamma}$ is the symmetric strain tensor given by

$$\dot{\gamma}_{ij} = \frac{\partial u_i}{\partial x_j} + \frac{\partial u_j}{\partial x_i}. \tag{2.25}$$

We define the modulus or second moment of the strain tensor as

$$|\dot{\gamma}| = \sqrt{\frac{1}{2}\dot{\gamma}_{ij}\dot{\gamma}_{ij}}. \tag{2.26}$$

In an analogy to Newtonian fluid mechanics, Jop *et al.* (2006) introduced a non-constant viscosity η, which is defined in terms of the friction coefficient defined in equation (2.20):

$$\eta\left(|\dot{\gamma}|, p\right) = \frac{\mu(I)p}{|\dot{\gamma}|}. \tag{2.27}$$

This indicates that the material is shear thinning i.e. the resistance of the material decreases the quicker it is deformed. We also note that, unusually, the viscosity is also a function of the pressure. We generalise the definition of I slightly to account for the three-dimensional nature of the flow

$$I = \frac{|\dot{\gamma}|\, d}{\sqrt{p/\rho}}. \tag{2.28}$$

In this formulation we recover that the total shear stress is $|\tau| = \mu(I)p$ as in the one-dimensional rheology. The tensorial formulation just serves to direct this frictional stress along the direction of the strain.

The three-dimensional rheology still possesses a yield stress, the only difference being that the scalar shear stress in the one-dimensional rheology must be replaced by its absolute value:

$$|\tau| = \mu_1 p. \tag{2.29}$$

2.2 Validity

Having derived the above rheology, it is important to discuss how the assumptions made affect its range of applicability, and whether it can indeed predict salient flow features. To this end, we will give a brief review of the effectiveness of the rheology for the flow configurations pictured in figure 2.3. We shall briefly examine the large body of experimental and numerical work assembled in the article of MiDi (2004) to understand where the rheology gives good agreement and where the assumptions used in the derivation break down.

2.2.1 Inclined Plane

It is perhaps unsurprising that the $\mu(I)$ rheology gives some of its best agreement with steady, fully developed flows on an inclined plane, on account of the parameters used to fit the friction law being taken from such experiments. As derived above, the rheology captures quantitatively the Bagnold depth dependence of the velocity profile (although this also arrives through dimensional analysis of any local rheology) for deep flows. Since the friction must balance gravity everywhere in the flow (equation (2.17)), we predict that I is constant and therefore so is the volume fraction. Tautologically, the flow rule (2.2) is also followed.

Perhaps more interesting are the inclined plane flows for which the rheology does not predict the correct behaviour. For shallow flows, when $h \sim h_{\text{stop}}$, the observed velocity profile is linear, and cannot be predicted by the rheology. The difference in velocity profiles can be seen in figure 2.6. A plausible explanation for this discrepancy is the appearance of non-local effects such as force chains and particle correlations, which add another length scale to the problem, thus rendering the dependence of the rheology solely on I inaccurate. This is indicative of a more general behaviour of the $\mu(I)$ rheology giving poor agreement near flow thresholds, which we shall return to a little later.

However, the steady plane shear flow mentioned here is only one very specific type of flow seen on inclined planes. Although the $\mu(I)$ rheology cannot account

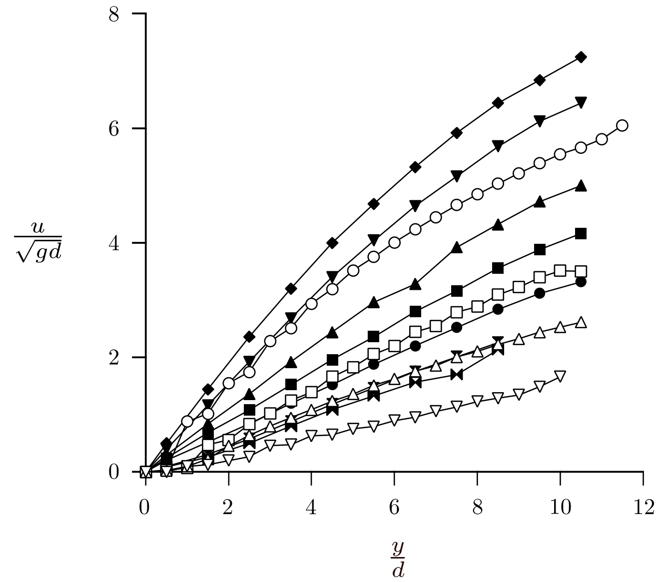

Figure 2.6: *Velocity profiles for equilibrium flows on inclinations* 12.6°–36° *at a fixed non-dimensional height for a variety of particle species. The flows on smaller inclinations are such that $h \sim h_{\rm stop}$ and the profiles appear linear. This is possibly due to the presence of force chains and correlated particle motion violating the local assumption of the $\mu(I)$ rheology. The steeper flows with $h > h_{\rm stop}$ exhibit the predicted Bagnold profile.*

for hysteresis and therefore the avalanching instability, it has been used to good effect to predict other instabilities, such as the presence of roll waves (Forterre & Pouliquen, 2003) and levée formation and self channelization (Mangeney *et al.*, 2007).

2.2.2 Heap flow and Rotating Drum Flow

These two flow configurations are often referred to as surface flows since the majority of the flow occurs near the surface. These flows are tricky to characterise as they contain regions where the flow is fluidised and free-flowing on top of (almost) static regions. Comparing these flows to the conclusions from steady inclined plane flow, we would expect the $\mu(I)$ rheology to agree well in the flowing region, and less so in the quasi-static regions. Heap flows are formed when sand is poured in between two plates as in figure 2.3(b). In contrast to the flow over an inclined plane, the inclination of the free surface is chosen by the system. The flow is largely localised at the free surface, as the side-walls supply an extra frictional contribution that stabilises the pile beneath.

Jop *et al.* (2005) consider the integrated force over a horizontal element that spans the chute transversely, and is infinitesimal in height. They identify the three forces acting on it, namely gravity, the friction from the side-walls and the force due to the vertical shear, which should be given by the $\mu(I)$ rheology. They assume that the element slips against the smooth side-walls and model the interaction as a Coulomb friction with coefficient μ_{w}, i.e. proportional to the pressure, which is taken as lithostatic. If the chute width is given by W then the balance between the three gives

$$0 = \tan\theta - \mu_w \frac{z}{W} - \mu(I). \tag{2.30}$$

This suggests that the frictional contribution to the motion increases deeper into the pile. Since $\mu(I) > \mu_1$ in flowing regions, we can calculate a height h below which this rheology predicts no flow, i.e.

$$\frac{h}{W} = \frac{\tan\theta - \mu_1}{\mu_{\mathrm{w}}}. \tag{2.31}$$

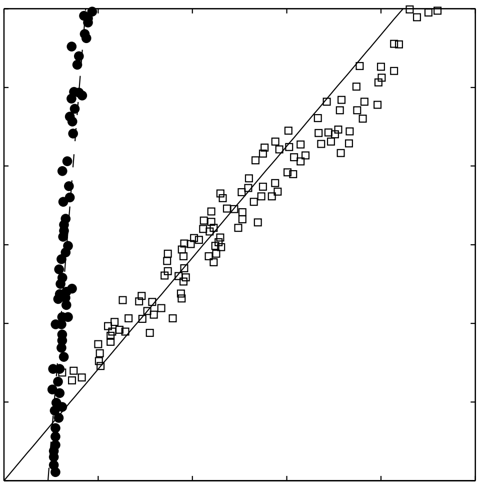

Figure 2.7: *The flow rule for sand (●) and glass beads (□). Modified from MiDi (2004).*

However, careful observations made by Komatsu *et al.* (2001) indicate that this depth threshold does not exist. Instead, an exponential tail is seen in the velocity profile that percolates to the bottom of the pile. However, despite this prediction of a yield surface within the flow, the $\mu(I)$ model with added side-wall friction gives good predictions of the velocity profile near the surface. The necessity of including W in the analysis indicates that, strictly, the $\mu(I)$ rheology is not valid, as it is predicated on d being the only relevant length scale in the problem. However, including the wall friction explicitly gives good agreement with experimental evidence.

The problem of introducing an additional length scale into the problem can also been seen in the modification of the flow rule (2.2) for angular particles. In such a case it takes the form as shown in MiDi (2004)

$$\frac{\widehat{u}}{\sqrt{gh}} = \alpha + \beta \frac{h}{h_{\text{stop}}(\theta)}. \tag{2.32}$$

The data shown in figure 2.7 show the fit for glass beads flowing over glass beads and sand flowing over sand. The additional constant α poses a difficulty for the $\mu(I)$ rheology as it demonstrates a dependence of the friction coefficient, not only on the value of I calculated by values of the fields locally, but also on the non-local parameter n. If we equate h_{stop} in equations (2.32) and (2.8), invert in terms of $\tan\theta$ and put into equation (2.6) using the definitions for I and I_0 above, the flow rule then predicts that

$$\mu = \mu\left(I - \frac{\alpha I_0 B}{\beta}\frac{1}{n}\right). \tag{2.33}$$

This means that the rheology as it stands is not able to predict this behaviour for angular particles, and a local description is no longer strictly valid. We are unable to express the rheology locally in terms of I as the boundaries of the flow become important, and therefore d is no longer the sole length scale in the problem — it is supplemented in this case by a system size field n, the dimensionless flow height.

2.2.3 Confined Flows

The three classes of confined flows investigated by MiDi (2004) are the vertical chute, plane shear experiments and Couette flow. The canonical experiment for rheological studies is plane shear on account of its geometrical simplicity. The presence of gravity is a complicating influence, causing the shear to be unequal across the system and so many studies are carried out numerically (Aharonov & Sparks, 1999; da Cruz *et al.*, 2005, e.g.). Typically, the experiments fall into two categories: fixed volume, where the distance between the shearing plates is fixed, or fixed force, where the distance between the plates is changed in order to maintain a constant pressure.

The force balance in gravity-free plane shear means that the pressure and shear stress are constant throughout. As a result, I, and therefore μ, are also constant across the chute, and the velocity exhibits a linear variation. This analysis holds well for moderately quick flows, however, for higher values of I, slip develops at the wall and an inflection point appears in the velocity profile, indicating a complex boundary effect which the $\mu(I)$ rheology is unable to capture.

For the vertical chute and Couette flows, the $\mu(I)$ rheology also runs into problems with the behaviour at the boundaries. In both of these cases, the shear is localised in bands near the boundaries with a shear-free region elsewhere. In vertical chutes the $\mu(I)$ rheology predicts a dependence of the shear band thickness on the velocity but in practice this has a fixed width of around 5–10 d regardless of the velocity and set only by the inclination and the wall roughness. The misestimation of the shear bands is a clear indication that the local model cannot accurately capture the transition from a flowing to a static or plug region. The appearance of these plug-like regions implies a large particle correlation and the presence of force chains spanning the system. Under these circumstances, the local assumption breaks down and therefore I is not the appropriate dimensionless number to describe the problem.

2.2.4 Discussion

As we have seen, although the rheology gives good quantitative agreement with a number of experiments, there are several areas where its predictive ability is weak. The assumptions used in the derivation of the rheology give a good idea as to where the model will be valid.

The six control geometries used in MiDi (2004) indicate that the model performs well far away from shear-free areas. This is to be expected for two reasons: the stresses are only well-defined when their history is taken into account in shear free regions, and the local assumption is broken as the correlation of the particles approaches the system size. In general, free surface flows with no static regions match closely with the predictions. This should be no surprise as the material properties μ_1, μ_2 and I_0 are measured for such flows. Even within the inclined flow from which they are derived, I_0 is a weak function of the inclination. Asking these parameters to predict the flow in a completely different geometry is perhaps too much — it is possible that the confined flows would benefit from a different choice of these parameters.

A strength of this model is its mathematical simplicity and experimental accessibility — it does not require the measurement of many microscopic parameters. Indeed, it is with great difficulty that even a simple parameter such as the coefficient of restitution is measured reliably for irregularly shaped particles. The influence of many of these parameters is simply encoded within the h_{stop} and μ functional dependencies. However, it is perhaps regrettable that the rheology is not derived from micro-physical principles, but there is some consolation as this is a distinction shared with even viscous flows which are extremely well understood in comparison.

Even within the framework set out above, the precise functional dependency of μ is somewhat arbitrary as it stems from the character of the h_{stop} curve (2.8), whose only salient features are that there is an asymptote, a root and a continuity between the two. These constraints leave a certain amount of freedom to choose the fit function. Originally, Pouliquen (1999*b*) chose an exponentially decreasing function for h_{stop} but that was revised subsequently (Pouliquen & Forterre, 2002, e.g.) to a rational function of $\tan\theta$. This does not make a huge difference in the subsequent analysis for dense flows, but serves to simplify the algebra somewhat. For high values of I, such flows will be more sensitive to the precise shape of the $\mu(I)$ curve, but primarily we shall not be considering these flows.

Flows that are near a transition appear to be poorly predicted by the $\mu(I)$ rheology. At one extreme, slow, quasi-static flows often have shear bands and, in general, the scaling of their width is not correctly predicted by the model. At the other extreme, the transition to a kinetic flow at high I cannot be predicted by this rheology. This is no surprise as the constitutive relation (2.15) has not been compared with data at high inertial number and so the volume fraction dependence for high I is not known. Indeed, the high energy flows exhibit a dependence on the particle–particle coefficient of restitution and an elastic timescale, thus rendering the $\mu(I)$ model ineffective (Pouliquen *et al.*, 2006).

However, the comparison with dense flows presents a different picture. Unless shear localization has occurred, the model gives good agreement with experimental observations. The appearance of regions that are static indicates a zone over which a transition occurs. The model as it stands is ill-prepared to deal with such features. This should come as no surprise, as the flow law (2.2) only applies to flows with $h > h_{\text{stop}}$ and therefore $\text{Fr} > \beta$. Should the flow near this threshold, non-local effects are apparent as the flow arrests and a network of force chains develops. Pouliquen & Forterre (2002) extend the friction law to deal with quasi-static flows in a depth integrated framework effectively, but the choice of this extension is arbitrary, and simply provides a smooth transition to the static state, allowing numerical computation. Despite this problem, Mangeney *et al.* (2007) give good qualitative predictions of the levée formation in debris flows. Another signal of the difficulty of dealing with shear-free regions can be seen in the difference between θ_{start} and θ_{stop}. A stationary granular assembly on an inclined plane will need to be raised to an inclination $\theta_{\text{start}} > \theta_{\text{stop}}$ before it starts flowing, but the inclination can be subsequently reduced and the flow maintained. A similar effect can be seen in Couette flow, where the rotation rate required to maintain a flow is less than the rate required to initiate it. The ideal friction criterion used in the model cannot predict this hysteresis as it has no awareness of the history of the sample. Generally, these flow transitions are affected by the system size, a signature of non-trivial finite-size and boundary effects that are not well understood. As a result, the avalanching instability seen in rotating drum granular flows and shallow granular flows on an inclined plane cannot be predicted using this approach. It is likely that this metastability of granular flows will require a biphasic description of the strong (force chains) and weak (collisions, friction) forces in order to accurately resolve this flow behaviour (Deboeuf *et al.*, 2005).

In summary, the steady laterally uniform flow regime of granular materials down inclined planes has been largely characterised over the small range of angles $\theta_1 < \theta < \theta_2$, however, the application of the knowledge gained from these steady flows to ones on higher inclinations is an unresolved issue — one that we turn our attention to now.

2.3 Application to steep chute flows

While the $\mu(I)$ rheology has been analysed for a plethora of steady, fully developed flows, we arrive at the focus of this thesis: the application to flows for inclinations $\theta > \theta_2$. Due to the mathematical complexity of the $\mu(I)$ equations, it is necessary for investigations to be of a numerical nature as very limited analytic progress can be made. We present a simple first order finite volume numerical scheme to examine the full three-dimensional structure of the flow, with a view to compare the predictions to the experimental data presented in chapter 4.

2.3.1 Problem Formulation

We make three assumptions on the nature of the flow, the first being the assumption of constant density. Experimental studies such as Louge & Keast (2001) and

Rajchenbach (2003) show no large density differences within the flowing layer. This is also seen numerically in simulations such as Silbert *et al.* (2001). Indeed, there were only small differences between the volume fraction in static and flowing regions and we therefore assume that $\phi \approx \phi_{\mathrm{rcp}}$. It is noted that the granular medium does become dilute close to the free surface (partly because of velocity fluctuations there), however, this layer is very thin (as confirmed by our own experimental observations). Therefore, to the first order, we assume that this variation of density is not essential to describing our flow.

The second assumption is that the flow in the chute has no flow in the transverse or y direction, i.e. $\boldsymbol{u} = (u, 0, w)$, where u and w are both functions of all three position components. This has the consequence that we ignore any secondary circulation flows. Our experimental data suggest that these effects are small compared to the mean flow; the y-velocity at the surface is of the order of 1% of the downstream velocity. Forterre & Pouliquen (2008) also report that cross slope velocities for such flows are very small. The third assumption, which is also experimentally motivated, suggests that the flow is steady in time but develops as a function of x. We therefore take $\partial_t = 0$.

Using these assumptions, we can write the local conservation of mass

$$\boldsymbol{\nabla} \cdot (\rho \boldsymbol{u}) = 0 \tag{2.34}$$

as

$$\frac{\partial u}{\partial x} = -\frac{\partial w}{\partial z}. \tag{2.35}$$

The momentum balance is given by

$$\nabla \left(\rho \boldsymbol{u}\boldsymbol{u}\right) = \boldsymbol{F} + \nabla \cdot \boldsymbol{\sigma}. \tag{2.36}$$

where $\boldsymbol{uu}$ is the dyadic product of $\boldsymbol{u}$ with itself. Then, using the $\mu(I)$ representation for the stress tensor in equation 2.24, the x, y and z momentum balances are given by

$$\rho\left(u\frac{\partial u}{\partial x}+w\frac{\partial u}{\partial z}\right) = \rho g\sin\theta-\frac{\partial p}{\partial x}+\frac{\partial \tau_{xx}}{\partial x}+\frac{\partial \tau_{xy}}{\partial y}+\frac{\partial \tau_{xz}}{\partial z}, \quad (2.37)$$

$$0 = -\frac{\partial p}{\partial y}+\frac{\partial \tau_{xy}}{\partial x}+\frac{\partial \tau_{yy}}{\partial y}+\frac{\partial \tau_{yz}}{\partial z}, \quad (2.38)$$

$$\rho\left(w\frac{\partial w}{\partial z}+u\frac{\partial w}{\partial x}\right) = -\rho g\cos\theta-\frac{\partial p}{\partial z}+\frac{\partial \tau_{xz}}{\partial x}+\frac{\partial \tau_{yz}}{\partial y}+\frac{\partial \tau_{zz}}{\partial z}, \quad (2.39)$$

respectively.

In addition to these, we also have an integral condition specifying the global mass flux:

$$q=\iint \rho u\ \mathrm{d}A = W\widehat{\rho u h}, \quad (2.40)$$

which is constant down the slope.

At this point, we can simplify the algebra of the problem considerably by exploiting two different length scales of the flow. The first is h, which gives the scale over which the flow varies vertically. The second is a characteristic length scale L over which the down stream velocity develops. This is calculated by forming a crude balance of the advective acceleration and the gravitational forcing minus the friction contribution, i.e.

$$\frac{u^2}{L}\sim g\cos\theta\left(\tan\theta-\mu\right), \quad (2.41)$$

giving

$$\epsilon=\frac{h}{L}\sim \mathrm{Fr}^{-2}\left(\tan\theta-\mu\right). \quad (2.42)$$

Provided that $\epsilon \ll 1$ we can make considerable simplifications to equations (2.37), (2.38) and (2.39). Our experimental evidence presented in chapter 4 in figure 4.7(a) shows that the flows we consider have $5<\mathrm{Fr}<25$ and $0.8<\mu/\tan\theta<1$, equating to a value of ϵ of no more than 0.01, and typically much smaller. Also assuming that $W \ll L$, we can neglect the derivatives on the left hand side of (2.39) as well as all of the stress tensor terms, thus leaving the hydrostatic balance

$$p=\rho g(h-z)\cos\theta. \quad (2.43)$$

This approximation is usually termed the long-wave approximation, and is used by Savage & Hutter (1989); Gray *et al.* (2003); Mangeney *et al.* (2007) and many others.

As we have assumed that there is no lateral velocity v in the $\mu(I)$ rheology we may neglect the shear tensor derivatives in the y-momentum balance (2.38). As such, we have that

$$\frac{\partial p}{\partial y} = O(\epsilon), \tag{2.44}$$

and so $h = h(x)(1 + O(\epsilon))$ using equation (2.43), i.e. just a function of x and not the cross-chute coordinate y. We may therefore treat h as equal to its average value as specified by equation (2.40). This small cross-chute variation of h is in accordance with our experimental observations. Under this condition, according to (2.40)

$$h = \frac{q}{W\rho\hat{u}} \tag{2.45}$$

The x momentum equation is also simplified considerably by the long-wave approximation. The stretching stress term $\tau_{xx,x}$ can be neglected as $\partial_x\tau_{xx} \sim \epsilon^2\partial_z\tau_{xz}$. The contribution due to w_x in the term $\tau_{xz,z}$ can also be neglected. Lastly, we can also neglect the stress given by the downstream pressure gradient since $\partial_x p \sim \rho g\partial_x h \sim \epsilon\mu\rho g \sim \epsilon\partial_z\sigma_{xz}$.

With these simplifications, the balance of vertical momentum is then given by the hydrostatic pressure balance and the downstream momentum by

$$\rho\left(u\frac{\partial u}{\partial x} + w\frac{\partial u}{\partial z}\right) = \rho g\sin\theta + \frac{\partial \tau_{xy}}{\partial y} + \frac{\partial \tau_{xz}}{\partial z}. \tag{2.46}$$

The long wave approximation also simplifies the computation of the shear stress and the inertial number as

$$|\dot{\gamma}| = \sqrt{\partial_y u^2 + \partial_z u^2} + O(\epsilon) \tag{2.47}$$

To complete the description of the problem we must specify the basal and side-wall boundary conditions. For the basal condition we simulate a rough surface by applying a no-slip boundary condition, while for the side-walls a Coulomb friction is applied with coefficient μ_{w} and so a slip velocity is permitted. The side-wall condition can be written as

$$\tau_{xy} = -\mu_{\mathrm{w}} p u/|u|, \tag{2.48}$$

where μ_{w} is a constant taken from h_{stop} measurements over the perspex wall material ($\mu_{\mathrm{w}} = 0.45$).

Care must be taken at the free surface as the highest derivative in equation (2.46) is multiplied by zero. The equation is therefore singular and first order there, and no boundary condition is necessary. However, as $\sigma \propto p$, the surface is stress-free which is the boundary condition we would normally expect to apply. This leads to the behaviour of I near the free surface being complicated and warrants further investigation. If we assume a Bagnold depth dependence near the surface then

$$\frac{\partial u}{\partial z} = \frac{I_{\mathrm{Bag}}\sqrt{zg}}{d}, \tag{2.49}$$

for some constant I_{Bag}, which is the value of I in a 2-D pure Bagnold flow. If, in addition to this, there is a cross slope variation near the surface then

$$I = \frac{d}{\sqrt{zg}}\sqrt{\left(\frac{\partial u}{\partial y}\right)^2 + \left(\frac{\partial u}{\partial z}\right)^2} = \sqrt{\frac{d^2}{zg}\left(\frac{\partial u}{\partial y}\right)^2 + I_{\mathrm{Bag}}^2}, \tag{2.50}$$

implying that $I \to \infty$ as $z \to 0$ at the free surface, if $\partial_y u \neq 0$. The thickness of the boundary layer over which the y-variation in I decays to I_{Bag} is given by

$$z = \frac{d^2}{I_{\mathrm{Bag}}^2 g}\left(\frac{\partial u}{\partial y}\right)^2. \tag{2.51}$$

We do not attempt to resolve this boundary layer in our simulation as μ remains finite and is multiplied by $p = 0$ at the surface, meaning that the stress remains well-defined everywhere. Because we are using a finite volume method, the stresses on the top edges of the top cell are zero even though I is infinite since μ is finite and $p = 0$.

Since the only x gradient in the problem is the first term on the LHS of equation (2.46) we can treat the problem as an initial value problem in x. Ordinarily this marching of u would be done in the variable t, but instead we march u^2 with the variable x. In this formulation we therefore require an initial condition.

The initial condition requires specifying $u(0, y, z)$ but, experimentally, only the initial velocity at the surface $u(0, y, h)$ can be measured. As such, the depth dependence of the velocity profile is unknown and can be treated as a degree of freedom with which to fit the numerical results to the experimental data. Experimentally, to begin with, there is little y-variation of the velocity profile. For this reason, the initial condition is chosen to be a near-plug flow with the value of the mean velocity slightly less than the first recorded experimental measurement. This was done to allow the effect of the initial condition to be minimised before the flow is quick enough for comparisons to be made to the experimental data. There is a small amount of shear introduced in the initial profile to avoid convergence issues in the near-static regions. Other initial conditions based on the shape of the experimental velocity profile have also been tried, but the *shape* of the results are largely similar after around 1 m of travel. Unsurprisingly the average velocity of the initial condition will have a larger effect on the velocities at a given x as the mass accelerates down the slope.

2.3.2 Numerical Method

To solve this problem numerically a staggered grid scheme is used to discretise the velocity and calculate the appropriate derivative quantities, otherwise known as a finite volume scheme. The computational domain is split up into a rectilinear grid of NM cells of equal size where N is the number of cells in the y direction and M is the number of cells in the z direction. We then introduce the discretized grid coordinates

$$y_n = \left(n - \frac{1}{2}\right)\delta y \tag{2.52}$$

$$z_m = \left(m - \frac{1}{2}\right)\delta z \tag{2.53}$$

where $\delta y = W/N$ and $\delta z = h/M$. The cell centres depicted in figure 2.8 are then given when $n, m \in \mathbb{N}$ in the range $1 \leq n \leq N$ and $1 \leq m \leq M$. The basal boundary and the free surface are given by $m = 1/2$ and $m = M + 1/2$ respectively, and the side-walls by $n = 1/2$ and $n = N + 1/2$. The boundaries are

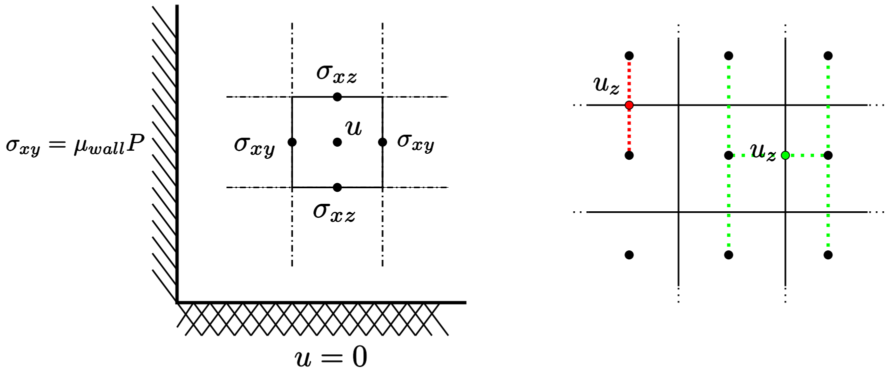

Figure 2.8: *Depiction of the cell structure and differentiation schemes used in the finite volume method for solving the $\mu(I)$ rheology for a chute flow.*

therefore half a cell away from the nearest point at which velocity data is stored. The velocity is centrally differenced to give the derivative quantities $u_z \equiv \partial_z u$ and $u_y \equiv \partial_y u$ at the cell boundaries i.e. on a grid offset by half a cell's width and height from the velocity data. The differentiation scheme is shown pictorially in figure 2.8 and in table 2.1. Since we require both u_z and u_y on all midpoints of the staggered grid two different differentiation stencils must be used. It can be seen that u_y at the point shown in figure 2.8 must necessarily have a total of 4 velocity points to calculate the derivative, where u_z in the figure only requires two. This can be seen in more detail in table 2.1. The derivative quantities calculated on the cell boundaries are used to calculate the stress tensor $\boldsymbol{\sigma}$, which in turn is centrally differenced to give the divergence of $\boldsymbol{\sigma}$ at the cell centres. This is the rheological contribution to the change in velocity as x increases.

As we do not store velocity information on the boundaries of the numerical domain, we must extrapolate where appropriate to calculate derivative quantities there. In order to maintain the accuracy of derivatives there a quadratic extrapolator was chosen of the form shown in table 2.1. For the side walls, this extrapolator uses three velocity points in the y direction to extrapolate to the side wall. For the free surface we follow a similar routine but instead take the three points in the z direction as the data for the extrapolation. As there is a no-slip condition at the basal surface, we impose $u = 0$ there and calculate derivatives appropriately.

Care must also be taken in regions where $|\dot{\gamma}| = 0$ as the stresses are ill-defined

Discretization

$$u^{n,m} = u(y_n, z_m)$$

Internal derivatives

$$\begin{aligned}
u_z^{n,m+1/2} &= \frac{1}{\delta z}\left(u^{n,m+1} - u^{n,m}\right) \\
u_z^{n+1/2,m} &= \frac{1}{4\delta z}\left(u^{n+1,m+1} - u^{n+1,m-1} + u^{n,m+1} - u^{n,m-1}\right) \\
u_y^{n+1/2,m} &= \frac{1}{\delta y}\left(u^{n+1,m} - u^{n,m}\right) \\
u_y^{n,m+1/2} &= \frac{1}{4\delta y}\left(u^{n+1,m+1} - u^{n-1,m+1} + u^{n+1,m-1} - u^{n-1,m-1}\right)
\end{aligned}$$

Boundary derivatives (4 point stencil)

$$\begin{aligned}
u_y^{1,m+1/2} &= \frac{1}{3\delta y}\left(u^{2,m+1} - u^{1/2,m+1} + u^{2,m-1} - u^{1/2,m-1}\right) \\
u_z^{n+1/2,1} &= \frac{1}{3\delta z}\left(u^{n+1,2} - u^{n+1,1/2} + u^{n-1,2} - u^{n-1,1/2}\right)
\end{aligned}$$

Boundary derivatives (2 point stencil)

$$\begin{aligned}
u_y^{1/2,m} &= \frac{2}{\delta y}\left(u^{1,m} - u^{1/2,m}\right) \\
u_z^{n,1/2} &= \frac{1}{\delta z}\left(u^{n,1} - u^{n,1/2}\right)
\end{aligned}$$

Quadratic extrapolator

$$u^{1/2,m} = \frac{15}{8}u^{1,m} - \frac{5}{4}u^{2,m} + \frac{3}{8}u^{3,m}$$

Table 2.1: *Numerical differentiation schemes for calculating the derivatives on the cell boundaries and the quadratic extrapolator used at the edge of the computational domain.*

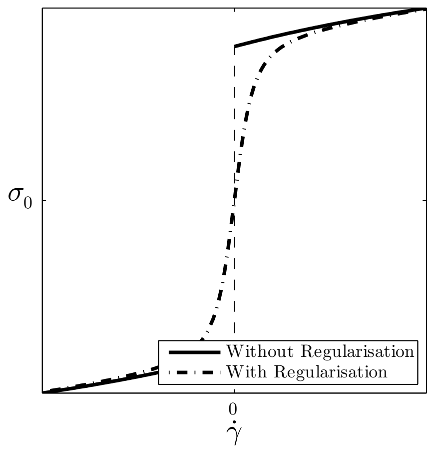

Figure 2.9: *Regularisation of shear stress at zero strain.*

and equation (2.24) becomes an inequality there. For such regions to start shearing, the yield stress $\tau = \mu_1 p$, which is implicitly defined in the rheology, must be overcome. Full resolution of these areas would require tracking a yield surface and calculating the forces acting at the boundary of the shear free region and considering the region as a rigid body. However, as these regions are small compared to the bulk of the flow, this added complication gives a negligible increase in accuracy at the expense of considerable computational complexity. We can therefore relax this condition by introducing a small regularisation parameter ε such that

$$|\dot{\gamma}| = \sqrt{\left(\frac{\partial u}{\partial z}\right)^2 + \left(\frac{\partial u}{\partial y}\right)^2 + \varepsilon^2}. \tag{2.54}$$

This has the effect of removing the yield stress $\mu_1 P$ and placing an upper bound on the effective viscosity of the material $(\nu_{\text{eff}} = \frac{\mu P}{\varepsilon})$. As a result, a small creep velocity appears in regions that would otherwise be static. A similar procedure is followed with the absolute value of the slip velocity used in the calculation of the wall stress to aid convergence, whereby $|u|$ is replaced with $\sqrt{u^2 + \delta^2}$ for another small parameter δ.

Using the grid system defined above, the inertia on the left hand side of equation (2.46) can be further simplified. Using the grid with a scaled z coordinate such that $s = z/h(x)$ allows us to write

$$\left.\frac{\partial u}{\partial x}\right|_z = \left.\frac{\partial u(x, h(x)s)}{\partial x}\right|_s - \frac{s}{h}\left.\frac{\partial u}{\partial s}\right|_x \frac{\mathrm{d}h}{\mathrm{d}x}. \tag{2.55}$$

Then, using the local conservation of mass

$$w = su\frac{\partial h}{\partial x} - \frac{\partial}{\partial x}\left[h\int_0^s u(x,s)\ \mathrm{d}s\right], \tag{2.56}$$

gives the inertia of the element as

$$\rho\left(u\left.\frac{\partial u}{\partial x}\right|_z + w\left.\frac{\partial u}{\partial z}\right|_x\right) = \rho u\left.\frac{\partial u}{\partial x}\right|_s - \frac{1}{h}\left.\frac{\partial u}{\partial s}\right|_x \frac{\partial}{\partial x}\left.\left[h\int_0^s u\ \mathrm{d}s\right]\right|_s \tag{2.57}$$

in this scaled coordinate system. The second term on the right hand side of this equation is written in terms of the partial mass flux $h\int^s u\ \mathrm{d}s$. As such, the derivative takes the value 0 at both the base, where the partial mass flux is 0, and the free surface where, since there is no cross slope velocity, the total mass at a given y-coordinate is fixed. As the Lagrangian description of the flow is captured by the first term, we elect to ignore the second term in the subsequent analysis. We also note that, if the flow field is separable, then this integral term is automatically 0.

In this formulation we are essentially treating x as a modified time coordinate. In a usual application of an initial value problem we use the time coordinate to look at the evolution of the initial condition. In our case we use x as a modified time coordinate such that the typical $\partial_t u \sim 1/2\partial_x u^2$. This allows us to use built-in MATLAB solvers for the problem. However the standard solvers had difficulty in producing solutions for the resultant system of equations due to the stiffness in the system. Instead, we use a specialised solver `ode15s` which is a first-order, multi-step, stiff ODE solver. This gave rapid convergence to the solution.

The numerical approach was as follows:

1. Extrapolate velocity field quadratically half a grid space to the boundaries;
2. Substitute in velocity boundary conditions;
3. Calculate height using mass flux;
4. Calculate derivative quantities and stress tensor using central differences;

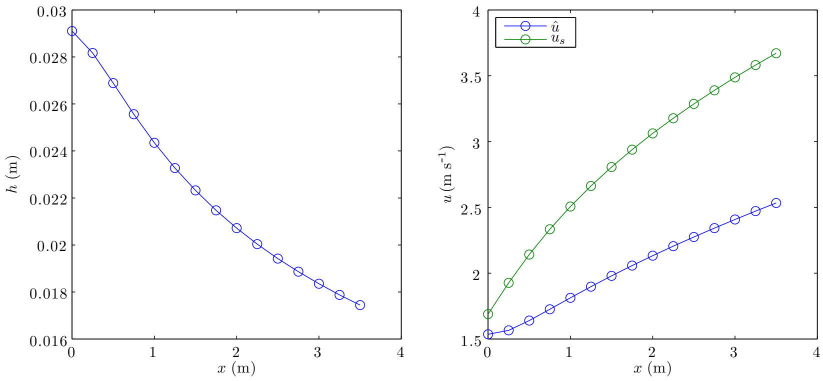

(a) Height (b) Velocity

Figure 2.10: *The development of the height and the average velocity of the flow as it progresses down the slope. Panel (a) shows the development of the height and panel (b) shows the development of both the average velocity $\widehat{u}$ and the average surface velocity u_s. The parameters used for the flow were $\theta = 38°$, $q = 17.8\,\mathrm{kg\,s^{-1}}$, $\mu_1 = 0.54$, $\mu_2 = 0.68$, $I_0 = 0.3$ and $\mu_\mathrm{w} = 0.45$. The grid had 20 divisions in the z direction and 60 in the y direction.*

5. Substitute in the stress boundary conditions at the walls;
6. Take divergence of the stress tensor;
7. Use `ode15s` to calculate velocity field for chosen x values.

The strong non-linearities in the problem obstruct the use of high order discretization schemes and, in particular, a pseudo-spectral Galerkin method produced solutions that degenerated into noise after a few iterations.

2.3.3 Numerical Results

Figure 2.10 shows the development of the height and mean velocity of a typical flow at an inclination just above the maximum friction angle ($\theta > \theta_2$). As expected, we can see that the flow accelerates and thins. Figures 2.11 and 2.12 show the internal properties of the same flow at a point $x = 3.5\,\mathrm{m}$. The velocity profile in figure 2.11(a) agrees qualitatively with expectations; the velocity is greatest at the free surface, and decreasing toward the boundaries. The profile of I in figure 2.11(b) has some interesting features. There are a number of high I zones: the centre of the base, the upper portion of the side walls and the boundary layer near the free surface, where the inertial parameter is infinite (and so not plot-

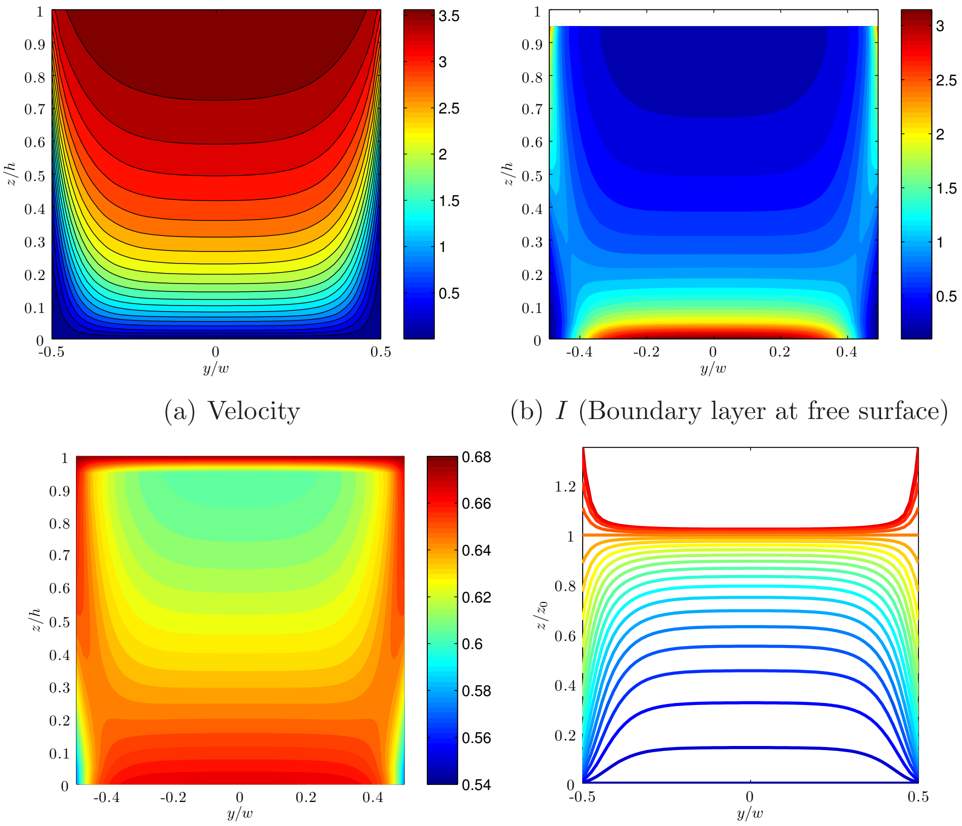

(a) Velocity

(b) I (Boundary layer at free surface)

(c) $\mu(I)$

(d) Separability

Figure 2.11: *Results of a simulation at $\theta = 38^\circ$ and $q =$ 17.8 $\mathrm{kg\,s^{-1}}$, 3.5 m after release. Each panel shows the values of a field in a cross section of the chute. The boundary layer in panel (b) can not plotted as I is infinite on the top row of cells. An increase in resolution of approximately 100 times would be necessary to visualise the boundary layer in I. The final panel shows the velocity normalised by the velocity profile $u(y, z_0)$ and demonstrates that the resulting velocity field is non-separable. The parameters used are $\mu_1 = 0.54$, $\mu_2 = 0.68$, $I_0 = 0.3$ and $\mu_\mathrm{w} = 0.45$. The height was calculated as $h = 0.017 = 17d$. The resolution was 60 cells wide by 20 cells deep.*

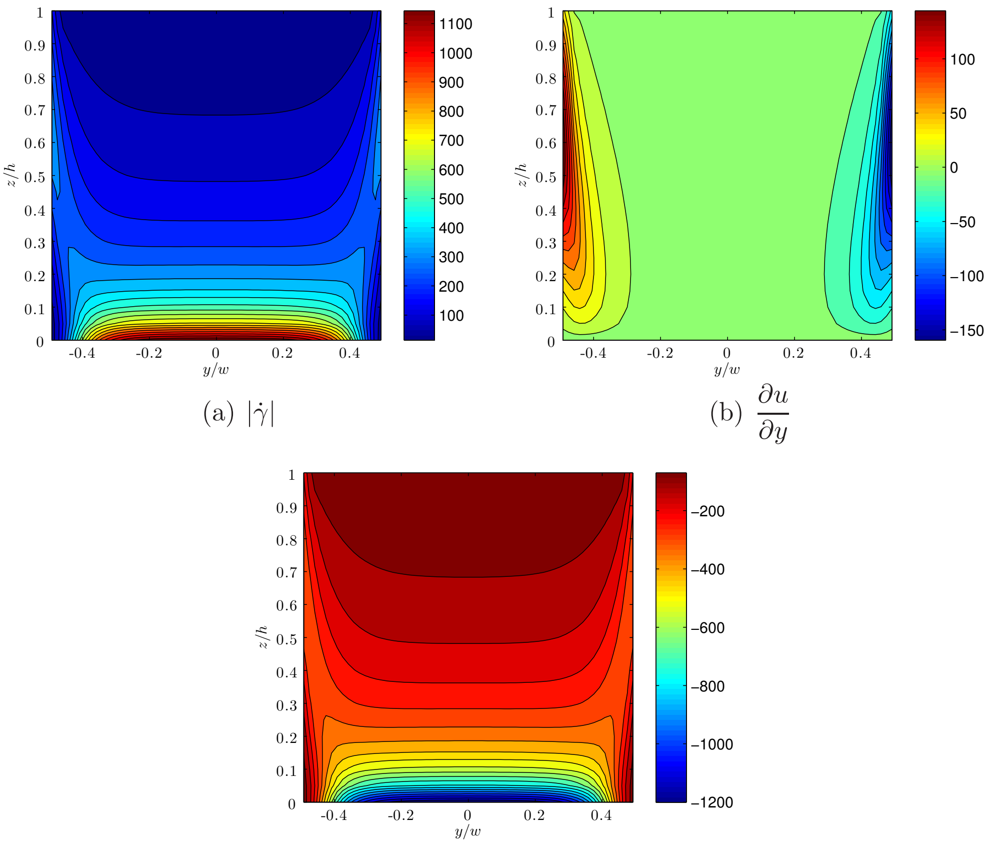

(a) $|\dot{\gamma}|$ (b) $\dfrac{\partial u}{\partial y}$ (c) $\dfrac{\partial u}{\partial z}$

Figure 2.12: *Derivative quantities of the numerically calculated velocity profile at* $\theta = 38°$ *and* $q = 17.8\,\mathrm{kg\,s^{-1}}$, *3.5* m *after release. Same parameters as figure 2.11 are used.*

ted). Using numerical data, we can use equation (2.51) to estimate the size of the boundary layer. A typical value for u_y at the surface for the simulations presented in figure 2.11 is 1, meaning that the boundary layer has size $z/d = 0.02$. The maximum value of u_y at the surface is higher at 44 but is concentrated very near the walls, where the assumption of a Bagnold background profile, and therefore equation (2.50), is invalid. This length scale is too small to affect the grains for the size of the flows investigated here. This is to be expected as a large change in I only elicits a small change in $\mu(I)$ and therefore $\boldsymbol{\sigma}$, since $\mu \to \mu_2$. This can be seen in figure 2.11(c). The resolution of the simulations presented here would need to increase by an order of around 100 to smoothly capture the change in I over this boundary layer. As such, the top row of cells in figure 2.11(b) represent those with infinite I and therefore are not plotted.

Figure 2.11(d) shows the velocity field normalised by the transverse profile taken at some arbitrary depth. Since the profiles are not just constant multiples of each other, the functional form of the velocity is not separable, i.e. it cannot be represented by the form $u = U(x)f(y)g(z)$, meaning that the transverse and depth effects are intimately related.

Figure 2.12 shows the smoothly changing derivatives of the velocity field used in the calculation of I and the stress tensor $\boldsymbol{\sigma}$. We note that from figure 2.10 if we take values for u_s and h at 3.5 m down the slope then the average vertical shear is $200\,\mathrm{s}^{-1}$. Figure 2.12(c) shows that most of the vertical shear is concentrated in a thin zone near the base and so the frictional losses are highest there.

Integrating the $\mu(I)$ rheology over the width of the chute and the height of the flow, we can formulate a total friction with contributions from the basal friction and the wall friction:

$$\mu = \mu_{\mathrm{w}} \frac{h}{w} + \mu_b. \tag{2.58}$$

Using this representation it is clear that, as the flow accelerates and thins, the friction decreases. This total friction is the characteristic friction that we can measure by looking at the development of the averaged surface velocity in our experiments. Figure 2.13 shows the total friction for calculations carried out with the same mass fluxes and inclinations as our experimental data, showing that the largest values of μ_t are never much larger than μ_2. A fuller comparison between the two will be carried out in chapter 4.

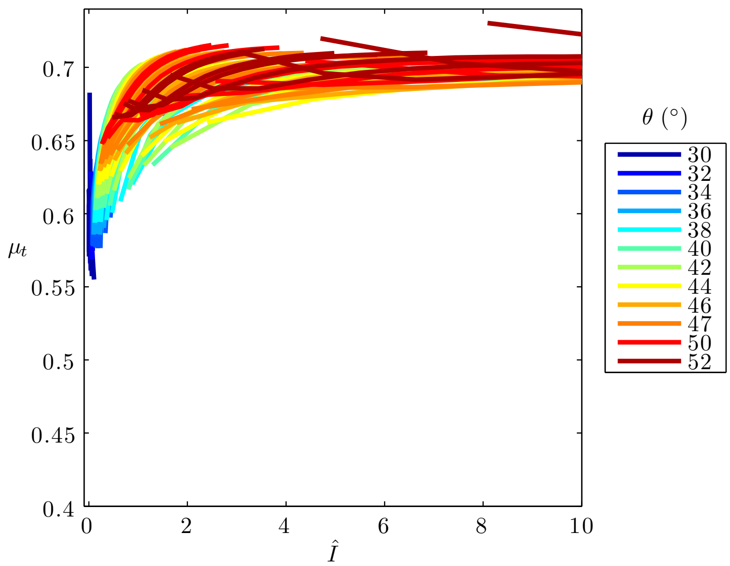

Figure 2.13: *Numerical simulations of the total friction μ on a rough base with $\mu_2 = 0.68$ and $\mu_{\mathrm{w}} = 0.45$. The friction decreases as the flow thins and the frictional force from the wall gets smaller.*

2.4 Conclusions

In this chapter we have described the $\mu(I)$ rheology and shown how it was motivated from inclined plane experiments. We have discussed the subsequent development of a tensorial, 3D theory to formulate a rheology that is usable for a general granular flow. We have assessed the validity of the rheology, and found that it generally gives good agreement with experimental data for flows that are not affected by boundary interactions, or near to the quasi-static or kinetic limits. We have developed a first-order finite volume code in order to produce the velocity profiles for a material obeying the $\mu(I)$ rheology in a chute, so that it may be compared to the experimental observations in chapter 4.

3

Experimental Preparation

3.1 Introduction

This chapter covers the design and operation of the recirculating chute used to collect the experimental data presented in this thesis. As mentioned in chapter 1, in order to investigate a developing flow it is necessary to take measurements at multiple times and/or multiple points along the direction of development. Traditionally the length of time for which measurements can be made is dictated by the amount of material stored in the apparatus, which at high flow rates means that the available time is very short — a primary reason why previous studies have focussed on steady, fully developed flows. For our chute, this problem is solved by using a recirculation mechanism which supplies a steady flow of material and is isolated from the conditions in the chute. The technical details and methodology of the instrumentation and calibration routines used to collect data are also described in this chapter.

3.2 Chute Design

3.2.1 Overview

Our flows are generated by the equipment shown in figures 3.1 and 3.2. A crucial feature of the apparatus is the recirculation mechanism. The recirculation process starts with roughly 2000 kg of sand at rest in the collection hopper (A). This is fed to a screw conveyor (B) which, when operating at its maximum capacity, can move $22\,\mathrm{kg\,s^{-1}}$ of material to the bucket conveyor (C). This lifts the material 6 m vertically to the feed hopper (D). The feed hopper contains an overflow pipe (G) that ensures a constant head of sand is maintained. This is necessary to ensure a constant flow rate since our hopper is too small for the exit conditions to be fully governed by the Janssen effect (Janssen, 1895). The exit of the hopper consists of a rectangular aperture of width 225 mm and of variable length which is controlled by a screw attached to a pulley. The angular position of the screw is given by a digital rotary encoder with one degree of rotation equivalent to 0.0139 mm of linear travel, giving very fine control over the aperture geometry. The aperture length can be anywhere from fully closed to 225 mm at its maximum. The sand falls freely from the aperture onto the chute (E) so that the conditions inside the chute do not affect the mass flow rate. The chute is mechanically isolated from the recirculation system so that vibrations do not affect the flow of the sand or the measurements. The inclination of the chute can be varied from 15° to 55° and is measured to an accuracy of 0.1° by a digital inclinometer. There were small variations in the inclination along the chute of around 0.1° due to it flexing under its own weight. The chute itself is 4 m by 0.25 m, of which the entire width and 3 m of length are observable experimentally. Whilst in the chute, measurements are made by instrumentation mounted on a hand operated traverse (F) located above. Finally, the sand falls freely from the chute onto the return chute (H) which deflects the sand back into the collection hopper. The machine is enclosed to contain dust and there is an extensive ventilation and filtering system which removes the finest particles from the material and the air in the laboratory.

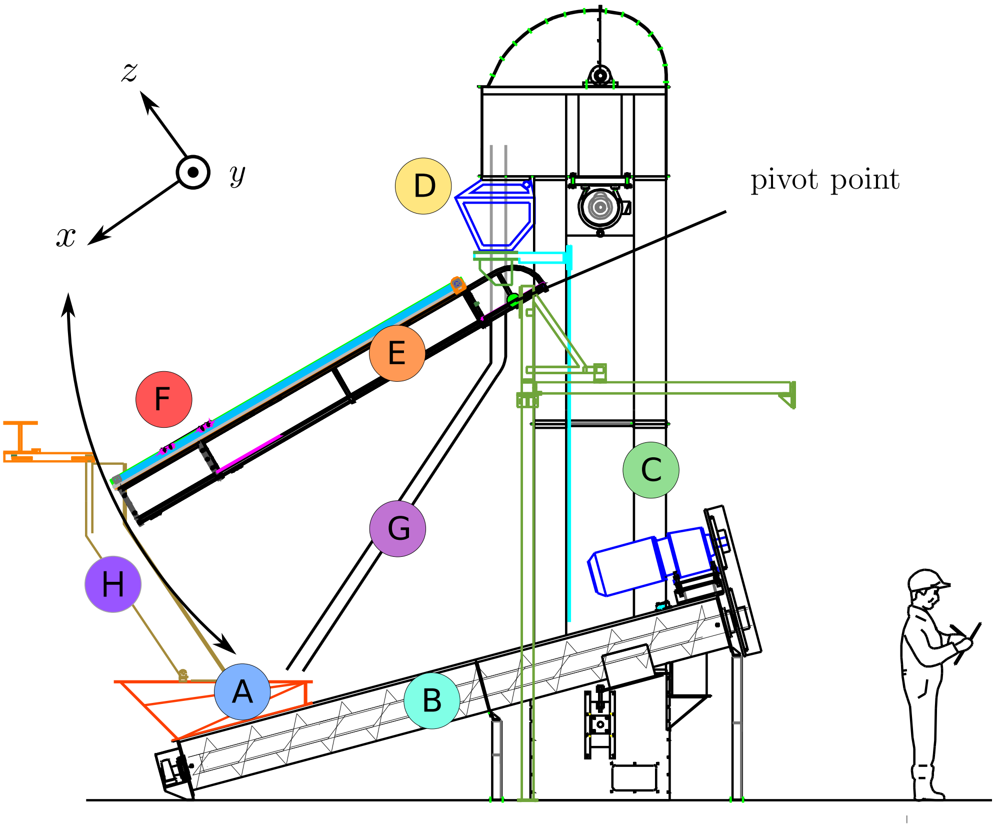

Figure 3.1: *A diagram of the chute and the recirculation mechanism. (A) Collection Hopper (B) Screw Conveyor (C) Bucket Conveyor (D) Feed Hopper (E) Chute (F) Instrumentation and traverse (G) Overflow (H) Return Chute.*

Figure 3.2: *Photograph of the Apparatus, including the recirculation mechanism, chute and instrumentation. The dust containment system has been partially removed for clarity.*

3.2.2 Recirculation Mechanism

The recirculation mechanism consists of two main components — the bucket and screw conveyors. The screw is used to move the sand laterally from the collection hopper at the bottom of the chute to the base of the bucket conveyor. Over this distance, the sand is also lifted vertically around $1\,\mathrm{m}$ so that it may fall into the up-going buckets. The screw is powered by a user-controlled motor rated at $22\,\mathrm{kW}$. The user can alter the mass flux of the screw from $1\,\mathrm{kg\,s^{-1}}$ up to $22\,\mathrm{kg\,s^{-1}}$ in intervals of less than $5\,\mathrm{kg\,s^{-1}}$ by means of a control panel. Fine control over the mass flux is via the hopper exit geometry. The designed maximum throughput for the screw is $36\,\mathrm{kg\,s^{-1}}$, but it is limited to $22\,\mathrm{kg\,s^{-1}}$ to increase longevity and minimise the impact of any overflow that may occur in the chute for lower inclinations.

The bucket conveyor system which lifts the sand through around $6\,\mathrm{m}$ vertically is powered by a $11\,\mathrm{kW}$ motor and is capable of moving $40\,\mathrm{kg\,s^{-1}}$ of material from the screw conveyor to the hopper. The speed of the buckets is not controllable by the user and operates at a fixed rate such that a maximum flux of $30\,\mathrm{kg\,s^{-1}}$ could be moved. Setting the bucket flux above the maximum flux of the screw conveyor avoids the problem of the buckets overfilling. This can lead to the bucket enclosure filling with sand and jamming the recirculation mechanism.

3.2.3 Hopper and Initial Conditions

Design

After the recirculation mechanism, the sand enters the hopper before entering the chute. The hopper's design is therefore critical in ensuring that the flow in the chute is as uniform as possible whilst maintaining isolation between the sand in the chute and the rest of the apparatus.

A large hopper can help with maintaining isolation between the hopper's exit flow and conditions at the top of the bulk where, in our case, there is a periodic forcing generated by the impact of the sand falling from the buckets. Another advantage of having a large hopper has been known since the earliest systematic studies of granular behaviour. Even before the study of Janssen (1895), after whom this effect was named, it was known that the pressure at the base of a hopper was a weak function of the total amount of material above the exit. Janssen found that the frictional nature of the grains caused the hopper walls to bear some of the particles' weight (in contrast to the behaviour exhibited by a liquid) and that the bottom pressure tends to a limit as the total mass in the hopper increases. Since the mass flux q out of the hopper must be a function of the stress state, and therefore the pressure at the exit, Janssen's observation therefore means that if the material is sufficiently deep, the flow out of the hopper is independent of the amount of granular material stored above it. Nedderman *et al.* (1982) review a number of studies for different grains, which give estimates of the depth needed to reach this threshold. These are all of a similar order of magnitude: the height of the material should be of the same order of magnitude as the aperture size. From this point of view, the larger the hopper the better.

However, the laboratory housing the chute has a finite height and restricts the maximum size of the hopper. We are faced with a compromise as the smaller the hopper, the longer the chute can be, and the larger the range of inclinations can be studied. To balance these two considerations, the hopper's final height was chosen to be around 5 times the maximum aperture width. This gave a good range of available inclinations, whilst ensuring that the exit flow has only a weak dependence on the total mass in the hopper.

To increase the length of the observable chute whilst allowing the top of the bucket conveyor to be packaged, an asymmetric hopper design was chosen, with the entry point for the sand not directly above the exit. This had the slight complication of inducing non-symmetric velocity profiles at low flow rates, as well as introducing large static zones into the hopper. The solution to these problems is discussed later. The final hopper design can be seen in figure 3.3.

The introduction of an overflow pipe into the hopper removed the problem of the exit flow's dependence on the mass in the hopper completely as it maintains a constant head at all times. Sand in the overflow goes directly to the collection hopper at the base of the chute, where it is recirculated. It also removed the risk of the hopper overflowing, which could cause lasting damage by jamming the bucket conveyor. It also provides a simple way of limiting the mass flux into the hopper without resorting to elaborate control strategies regarding screw speed and bucket rate.

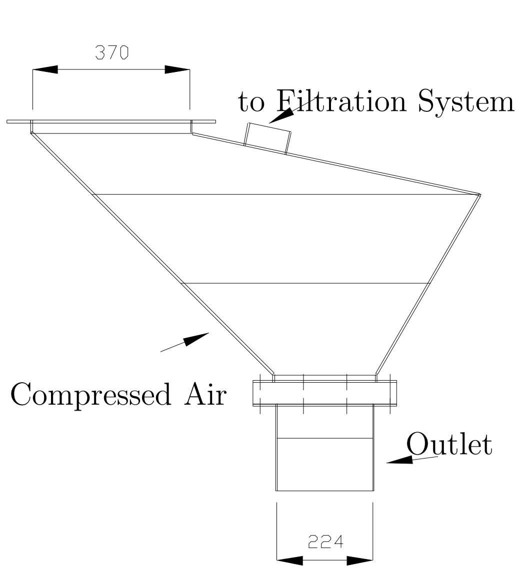

(a) Front view

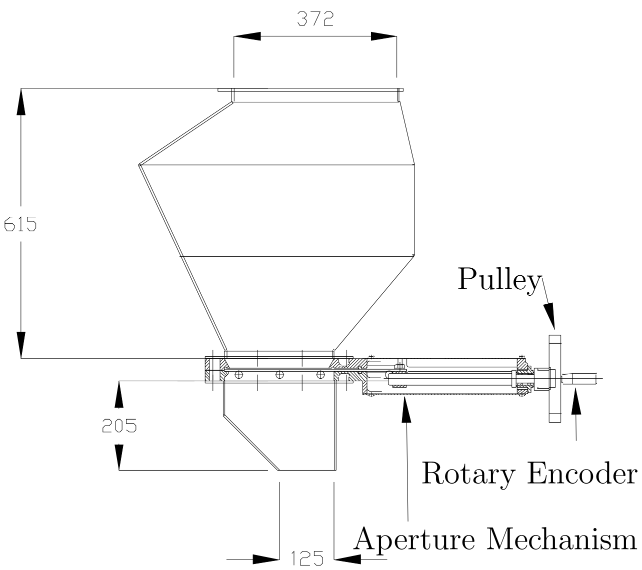

(b) Side view

Figure 3.3: *Front and side view of the hopper. Pictured are the aperture mechanism which consists of a sliding plate attached to a fine-pitch screw, a digital rotary encoder, a compressed air valve to fluidise the grains in the hopper and the suction point used to evacuate dust. Dimensions are in* mm.

The exit flow of a hopper is known to depend heavily on the exit geometry (Nedderman *et al.*, 1982); manipulating the geometry precisely allows fine control of the mass flux. To this end, we use a sliding plate attached to a fine-pitch screw which gives a linear travel of 0.0139 mm per degree of rotation. This is attached to a digital rotary encoder which gives the angular position to the nearest degree. The plate has a fixed width of 225 mm, and a variable length, l, which varies from 0–225 mm. The maximum mass flux that can be supplied by the screw and buckets is achieved at an aperture length of approximately 80 mm.

Initially it was noticed that the mass flux could vary considerably for a given aperture size between experiments. A brief look at the flow within the hopper suggested that the hysteresis of dry granular materials was causing different flow states to form within the hopper each with different sized static zones which affected the repeatability of the flow.

To remedy this, on one side of the hopper a compressed air line was fitted approximately 30 cm above the aperture. This fluidised that boundary and removed the large static region from the hopper, helping to reduce the effect of the hysteresis.

In addition to this, a fixed startup routine was developed which produced repeatable flows:

1. Open the aperture to 80 mm;
2. Set the screw feed to maximum flux;
3. Wait for the hopper to fill above the level of the overflow;
4. Change to the desired aperture size;
5. Alter screw speed to reduce the overflow flux. (This reduces unnecessary particle degradation).

These two additions were found to produce repeatable mass fluxes for a given aperture size with an estimated error of less than 2%. The remaining variation in the measurement for a given aperture size can be attributed to a combination of measurement error (as discussed in the next section) and different random loadings of the hopper.

Calibration

Independence of the flow state in the hopper and the chute allows the flow rate q to be calibrated against the aperture size l thus saving the need to check the mass flux of each experiment. We do this by choosing an aperture size, waiting for a steady flow to develop and then swinging a large, rigid nylon bag underneath the end of the chute. The nylon bag is connected to a crane via a crane scale which gives the weight of the bag and its contents with an error of $\pm 100\,\mathrm{g}$ at a sampling rate of around $10\,\mathrm{Hz}$. The factory software supplied with the crane scale only supplied data at around $1\,\mathrm{Hz}$, a level of accuracy that gave errors of $\pm 20\%$ for the highest mass fluxes and so custom software was reverse engineered, details of which are in appendix B.

We calculate the mass flux q as follows. The crane scale measures a force

$$F(t) = g \int_0^t q(t')\,\mathrm{d}t' + qv + m_{\mathrm{bag}}\,g \tag{3.1}$$

for a flow with mass flux q entering the bag of mass m_{bag} at a mean velocity v. These three terms are the weight of the sand in the bag, the impulse imparted to the bag upon impact and the weight of the bag respectively. Assuming a constant impulse qv gives the flux q as

$$q = \frac{\partial_t F}{g}. \tag{3.2}$$

Figure 3.4(a) shows the mass in the bag as a function of time for various aperture lengths. The trend shows a constant mass flux over intervals larger than the sampling time of $0.1\,\mathrm{s}$. The uncertainty in the flow rate measurement was less than 1%.

A scaling law for the mass flux in terms of the aperture size of a cylindrical hopper with a conical base was discussed by Beverloo *et al.* (1961). We proceed by noting that, if we consider the case $l \gg d$, then the mass flux q exiting the hopper should scale as

$$q \sim \rho v W l \tag{3.3}$$

for some characteristic velocity v at the exit of the hopper. Since the particles are in free fall when exiting the hopper, this velocity can be expected to scale as the result of being accelerated by gravity over a distance comparable to the aperture

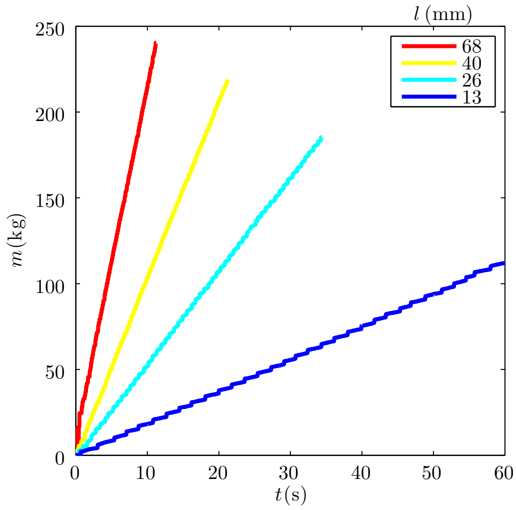

(a)

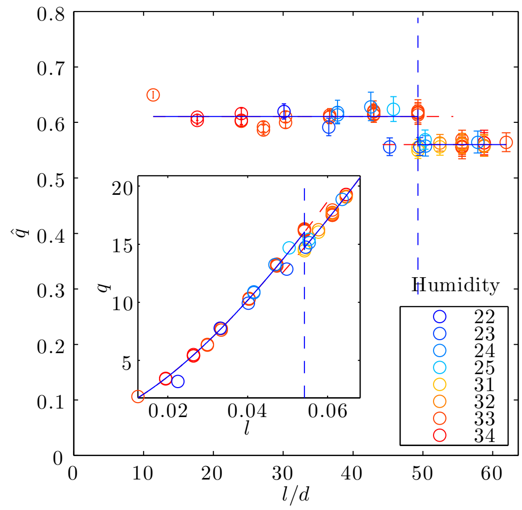

(b)

Figure 3.4: *The mass flux, q as it varies with the aperture length l. (a) Variation of mass flux over time for different aperture openings (b) Non-dimensional mass flux $\hat{q} = q/\rho W\sqrt{gl^3}$ as a function of dimensionless aperture opening l/d. Inset of (b) shows the dimensional flux q with units $\mathrm{kg\,s^{-1}}$ in terms of the aperture length, l, in m. The error bars show the maximum error due to quantisation.*

length l, i.e.

$$u \sim \sqrt{gl}, \tag{3.4}$$

giving an expected scaling of

$$q \sim \rho W\sqrt{gl^3}. \tag{3.5}$$

The flow rates for our hopper with its slightly unusual geometry are non-dimensionalised by this scaling to give $\hat{q} = q/\rho W\sqrt{gl^3}$. Figure 3.4(b) plots $\hat{q}$ with the dimensional data, q, shown in the inset. We can see that this scaling collapses the data very well, however the value of $\hat{q}$ changes half way through the interval we are interested in: above aperture lengths of 52 mm the flow enters a slightly different regime where $\hat{q}$ alters slightly. The reasons for this are unclear. The dependence of this mass flux on humidity and particle size has been checked and is negligible. The scatter in figure 3.4(b) is due to different random loadings of the hopper.

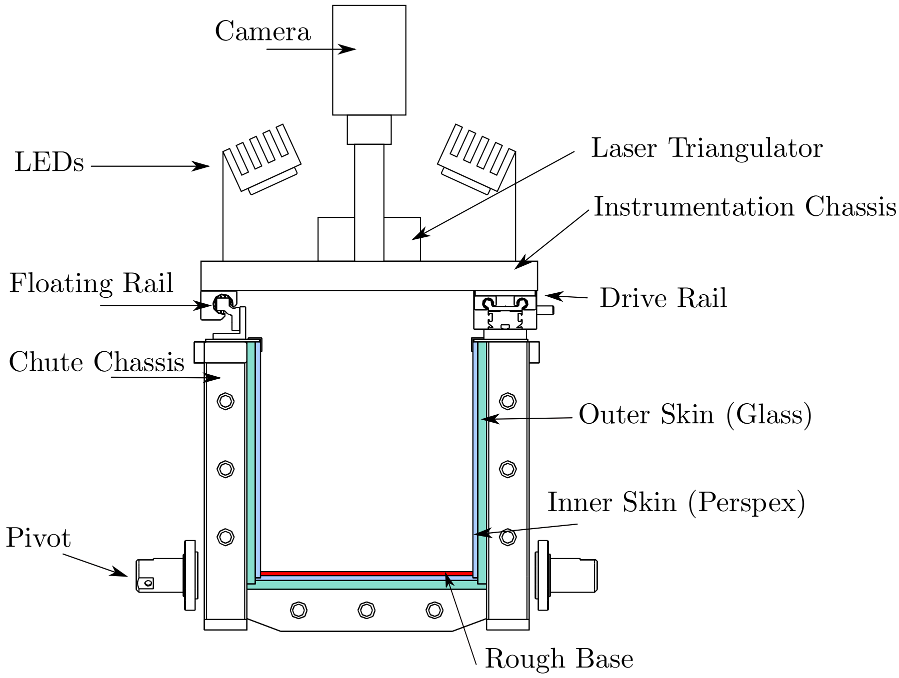

Figure 3.5: *Cross section of the chute showing the measurement systems and the rails used to alter their x position.*

3.2.4 Surface conditions

The experimentally observable portion of the chute consists of a modular steel chassis and two layers of lining. The outer skin is an acrylic layer and is attached permanently to the chute. The second, inner skin is made out of perspex, which is slightly more scratch resistant and is designed to be easily replaced or substituted for another material. The construction can be seen in figure 3.5.

During flow, the grains lightly scratch the surface of the perspex which changes the surface condition initially. However, this process soon reaches equilibrium with the result that the surface exerts a Coulomb-like frictional stress on the sand with coefficient $\mu_{\mathrm{w}} = 0.45$. This permits a slip velocity, unlike a Newtonian fluid near a boundary (see section 3.4.2 for more details).

The flow is bounded by two rigid side walls, a rigid base, and a free surface. The side walls in all experiments are made of the smooth perspex. However, two basal surfaces are used. One is the smooth perspex referred to above, and the second is a rough base which is constructed by overlaying the smooth base with a

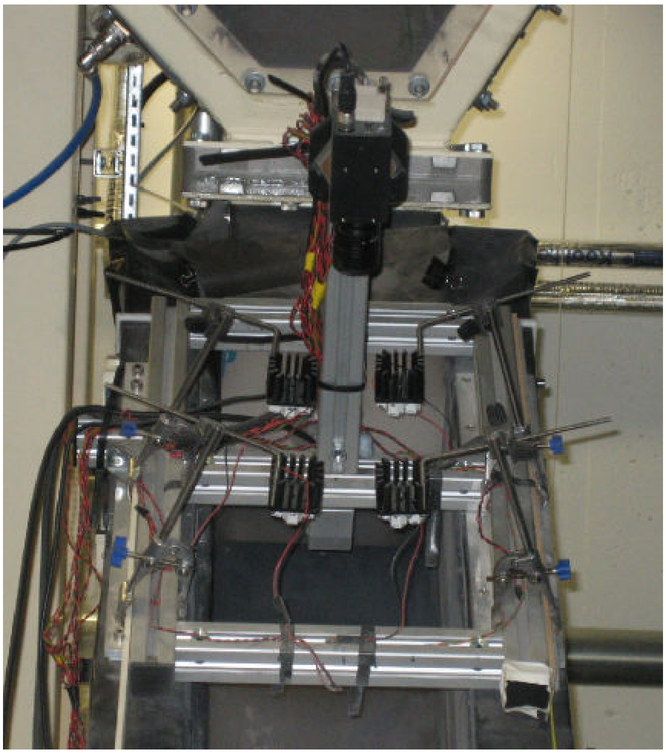

Figure 3.6: *Photograph of the instrumentation traverse. Visible are the LED strobes, the laser triangulator and the camera.*

layer of coarse grit sandpaper (P40 grade). This has an average particle diameter of 0.425 mm, which is sufficiently large to impose a no-slip velocity condition at the base for shallow angles. At high particle velocities however, the sand skips over the bumps in the base, leading to a complicated boundary condition.

The asymmetry of the hopper caused a non-symmetric velocity profile in the chute for low flow rates. To remedy this, a weir, around 30 mm high, was placed near the top of the chute just below the point where the sand falls from the hopper. This causes the particles to slow down slightly, increasing the pressure, causing them to spread evenly across the entire width of the chute. At higher mass fluxes, the velocity profile is already symmetric and the weir has little effect on the flow.

3.3 Measurement Systems

The chute is equipped with two measurement systems: a camera used to record surface velocities, and a laser triangulator used to record the surface height. Using these two fields, the Froude number Fr, the dimensionless height n, and the surface acceleration and friction coefficient can be measured. Each system is controlled by a separate computer (see figure 3.7). The first generates the high-precision timing pulses needed to synchronise the camera and the flash and stores the recorded video. These pulses are also used by the second computer which records the height data, allowing a height profile to be matched to its corresponding video frame. The height measurements are also used to remove parallax effects from the velocity measurement.

3.3.1 Flow Height Triangulation

The height of the flow, $z = h(x, y)$, is measured using a Micro Epsilon LLT2800-100 laser triangulator. This is a line-optical system which projects a laser sheet onto the surface of flow. The back-scattered light from the laser sheet is then focused using a high quality optical system and registered by a CMOS array, as shown in figure 3.8. The CMOS array is designed such that the illumination, readout and processing stages can happen simultaneously, thus allowing a high

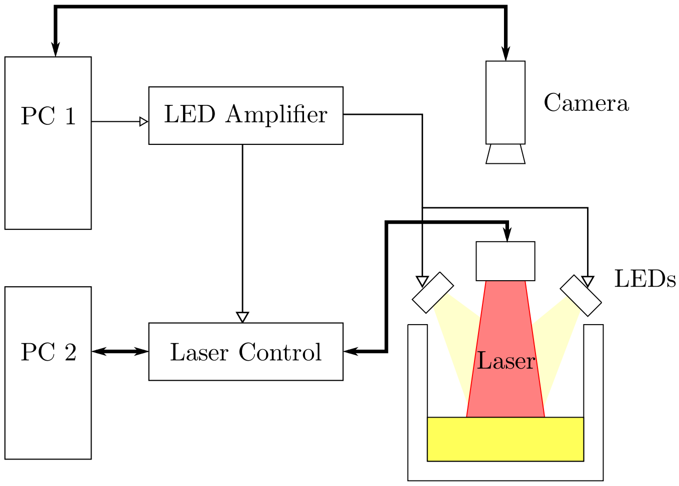

Figure 3.7: *Schematic of the measurement systems. One computer controls video capture and timing pulse generation. The second captures and processes height information from the laser triangulator. It also counts the timing pulses which are used to match the video frames to a height reading.*

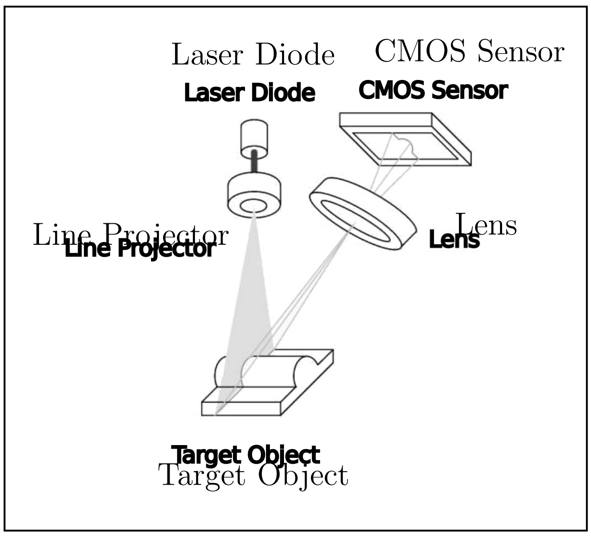

Figure 3.8: *Schematic of the triangulation process used to measure the flow height. A laser is shone onto the surface, and the distance calculated from the reflected light.*

data throughput. This system provides both the height (z) and the lateral (y) coordinates. It outputs both values to the PC via a firewire interface and read by custom software, which was developed in C++. The software writes the coordinates to a custom file format, which is read by MATLAB for post-processing. Details can be found in appendix C.

The laser triangulator is capable of calculating 256,000 coordinate pairs per second with a maximum of 1024 points in a profile, or at a maximum rate of 1000 profiles per second. The maximum length of the measurable area is 140 mm laterally with a maximum surface deviation of 100 mm in height. The accuracy of the points is 0.04 mm for a surface with ideal optical properties.

We have chosen to record 100 points per profile in our experiments which corresponds to a spatial resolution of around 1 mm, or less than a particle diameter, between points. We read data at 400 profiles per second, quick enough to resolve our quickest flows to within 1 mm of surface travel. We collect 10 s of data for each position down the chute, either with the laser sheet perpendicular or parallel to the direction of the flow. No significant difference in the mean flow height was seen between the orientations. In practice, due to the slightly sub-optimal optical properties of the sand and the inevitable build up of a thin layer of dust on the lens, the error of the readings is slightly larger than the manufacturer's specification at approximately 0.2 mm, but is still significantly less than the median grain diameter. The central 120 mm of the flow are measured, with the height typically varying by less than two grain diameters across the slope.

Care must be taken to avoid measurements of saltating particles as they obscure the dense bulk of the flow that we are interested in. Taking a median average removes the effect of these outliers. Particles that are too close to the laser sensor are out of the depth of field and are given a special value by the hardware so that they may easily be removed from the data.

Calibrating the sensor to record the flow height is a simple procedure as the equipment is calibrated at the factory with some reference surface, all that has to be done is subtract the difference between the reference surface and the distance to the base of the chute.

The height data presented in the experimental results have been time-averaged over all of the recorded profiles at that x coordinate. For single point data, we also take an average across the profile (in the y direction).

In addition to providing the height data, the triangulator is also used to remove parallax effects from the surface velocity measurements which will be explained in more detail in the next section.

3.3.2 Surface Velocity

There are a number of techniques for calculating the velocity of a material, most of which were initially developed for either solid surface displacements or transparent fluid flows. These include Laser Doppler velocimetry and hot-wire anemometry. However, these two techniques are unsuitable for a granular material as its opacity and athermal nature prevent their use. Instead, we use a comparatively recent technique called Particle Image Velocimetry (PIV) which is in widespread use in the granular field (Eckart *et al.*, 2003; Willert *et al.*, 1996) . This technique has the advantage of producing a two-dimensional picture of the surface velocity, and is a truly passive technique for granular flows. This technique is based on analysing differences between frames in a video sequence. We acquire the pictures of the free surface using a JAI CL M4+ camera used in conjunction with a BitFlow R3 frame grabber. A 25 mm lens is used with a 0.95 f-stop. This captures the whole width of the chute whilst giving a sufficient depth of field and illumination of the CCD. The frame rate of the camera is fixed at 24 fps, at a resolution of 1372×1024 pixels. Since the size of each frame in real world coordinates is approximately 0.25×0.20 m, a flow speed of $5\,\mathrm{m\,s^{-1}}$ equates to the particles traversing the full length of the picture between consecutive frames and therefore is too large to identify any similarities between them. This problem can be solved either by increasing the frame rate (thus requiring a new camera), or by exploiting the time-steady nature of the flows and using a syncopated flash with a “frame straddling” technique.

If the flow is steady in time then the description of the flow is insensitive to the length of interval between pairs. However, it is not possible to gain a complete description of the velocity profile with a single pair of images as the presence of statistical noise, both from errors incurred by the pattern matching algorithm and from the grains’ granular temperature, gives uncertainty in the mean velocity value.

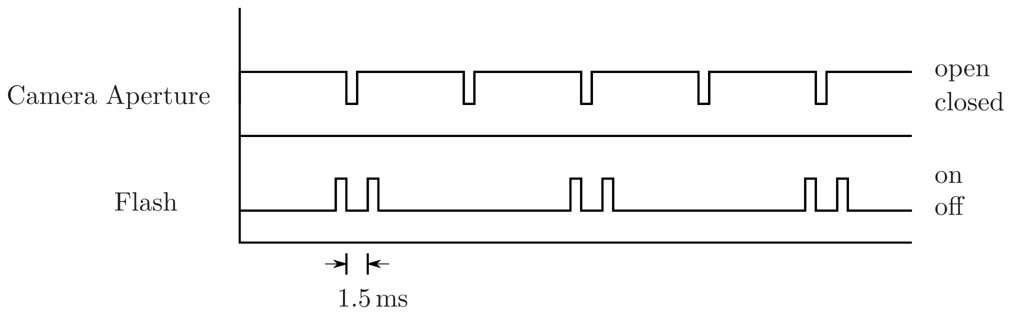

Figure 3.9: *Temporal diagram of frame straddling: a technique developed for steady flows allowing for an increase in temporal resolution using standard photography equipment.*

We solve the issue of having a short interval between images within the pair by having a double flash that straddles the frame boundary. By activating the flash at the end of exposure for the first frame, and the beginning of exposure for the second frame, as shown in figure 3.9, we effectively have a frame rate of around 700 fps for the pair. Over this short time the particles move a few pixels between adjacent frames, which is ideal for the PIV algorithm detailed later in this section.

However, generating this quick double flash requires some non-standard technology. Incandescent bulbs of the type used for traditional camera flashes do not have a sufficiently fast response time for this purpose. They also require a huge amount of power to be delivered over the short interval that they are on. Previous attempts to solve this problem have used multiple sets of bulbs, however, since they must necessarily be in different positions, they subtly change the pattern observed by the camera, thus reducing the quality of the PIV measurement. Instead, we use four banks of five high-powered LEDs. This avoids the need for multiple sets of bulbs as they are relatively low power — a bench power supply switching directly through a transistor is sufficient to power them all. Each bank is rated at 14 W (continuous rating), giving approximately 200 lm of luminescence.

The timing and length of the pulses used to fire the LEDs are controlled by a combination of two signals. A hardware-produced square wave synchronizes with the transfer of the lines in the camera's buffer and is multiplied by a software-produced wave over which the user has control to specify the temporal location and duration of the pulses.

The length of the LED pulse and the delay from the beginning of the frame transfer is chosen in a trial and error process to achieve a good level of illumination which is even between frames — CCD discharge times can affect the result, causing bleed between frames. The final timings are then checked using a photo transistor and oscilloscope, giving an accuracy of approximately 10^{-5} s. The interval between the flashes is approximately 1.5 ms.

The pictures are taken in a dark environment to minimise blur and some representative images can be seen in figure 3.10.

Particle Image Velocimetry

The transparent flows for which this class of techniques were traditionally developed needed to be seeded with particles in order for the flow to be visualised. These are typically small, neutrally buoyant particles with small Stokes' number to reduce their effect on the flow. For solids, the speckle produced by a laser on an optically rough surface achieves the same effect. The first PIV techniques for fluids used a laser to produce a Young's fringe pattern, which allowed the analogue autocorrelation to be taken and the velocity deduced. A full review of analogue PIV techniques can be found in Grant (1997). For granular flows, the material is sufficiently textured to render the introduction of tracer particles unnecessary, making this technique truly passive. The particular PIV technique used here takes the sequence of digital images as discussed in the previous section, and analyses differences between adjacent frames in software.

The algorithm used to examine the difference between frames is as follows. We define an image taken at time t as I_1, and the next image in the sequence, I_2, is the image taken at $t + \delta t$. We treat these images as mathematical functions representing the image intensity — in our case the grey-scale values of the image.

The algorithm in its most basic form takes a sub-image (the interrogation window) of I_1 and finds the most similar sub-image in I_2. More formally, if we restrict our attention to windows of width w and height h, then we can define $I_n^{i,j}$ as a portion of I_n with its lower left corner at the (i, j) pixel. We take the measure discussed in Gui & Merzkirch (2000) known as the Minimum Quadratic Difference

(MQD) method,

$$D(m,n) = \frac{1}{hw}\int_0^w \mathrm{d}x \int_0^h \mathrm{d}y \left(I_1^{i,j}(x,y) - I_2^{i+m,j+n}(x,y)\right)^2, \tag{3.6}$$

which gives a numerical representation of the difference between the windows. Here, (m,n) is the displacement between the two sub-images. We then search over all (m,n) to find the window in the second image that minimises D and take this as the most likely displacement for the particles in $I_1^{i,j}$. This is converted to a velocity by the formula

$$\boldsymbol{v} = \frac{1}{\delta t}(m,n). \tag{3.7}$$

For digital photographs the intensity maps are discretized and so the integrals in equation (3.6) reduce to sums over the pixels. Since the photographs are necessarily a 2-D representation, any motion perpendicular to the surface can be calculated using the free surface kinematic boundary condition and the height information from the triangulator.

The results of using this measure for two sample images are shown in figures 3.10 and 3.11. For clarity, figure 3.11 plots $1-D$ so that the peak can be clearly seen. The result of the calculation for this example gives a very small displacement in the y direction (as expected), and a large displacement of around 50 pixels in the x direction[1].

Our velocities are calculated using a modified version of the algorithm above. It is taken from the synthetic Schlieren technique developed in Sveen & Dalziel (2005) and gives a subpixel level of accuracy. This increased accuracy is obtained by interpolating the peak of D with a 3-point Gaussian curve fit — the minimum of the interpolated peak is taken to be the displacement. This typically reduces the RMS error of the displacement to less than 0.1 pixels. For our data, this equates to a typical error of approximately $0.01\,\mathrm{m\,s^{-1}}$. The modified algorithm also removes outliers in the velocity field by comparing a displacement vector with its spatial and temporal neighbours. It then re-examines D in the neighbourhood of the neighbours' displacements to see if there is a suitable peak there.

The images are split into a grid of 69 by 51 interrogation windows. This offers

[1]The x displacement in these images has been accentuated by an order of 10 for illustrative purposes. Typically x displacements are 5 pixels between frames.

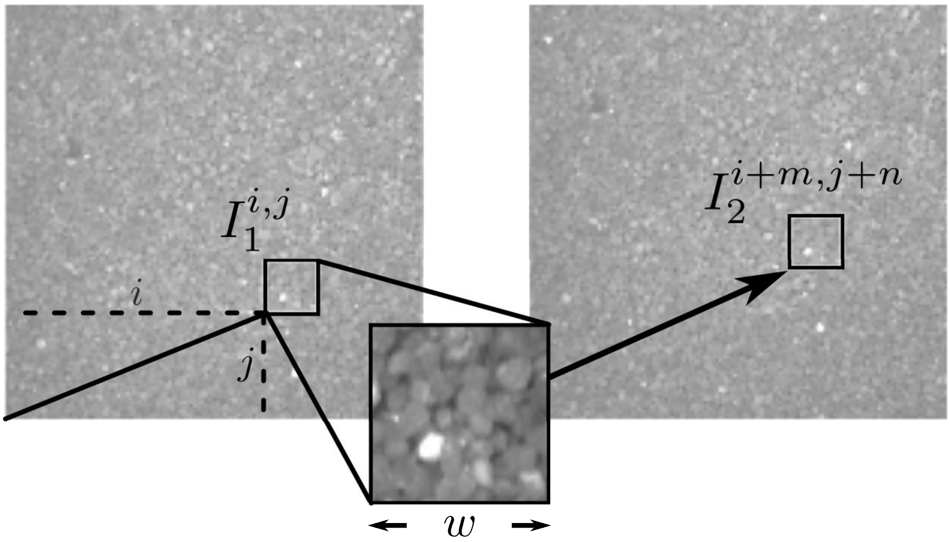

Figure 3.10: *Representation of the displacement calculated by correlating a sub-image of I_1 with the sub-images in I_2.*

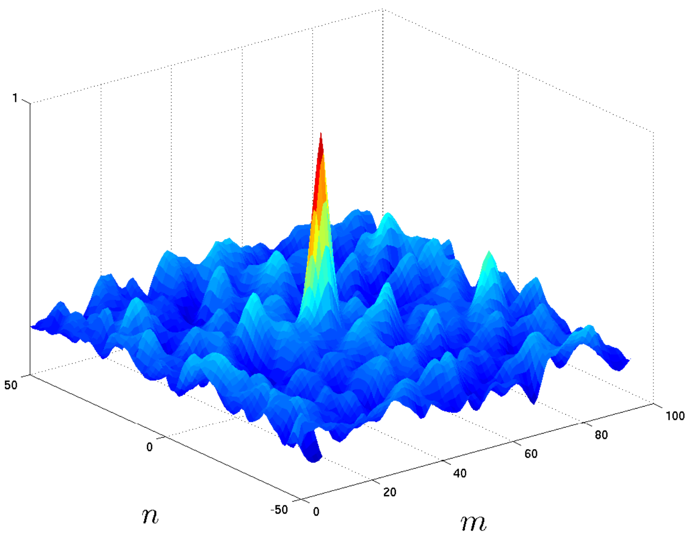

Figure 3.11: *Plot of $1-D$ for different displacements (m,n) of the sub-image $I_1^{i,j}$ seen in figure 3.10.*

a high degree of accuracy whilst keeping the computational cost of the PIV to a reasonable level. The window size corresponds to a rectangle of side length roughly 4 times the particle diameter, giving a level of granularity that allows the pattern matching algorithm to work effectively with the amount of deformation caused by the strain gradient. A smaller area would incur large errors in the calculated development, as individual particles appear very similar and would give a number of strong peaks in the correlation.

For time-averaged data approximately 50 pairs of images are used. For data points that represent the velocity of the flow at a given point down the slope, the velocity field is then also averaged in both the x and y directions. Median averaging is used in both cases.

Calibration

Since the PIV algorithm has no knowledge of real world coordinates, the displacements it gives are in terms of pixels. To convert these to real-world velocities, a mapping must be created between these pixel coordinates and the real-world coordinates. This map may not necessarily be a linear transformation due to lens distortion and parallax effects brought about by the change in flow height. Therefore some care must be taken to ensure the transformation is accurate. To a first approximation, the length of one of the sides of the field of view is proportional to the distance of the camera to the surface. If, as in our case, the camera is approximately 0.7 m away from the surface, then a difference of 0.1 m in the flow height h would incur an error the order of 10% in the calculated velocity. It is therefore important to remove this parallax effect from our calculations.

We proceed by using the chequerboard pattern pictured in figure 3.12 to generate a set of fixed, known real world points. The pattern has sharp contrast edges meaning that the corners can be identified with a high degree of accuracy. The squares have side-length of 25 mm and are flush with the sides of the chute so that the y coordinate origin corresponds to the wall. We use a corner detection method from Harris & Stephens (1988) to calculate the location of the corner to sub-pixel accuracy.

The idea behind this method is to take a small area of the image and compare it to its neighbourhood. If there is an edge in this small area, then there will

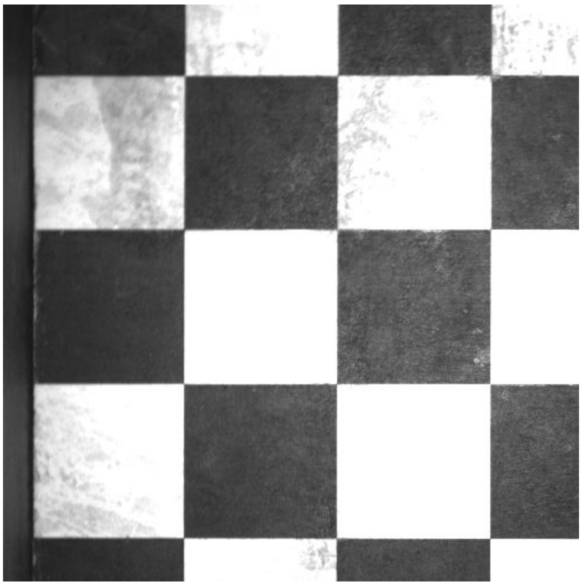

Figure 3.12: *The chequerboard pattern used to locate fixed points with reference to the chute geometry. This allows a pixel to real-world map to be constructed for different flow heights.*

be a minimal difference for displacements along the edge, and a sharp change for displacements perpendicular to the edge. If there is a corner, then there will be a large change in both directions. Consider taking a section of the image of height h and width w and shifting it by $\boldsymbol{x} \equiv (x, y)$. Then, the weighted quadratic difference with weight function $\pi(x, y)$ is given by

$$S(x, y) = \sum_{u=0}^{w} \sum_{v=0}^{h} \pi(u, v)(I(u + x, v + y) - I(u, v))^2. \tag{3.8}$$

Choosing a Gaussian for the weighting, $\pi(x, y)$, we effectively restrict the maximum displacement size to a few pixels. Therefore, we can linearise S in terms of the partial derivatives I_x, I_y

$$I(u + x, v + y) \approx I(u, v) + I_x(u, v)x + I_y(u, v)y, \tag{3.9}$$

which, when written in terms of the structure matrix A

$$A = \begin{bmatrix} \langle I_x^2 \rangle & \langle I_x I_y \rangle \\ \langle I_x I_y \rangle & \langle I_y^2 \rangle \end{bmatrix}, \tag{3.10}$$

gives

$$S = \boldsymbol{x} A \boldsymbol{x}^\top. \tag{3.11}$$

The expression $\langle . \rangle$ represents a weighted sum of the quantity within. For a point (x, y), if there is a corner there, then the eigenvalues of A are large and positive. Sub-pixel accuracy is obtained by iterating the process over the neighbourhood and interpolating the image there. This algorithm is most efficient when an initial guess is supplied by some means. In our routine, the user clicks on the four extreme corners of the grid. As the number of squares is known on each side, we can interpolate between the user-supplied extreme corners to provide initial points for the corner finder algorithm to use on all of the internal points. This way, we generate a full grid of mappings between pixel coordinates and world coordinates.

Once the map between the control points has been produced, we use the MATLAB function `cp2tform`, which provides a locally-weighted mean interpolation for coordinates not on the grid. This routine removes the effects of distortion for small amounts of fish-eye curvature.

To remove parallax from our calculation we use the camera and laser triangulator in tandem to photograph the calibration pattern at different distances from the camera. We stick the chequerboard pattern onto a rigid surface and alter the distance to the camera in $\sim 10\,\mathrm{mm}$ intervals. The above routine is performed at each level to create a full three-dimensional mapping between the coordinate systems. For flow heights in-between those measured during the calibration process, the displacement is taken as the linear interpolation of the two maps at neighbouring heights.

If we define the map from pixel to world coordinates for a height h_i as $R(\boldsymbol{x}, h_i)$ then for a pixel displacement $\boldsymbol{d}(\boldsymbol{x})$ at a position $\boldsymbol{x}$ and height $h_i < h < h_{i+1}$ the real-world velocity is given by

$$\boldsymbol{u}(\boldsymbol{x}) = \frac{1}{\delta t(h_{i+1} - h_i)} \left[(h - h_i)\left(R(\boldsymbol{x} + \boldsymbol{d}(\boldsymbol{x}), h_i) - R(\boldsymbol{x}, h_i)\right) \right. \\ \left. + (h_{i+1} - h)\left(R(\boldsymbol{x} + \boldsymbol{d}(\boldsymbol{x}), h_{i+1}) - R(\boldsymbol{x}, h_{i+1})\right) \right]. \tag{3.12}$$

We perform this calculation for each of the 69×51 velocities to give a 2-D picture of the surface velocity.

3.4 Material Characterisation

As described in chapter 2, the $\mu(I)$ rheology is an extension of the basic Coulomb friction law with the coefficient varying with the inertial number I. Using the functional dependence in equation (2.20) introduced by Jop *et al.* (2006) reduces the characterisation of the coefficient to two constants μ_1 and μ_2 that are intrinsic to the material and are the minimum and maximum values of the coefficient for steady flows. There is also another constant I_0 that is not only dependent on the material but also on the flow geometry. We measure the friction coefficients μ_1 and μ_2 from measurements of $h_{\text{stop}}(\theta)$, the height of the deposit left by a steady flow at an inclination θ.

The lack of separation of scales in a granular fluid means that the particle diameter d plays a crucial role in many granular rheologies including the $\mu(I)$ rheology. We introduce a number of methods for evaluating the Particle Size Distribution (PSD) of a sample of our material, and take the median of the distribution as d. We also track the change in the PSD as the particles degrade over time.

The same granular material is used in all of our experiments: quartz silica sand that is a by-product of a coarse grade (14–18) sieving process. The initial specification of the washed sand is for diameters to lie in the range 0.71–1.2 mm. Typically the sand is rough and angular; there is no noticeable change in shape as the particles degrade and their size reduces.

3.4.1 Material Sizing

A number of techniques can be used to calculate the PSD of a granular material. Traditionally, sieving techniques are used. These have the advantage of being able to process large sample sizes easily, but the resolution of the PSD is low unless a large number of sieves are used and the sand vibrated vigorously. This can lead to breakage of the sand, thus making the method unfavourable. In any case, the original specification confines the particle diameter to lie within two standard sieving sizes and further sieving would give little further information. Instead, we discuss a number of more modern, optical techniques that offer a much more detailed profile of the particle diameter d. These techniques fall into two categories: binary image processing and segmentation techniques, and a fully optical laser-based technique capable of detecting a very wide range of particles.

The image segmentation techniques require a digital photograph of a sample that is at most one layer thick. When measuring the PSD we must ensure that enough particles are sized for the measurement to be statistically significant. Kennedy & Mazzullo (1991) show that 300 – 500 particles are needed for a statistically stable mean grain size value for natural sands.

A common problem with imaging a collection of grains is the apparent touching of the grain sections, preventing individual analysis. Although the number of contact points between grains of random orientations is small, the apparent touching of the grains is caused by the 'Holmes' effect first noted by Holmes (1930), whereby the projections of the particles in the thin layer overlap (Van den Berg *et al.*, 2002). It is therefore necessary to split the groups of particles into individuals, otherwise known as segmenting the image. Although this could be done manually, it quickly becomes unfeasible for a moderate number of grains, and so it is preferable for it to be done algorithmically.

Here we present two techniques that attempt to do this, the 'Shortest Chord method' and the Watershed transform. The first algorithm developed to tackle this turned out to be less efficient than later methods and so it was abandoned in favour of those presented here. The details are presented in appendix D.

The first step in obtaining particle size information using the image segmentation techniques is to acquire the images themselves. We place a sample of sand into a large petri dish on top of a diffuse light source. Having the light below the particles helps to increase contrast between the particles and the background. A Nikon SLR camera is used to take 6 megapixel images (2000×3008) in an uncompressed TIFF, (a lossless file format). The images contain around 500 – 700 particles, some of which are touching. We also take an image of the background illumination which is subtracted from the first image allowing for easy and accurate separation between the particles and the background.

Once the background illumination has been subtracted the image is thresholded, producing a binary image. An ‘on’ pixel represents the background, and an ‘off’ pixel indicates the presence of a particle. There is a small amount of speckle produced by dust and imperfections in the petri dish and dust. This is removed from the binary image by morphologically opening it. The user manually sets a threshold for this process, removing any objects smaller than the threshold. Figure 3.13 shows the raw image and the result of the thresholding and opening. Once we have a clean binary image, the segmentation can begin.

Shortest Chord Method

The shortest chord method is a conceptually simple yet computationally intensive method of segmentation. The first step in the process is calculating the positions of the centres of the grains. This is achieved by taking the Euclidean distance transform of the image (Borgefors, 1986). This transform calculates an approximation of the minimum distance of a foreground pixel (i.e. a pixel in a particle) to the background; the background pixels take a value of 0, and pixels within the particles have higher values the closer they are to a particle centre. The maxima of this transform give a close approximation to the particle centres (we use a process called ultimate erosion to calculate these maxima). However, since the particles used are not completely smooth, or indeed entirely convex, a number of maxima occur near the centre of each particle. Multiple maxima within a single particle are removed by creating a new binary image from the maxima pixels, morphologically closing the image by less than a particle diameter and taking the position of the centroid for each blob as the particle centre. This method of finding the particle centres detects all of the particles, apart from ones that have regions of high convexity (typically less than 20 in a sample size of more than 500) which report multiple centres.

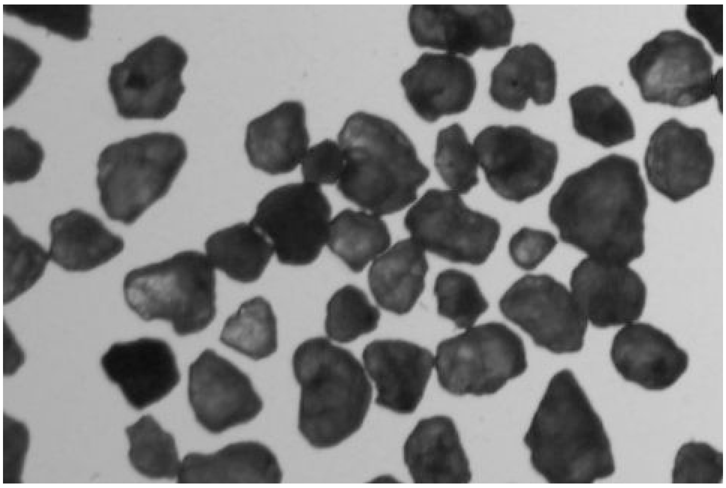

(a) Original Image

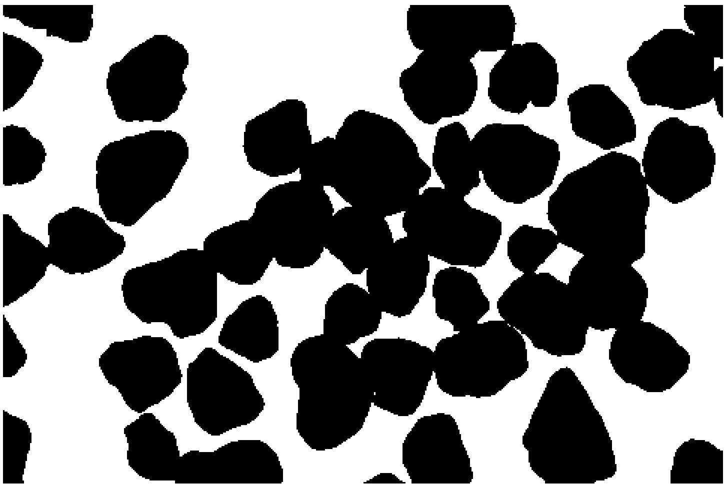

(b) Prepared Image

Figure 3.13: *Two images showing the preparation routine. The background is subtracted and the resultant image thresholded and morphologically opened to remove speckle.*

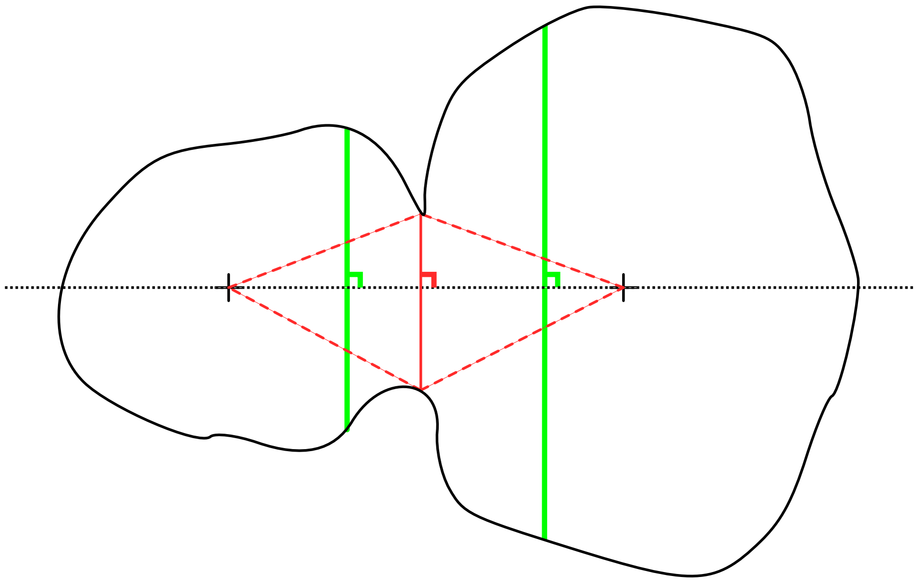

Figure 3.14: *Diagram showing a typical blob of particles, with the particle centres produced by an erosion process signified by crosses. The red line is the perpendicular bisector that minimises the distance between the two edges over all bisectors (b_d) of the line connecting the cores. Green lines are non-optimal cuts.*

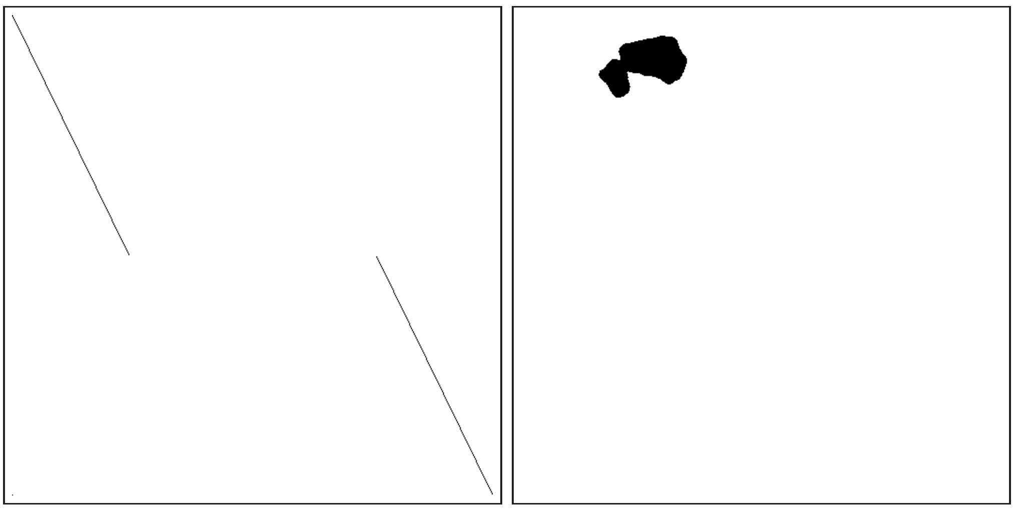

(a) Convolution Line

(b) Isolated Clump of particles

Figure 3.15: *The two images used in a convolution to find the shortest chord between two particles.*

Now that the number of particles is known, the mean particle size can be calculated by simply counting the number of foreground pixels in the original binary image. However, for more detailed information about the PSD, we use the particle centre information to separate the joined particles.

In order to do this, we label each region of the image. If a region is found with more than one particle centre then it must be split. The split point is chosen according to figure 3.14, by considering the bisectors of the line joining the particle centres. Of these bisectors, the one with the least 'on' pixels in the original image is chosen to be the line that splits the region into separate particles. This can be done by taking the pixel-wise logical intersection between the original binary image and a mask consisting of a line. More rigorously, if we define particle centres as $\boldsymbol{c}_1$ and $\boldsymbol{c}_2$, and the unit vector joining them $\hat{\boldsymbol{s}} = (\boldsymbol{c}_1 - \boldsymbol{c}_2) / |\boldsymbol{c}_1 - \boldsymbol{c}_2|$ then we define the bisector a distance d from $\boldsymbol{c}_1$ as

$$b_d = \{\boldsymbol{x} : (\boldsymbol{x} - \boldsymbol{c}_1) . \hat{\boldsymbol{s}} = d\} . \tag{3.13}$$

Then we choose the bisector, b_d that minimises

$$l(d) = \int_{x \in b_d} I(x) \, \mathrm{d}s, \tag{3.14}$$

for $0 < d < |\boldsymbol{c}_2 - \boldsymbol{c}_1|$ where I is the map of the grey levels in the image and s is the arc length along the path.

This method can also be formulated in terms of a convolution between the image and a mask. If we define an image K such that $K(\boldsymbol{x}) = 1$ for $\boldsymbol{x} \in b_0$ then the number of pixels l in the intersection between I and b_d is given by

$$l(d) = \sum_{\boldsymbol{x}} I(\boldsymbol{x}) K(\boldsymbol{x} + d\hat{\boldsymbol{s}}), \tag{3.15}$$

which is a region of the convolution of I and K. A sample image for I can be seen in figure 3.15(b), and the image K containing the bisector b_0 can be seen in figure 3.15(a). The convolution is then calculated using an FFT for computational efficiency.

The results of this algorithm are shown in figure 3.16 which shows the results of the segmentation of the image. The expected over-segmentation caused by

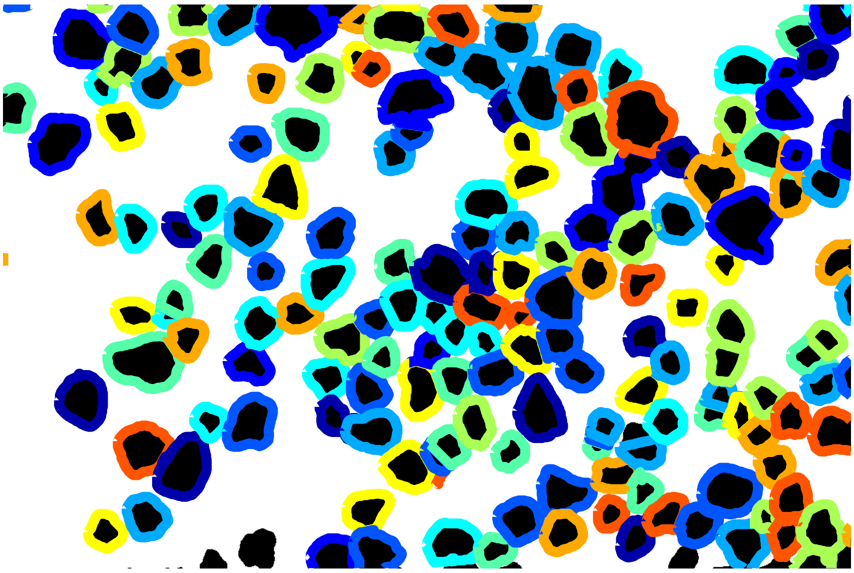

Figure 3.16: *Results of the shortest chord method.*

false-positive particle centres can be seen for very non-convex particles, although this affects fewer than 2% of the particles.

Watershed Transform

The watershed transform is a basic morphological tool for segmenting images. It relies on the fact that eroding the binary image will cause touching objects to separate before they disappear. The algorithm separates the image into so-called catchment basins, hence its name. The implementation of this algorithm (Russ, 2002; Meyer, 1994) again makes use of the euclidean distance transform E of the binary image I. The minima of E give an approximation of the grain centres. However, any non-convexity of the particles will mean multiple minima for each particle and over-segmentation. To avoid this, we morphologically reconstruct E to have minima only at the particle centres as we have previously calculated (in section 3.4.1).

The regions of each catchment basin are calculated by 'flooding' the image, taking the values of E as a height in a landscape. When the flooding is such that two basins are about to flow into each other, the pixels over which this happens are called a watershed line and are taken to be the edge of the particle.

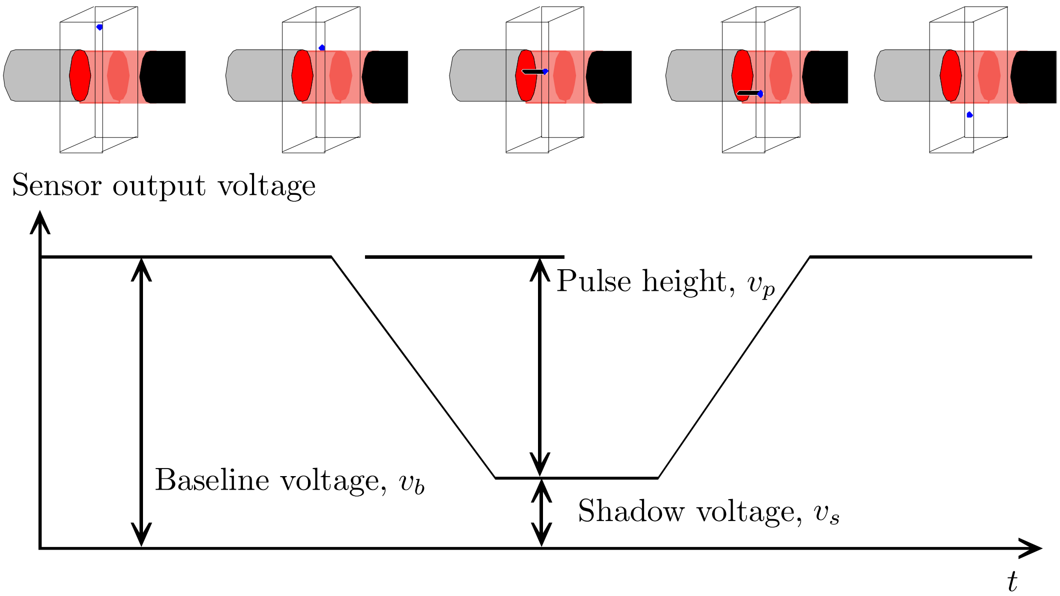

Figure 3.17: *Diagram showing the SPOS technique. The sensor voltage decreases from the baseline voltage v_b to the shadow voltage v_s as a particle passes through the beam. The decrease in voltage is directly related to the projected particle size. Reproduced from White (2003).*

Heuristically, this can be thought of as a ridge running between two valleys — water falling onto one side of the ridge flows into a separate river rather than a drop falling on the other side. The results for this algorithm were very similar to the shortest chord method on account of the algorithm detecting particle centres being identical.

Single Particle Optical Sizing Technique

The final method used for particle sizing utilises a commercially available laser light obscuration technique known as Single Particle Optical Sizing, or SPOS (White, 2003). SPOS is a very flexible technique that allows a large range of particle diameters to be sized. The equipment used here can size particles in the range $0.005\,\text{mm} < d < 5\,\text{mm}$.

As opposed to the previous two techniques which rely on image processing, SPOS uses a laser shone on a dedicated optical sensor. The particles fall under gravity through the laser beam. As they do this they produce a shadow on the detector, changing the output voltage. The change in voltage is directly related to the projected cross section of the particle; the precise relationship between the two is taken from a calibration curve which is produced by passing particles of known size through the equipment. A schematic of the equipment can be seen in figure 3.17.

In order to size a representative sample from the chute, around 100 g of sand is riffled into 10 test tubes. One of these samples is placed into the machine where it is vibrated such that the sand falls one grain at a time past the sensor. The vibration rate is controlled by the system with a feedback loop to ensure that occurrence of two particles passing simultaneously is kept to a minimum. Otherwise, the two particles are detected as a single, large particle. The particles and the air around them are sucked through the machine by a vacuum pump, consistently aligning the particle's longest axis with the flow.

The software provides histogram data of the particle diameters weighted either by number or by volume. In our samples, there were a large number of very small particles detected ($d < 0.01\,\mathrm{mm}$) that were negligible when weighting the PSD by volume. These fine, dust particles have been excluded from any further analysis as their contribution to the dynamics of the flow inside the chute should be negligible.

Due to the ease of use, robustness and repeatability of this procedure, all particle sizing data presented here uses this technique.

Discussion and Results

For any particle (apart from perfect spheres), its 'diameter' as a single value is ill-defined. We can only hope to give a characteristic measurement of the size which is repeatable and reliable, thus allowing the effect of particle size on our data to be accounted for when comparison are drawn with other particle species in third parties' observations. However, the need for consistency between data sets requires a knowledge of how the characteristic sizes given by various techniques differ.

For any particle, we can define three lengths by placing the particle fully within a cuboid of minimal volume. We define the lengths of this cuboid as d_1, d_2 and d_3 where $d_1 \leq d_2 \leq d_3$ and lie in the directions $\boldsymbol{e}_1$, $\boldsymbol{e}_2$ and $\boldsymbol{e}_3$.

The particle diameter on which sieving is based can be deduced by considering the smallest cross section perpendicular to d_1. This cross section perpendicular to $\boldsymbol{e}_1$ will have a bounding rectangle of sides d_2 and d_3. Since the shape of the aperture through which the particle must pass is, to a good approximation, a square of side length d_{sieve}, we have that all particles with $d_2 < d_{\text{sieve}}$ will pass through.

However, we also note that for particles where $d_2 \neq d_3$, slightly larger particles can pass through if oriented diagonally to the sieve. Taking the plane normal to $\boldsymbol{e}_1$ and considering the bounding rectangle suggest that particles for which $d_2 < \sqrt{2}d_{\text{sieve}} - d_3$ will pass through, with the result that if $d_3 \to 0$ then particles for which $d_2 < \sqrt{2}d_{\text{sieve}}$ will also pass. This means that the particle diameter recorded by the sieving process will give a result

$$\frac{d_2 + d_3}{\sqrt{2}} \lesssim d_{\text{sieve}} < d_2 \tag{3.16}$$

which, notably, is wholly independent of the largest dimension d_1.

The two image-processing techniques record a slightly different particle diameter to sieving. It is supposed that the particle lies with its longest axis parallel to the horizontal so that the image seen by the camera is the projected area containing the $\boldsymbol{e}_1$ axis. We can equate the projected area A to an equivalent circular size by

$$d = \sqrt{\frac{4A}{\pi}}. \tag{3.17}$$

Assuming that the particles are approximately ellipsoidal, i.e. $4\pi d_1 d_3 < A < 4\pi d_1 d_2$, we can bound the diameter recorded by these image processing techniques d_{ip} as

$$\sqrt{d_1 d_3} < d_{\text{ip}} < \sqrt{d_1 d_2}. \tag{3.18}$$

The high speed laminar flow created by the vacuum in the SPOS machine sucks the particles past the optical sensor, causing the particles' longest axis to align with the flow i.e. d_1 is parallel to the vertical axis. This means that the area projected onto the sensor is the same as would be observed using the image

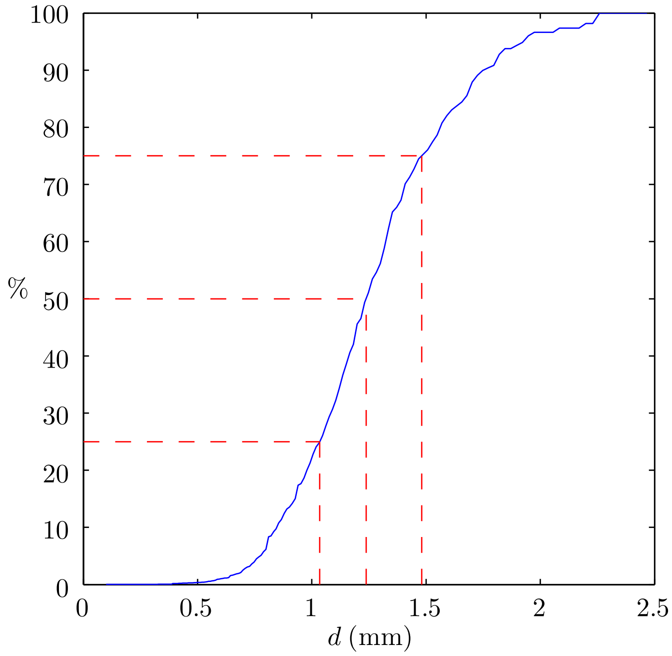

Figure 3.18: *The cumulative distribution function of the particle size weighted by volume. The SPOS sizing method has been used here, and gives a median particle diameter of 1.24* mm*. The first and third quartiles are 1.03* mm *and 1.48* mm *respectively.*

processing techniques. As a result,

$$\sqrt{d_1 d_3} < d_{\mathrm{SPOS}} < \sqrt{d_1 d_2}, \tag{3.19}$$

where we have used the same ellipsoidal approximation to convert the projected area into an equivalent diameter. This reasoning indicates that the SPOS and image processing techniques should give the same PSD. The discrepancy in the characteristic size between sieving and the other techniques equates to a difference of 20–30% for natural sands (White, 2003).

The PSD for the new sand before it has be recirculated around the machine is shown in figure 3.18. The sand is initially graded by the suppliers using the sieving technique, which gives a particle diameter range of 0.7 mm to 1.2 mm. Given the sieved size, and using the aforementioned discrepancy of White (2003), we would expect the size given by SPOS to be around 0.91 mm and 1.5 mm. These figures agree very closely with the quartile measurements presented in the figure.

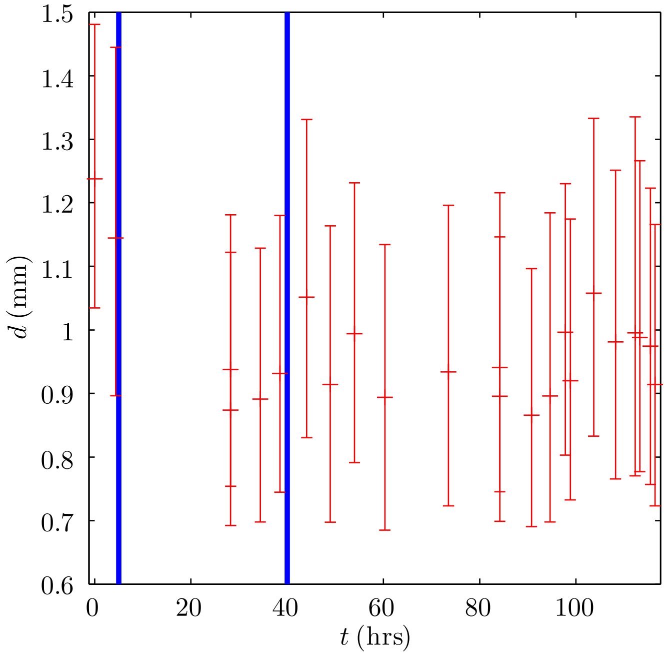

Figure 3.19: *The evolution of the particle diameter over time. Median diameter shown with error bars signifying the upper and lower quartiles. Blue lines signify times at which new sand was added.*

The development of the PSD as the sand is circulated over time is shown in figure 3.19. It shows that the initial particle size decays quickly to around 1 mm through particle-particle wear as well as wear caused by the recirculation mechanism. The rapidity of the decay is due to the particles breaking along any existing weaknesses in the particles. As these weak lines disappear, the particles become more robust and the rate of decay reduces. The blue lines indicate times where a substantial amount of new sand was added ($\sim 5\%$ of the total amount by mass). The PSD remains reasonably steady, with the small variations an artefact of the strong segregation effects seen in the chute. As segregation effects are very sensitive to the strength of the shear in the flow, the sample is sensitive to the flow history.

Subsequent chapters use the figure $d = 1\,\mathrm{mm}$ in all calculations. The density of the quartz that grains consist of is $\rho = 2660\,\mathrm{kg\,m^{-3}}$.

3.4.2 Frictional limits of equilibrium flows

The dynamics of a dense granular flow are heavily dependent on the frictional contribution to the rheology. The $\mu(I)$ rheology combines the effects of other mechanisms such as force chains and particle collisions into an effective friction coefficient. In order to compare the experimental results with such a friction-based rheology, it is necessary to measure the material's natural resistance to shearing. We can calculate the friction coefficient of a steady inclined flow, as in such a flow the retardation by friction is equal to the gravitational body force, giving

$$\mu g \cos\theta = g \sin\theta \quad \Longrightarrow \quad \theta = \tan^{-1}\mu. \tag{3.20}$$

We can exploit this relationship to measure μ by setting up a flow and slowly decreasing the inclination until the flow stops. We call this inclination θ_{stop}. An important result due to Pouliquen & Forterre (2002) as discussed previously shows that this angle is a function of only the particle species, basal condition and the height of the flowing layer, i.e. $\theta_{\mathrm{stop}}(h)$ for a given experiment. We can exploit this result to define the inverse of this function $h_{\mathrm{stop}}(\theta)$, which is the height of the stationary deposit left after a flow on an inclination θ.

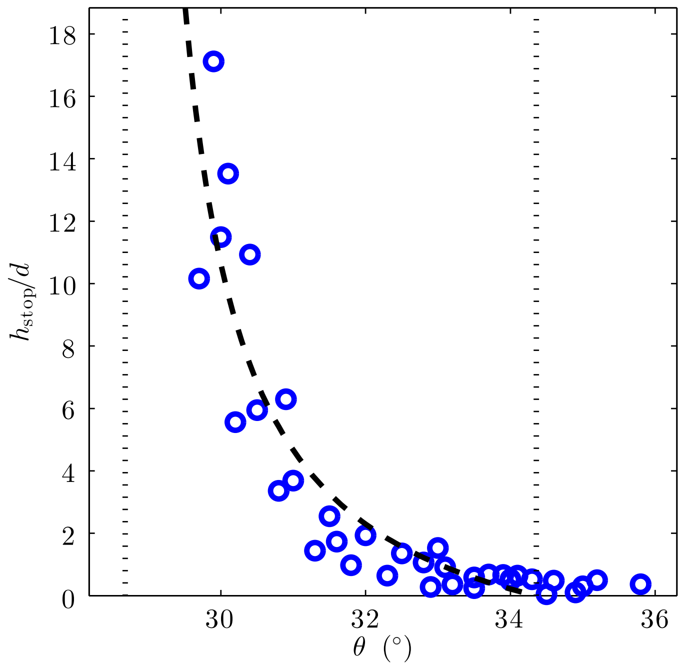

Figure 3.20: *The deposit height h_{stop} as a function of the inclination over the rough base. Fitting the curve described by* (3.21) *gives $\mu_1 = 0.54$, $\mu_2 = 0.68$ and $B = 3.0$.*

We measure the h_{stop} function by setting up flows on a range of angles in increments of 0.1° on a wide chute. Once the flow has reached a steady state we suddenly stop the mass entering the chute and allow the flow to come to a complete stop. We then scan the deposit using the laser triangulator and look for regions of constant height.

The h_{stop} curve is well fitted by the form introduced in MiDi (2004):

$$\frac{h_{\mathrm{stop}}(\theta)}{d} = B\frac{\mu_2 - \tan(\theta)}{\tan(\theta) - \mu_1}. \tag{3.21}$$

for some constant of proportionality B, and two constants μ_1 and μ_2. We have discussed this form for h_{stop} more fully in chapter 2.

The h_{stop} curve over the rough base for our material is shown in figure 3.20. Fitting equation (3.21) to the data gives $\mu_1 = \tan(28.7°) = 0.54$ and $\mu_2 = \tan(34.3°) = 0.68$. The parameter $B = 3.0$, although this is not important for our subsequent analysis but is included for completeness.

The characterisation with two friction coefficients is useful on a rough basal surface. On the smooth perspex there was no measurable range of angles with $\mu_1 = \mu_2 = \tan(24.4 \pm 0.2°) = 0.45$.

4

Experimental Results

4.1 Introduction

In this chapter we present results of experiments performed on slopes with $\theta > \theta_2$, the methodology of which was introduced in chapter 3. Our measurement systems used to collect the data are limited to surface measurements and therefore we analyse the data by integrating the equations of motion over the chute cross section. The result is similar in form to the shallow water equations in 1D, but there are additional terms for the stresses at the wall. To this end, we briefly review one of the most frequently used models in the field of granular flows and its variations.

A Coulomb friction law is supposed for the stress tensor so that we may directly compare our results to the $\mu(I)$ rheology discussed in chapter 2. We consider a generalisation of the $\mu(I)$ rheology by allowing other functional forms for the dependence of μ on Fr and $n = h/d$. Even with this generalisation, we find poor agreement with the experiments and discuss the possible reasons for this.

4.2 Theoretical Framework

We assume that the following equations of motion are valid for some stress tensor $\boldsymbol{\sigma}$ and take a Cartesian coordinate system as in the previous chapters, with x aligned with and increasing in the downslope direction, z perpendicular to the base with $z = 0$ at the base and $z = h$ at the free surface and lastly y lies across the chute to complete a right-handed xyz triad. The origin is then at the top of the chute on the basal surface.

We integrate over an area A that occupies the whole width of the chute in the y direction, and all of the space above the basal surface in the z direction. This is then specified by the limits $0 < y < W$ and $0 < z < \infty$. The conservation of mass is given by

$$\frac{\partial \rho}{\partial t} + \boldsymbol{\nabla} \cdot (\rho \boldsymbol{u}) = 0 \tag{4.1}$$

and the conservation of momentum by

$$\frac{\partial \rho \boldsymbol{u}}{\partial t} + \boldsymbol{\nabla} \cdot (\rho \boldsymbol{u}\boldsymbol{u}) = \rho \boldsymbol{g} + \boldsymbol{\nabla} \cdot \boldsymbol{\sigma}, \tag{4.2}$$

where $\boldsymbol{u}\boldsymbol{u}$ denotes the dyadic product of $\boldsymbol{u}$ with itself.

The mass holdup in a slice is

$$\rho_p h W \phi = \int \rho \, \mathrm{d}A, \tag{4.3}$$

hence we denote the average of velocity quanties u_i^n as

$$\widehat{u_i^n} = \frac{1}{hW\phi\rho_p} \int_A \rho u_i^n \, \mathrm{d}A. \tag{4.4}$$

Previous studies (e.g. Louge & Keast, 2001) have used non-invasive experimental measurement techniques to show that ϕ is approximately constant. This is in agreement with DEM simulations (Silbert *et al.*, 2001), with the approximation improving for thicker flows. A fuller discussion of this assumption can be found in chapter 2. We therefore assume incompressibility and take $\phi = \text{const}$.

As W is also constant, we can write the integrated conservation of mass as

$$\frac{\partial h}{\partial t} + \frac{\partial}{\partial x}(h\widehat{u}) = 0, \tag{4.5}$$

as there is no mass flux through the basal surface or the top surface (assuming the thickness of the saltating layer remains near constant down the slope). The limits of the integral in the definition of $\widehat{(\cdot)}$ do not depend on the coordinates, so the averaging process commutes with derivatives. Defining the average of a stress quantity σ_{ij} as

$$\widehat{\sigma}_{ij} = \frac{1}{hW\phi\rho_p}\int_A \sigma_{ij}\,\mathrm{d}A, \tag{4.6}$$

the conservation of momentum in the slice is given by

$$\begin{aligned}
\frac{\partial h\widehat{u}}{\partial t} + \frac{\partial h\widehat{u^2}}{\partial x} &= \; hg\sin\theta + \frac{\partial h\widehat{\sigma_{xx}}}{\partial x} - 2\frac{h}{W}\psi_x - \tau_x, && (4.7)\\
\frac{\partial h\widehat{v}}{\partial t} + \frac{\partial h\widehat{uv}}{\partial x} &= \; \frac{\partial h\widehat{\sigma_{yx}}}{\partial x} - 2\frac{h}{W}\psi_y - \tau_y, && (4.8)\\
\frac{\partial h\widehat{w}}{\partial t} + \frac{\partial h\widehat{uw}}{\partial x} &= -\,hg\cos\theta + \frac{\partial h\widehat{\sigma_{zx}}}{\partial x} - 2\frac{h}{W}\psi_z - \tau_z. && (4.9)
\end{aligned}$$

We have used $v = 0$ at the walls, and introduced the basal shear stress

$$\tau_i = \frac{1}{\phi\rho_p}\left[\frac{1}{W}\int_0^W \sigma_{iz}|_{z=0}\,\mathrm{d}y\right] \tag{4.10}$$

and the stress at the walls

$$\psi_i = \frac{1}{\phi\rho_p}\left[\frac{1}{h}\int_0^h \sigma_{iy}|_{y=0}\,\mathrm{d}z\right], \tag{4.11}$$

both expressed in terms of the average stress at the appropriate boundary. We have exploited the symmetry of the flow to write the total stress on the slice of fluid due to the shearing at the walls as twice the contribution from one wall. If we take the wall stress $\boldsymbol{\psi}$ and the transverse velocity v to be zero, and use the appropriate form for the stress tensor $\boldsymbol{\sigma}$, we recover the shallow water or Saint-Venant equations (de Saint-Venant, 1871).

4.2.1 Savage-Hutter Model

One of the first motivations for deriving an integrated approach to modelling granular flows was to predict avalanche run-out. An early attempt at modelling avalanches using a continuum mechanical theory was made by Savage & Hutter (1989). Their model has since become popular and is widely used on account of its simplicity, while still retaining a physical foundation. In its various guises it has been used to predict the shape, run-out and velocity of avalanches in many studies e.g. Denlinger & Iverson (2004); Gray *et al.* (1999); Greve & Hutter (1993); Hutter *et al.* (1993), to name but a few.

The original theory was very simple yet gave good agreement with laboratory experiments. It relied on a simple force balance between the gravitational forcing, basal resistance and the pressure gradient along the slope. It also exploited the property of avalanches that the majority of shear happens in a narrow layer at the base, and used this to simplify the velocity profile to a plug flow with slip at the base. If the material obeys a Coulomb law then the plug flow hypothesis holds if the internal angle of friction is larger than the angle of the frictional basal stress. The model can also easily incorporate other forms of basal drag.

The vertical inertia in the Savage-Hutter model is also neglected as it is assumed that the avalanche is much longer than it is high. This is also known as the long-wave approximation, and gives a simple hydrostatic balance for the pressure.

We can estimate the size of the neglected inertia by scaling x with a typical length scale L and z with the height h. Since the flow is assumed to be a plug flow, mass conservation implies that

$$w = -\frac{\partial u}{\partial x} z. \tag{4.12}$$

Therefore, if the vertical momentum in equation (4.9) scales as $h^2 u u'/L$, then it is small in comparison to the basal pressure $hg\cos\theta$ if

$$\epsilon = \frac{h}{L} \ll \mathrm{Fr}^{-1}. \tag{4.13}$$

The vertical inertia which is $O(\epsilon p)$ can thus be safely neglected, and the unidirectional assumption is valid.

The hydrostatic pressure balance is then used for the Coulomb basal traction, and is given by

$$\tau = -p \tan\varphi \,\mathrm{sign}(u), \tag{4.14}$$

where δ is defined as the basal friction angle.

The original Savage-Hutter model does however introduce a significant complication over the standard Saint-Venant equations by introducing the highly non-linear earth pressure coefficient. This addition is motivated by the classic soil mechanics problem of calculating the loads exerted on a retaining wall (Rankine, 1857), and is caused by the difference in the strength of soil under extensive and compressive modes of deformation. This gives the lateral pressure p_L as a function K multiplied by the lithostatic pressure:

$$p_L = K\left(\frac{\partial u}{\partial x}\right)p, \tag{4.15}$$

with K taken as a piecewise constant function

$$K = \begin{cases} K_{\mathrm{act}} & \text{if } \dfrac{\partial u}{\partial x} > 0. \\ \\ K_{\mathrm{pass}} & \text{if } \dfrac{\partial u}{\partial x} < 0. \end{cases} \tag{4.16}$$

where the active mode corresponds to the compressive deformation and the passive mode to extensive deformation. More recently however, experimental evidence (Gray *et al.*, 1999; Ertaş *et al.*, 2001) suggests that this sharp stress transition does not exist. Indeed, the depth averaged equations give good agreement on slopes and in rotating drum flows without adding this complication. We therefore choose to take $K = 1$ and return to an isotropic pressure. This basic approach to avalanche modelling has been extended in many ways by adding various complicating effects. Indeed, the account given above is a simplification of the model presented in the initial paper, which includes lateral effects and a slowly changing curvature of the basal surface. Other effects such as more strongly curved basal topography (Savage & Hutter, 1991), erosion and deposition effects (Gray, 2001) and many others have been included over the years. Indeed, the integrated approach which we will use to analyse our experimental results can be thought of as an extension to the Savage-Hutter theory.

4.2.2 Application to chute flow

In order to discuss our experimental results effectively, we must add a few analytic devices to the $\mu(I)$ theory already explained in chapter 2.

The depth-integrated equations of motion in section 4.2 provide a means of defining a macroscopic friction coefficient, or total friction, μ_t, which measures the overall retardation of a slice of granular fluid due to the resistive forces exerted on the material by the boundaries. This stress is then transmitted through the material according to its rheology. As our flows are time-steady we can set $\partial_t = 0$.

We write the x-velocity u as the maximum surface velocity u_s multiplied by a dimensionless function, to give the y and z dependence:

$$u = u_\mathrm{s}\, f\left(\frac{y}{W}, \frac{z}{h}\right). \tag{4.17}$$

In this representation, f takes a value of 1 at a point on the surface. Since the flows are assumed to be symmetric and the walls exert resistive forces, we expect this to occur in the middle and therefore $f(1/2, 1) = 1$ with $f < 1$ at the walls. A flow with a no-slip basal condition equates to $f(y/W, 0) = 0$, a flow with Bagnold depth dependence has $f \sim z^{3/2}$, and a plug flow has $f(y/W, z/h) = 1$.

We define s_n as the average value of f^n, i.e.

$$s_n = \frac{1}{Wh} \int \int f^n \,\mathrm{d}y\,\mathrm{d}z, \tag{4.18}$$

meaning we can write

$$\widehat{u} = u_s s_1. \tag{4.19}$$

Assuming $f(y, z)$ is positive everywhere (i.e. no return flow), we have $0 < s_n < 1$. The values of the s_n for typical flows are $s_1 = s_2 = 1$ for a plug flow, $s_1 = \frac{1}{2}, s_2 = \frac{1}{3}$ for linear shear, and $s_1 = \frac{3}{5}, s_2 = \frac{9}{20}$ for a Bagnold profile. In this formulation we define the mass flux

$$q = \int_V \rho u \,\mathrm{d}V = \phi\rho_p\widehat{u}Wh, \tag{4.20}$$

where we have used the relation

$$\rho = \phi \rho_p, \tag{4.21}$$

and which, when used in the conservation of mass in equation (4.5), gives

$$q = \text{const.} \tag{4.22}$$

down the slope, as is to be expected. At this point we make an assumption about the form of the stress tensor. For a hydrodynamic formulation such as the one discussed here, we must include a pressure which is taken as isotropic for the reasons described above (i.e. the earth pressure coefficient $K = 1$ at all times). We also include a deviatoric component of the stress tensor τ, such that

$$\sigma_{ij} = -p\delta_{ij} + \tau_{ij}. \tag{4.23}$$

Using a similar analysis to chapter 2 and section 4.2.1, we also exploit the aspect ratio of the flow to neglect vertical inertia. Using the scalings

$$\begin{aligned} x &\sim L, \\ z &\sim h, \\ u &\sim \sqrt{gL}, \end{aligned}$$

we define the aspect ratio

$$\epsilon = \frac{h}{L} \tag{4.24}$$

we find that the inertial term has size

$$\frac{\partial h\phi\widehat{uw}}{\partial x} \sim \epsilon^2 \phi g L \ll \epsilon \phi g L \sim \phi h g \cos\theta, \tag{4.25}$$

where we have used incompressibility to scale $w \sim \epsilon u$, and therefore the term can be neglected if $\epsilon \ll 1$.

If we assume that the deviatoric stress $\tau_{ij} \propto \dot{\gamma}_{ij}$ (as in the $\mu(I)$ rheology) then since $|\partial_z u|$ and $|\partial_y u|$ are much larger than all the other gradients of the velocity in the interior of the flow, we can include just the terms τ_{xz} and τ_{xy} in our analysis.

We assume that the chute is wide enough so that the friction at the wall makes negligible difference to the vertical momentum balance of the slice. We also take the momentum flux into the dense part of the flow, caused by any saltating particles at the surface $z = h(x)$, to be small. Making these assumptions, we recover a hydrostatic pressure balance by partially depth-integrating the equations. This gives

$$p(x, z) = \rho_p \phi g \cos\theta (h(x) - z). \tag{4.26}$$

We assume that the mass contained within this dense core is much larger than in the saltating layer, and so the saltating layer has a negligible influence on the dynamics. Because of this, we may take $p(x, h(x)) = 0$ and the surface at $z = h$ to be stress-free. Integrating this we obtain

$$\widehat{p} = \frac{1}{2}\rho_p \phi h g \cos\theta. \tag{4.27}$$

Up until this point, the flow height has only appeared as part of the combination $h\phi$, the integrated mass, but in the expression above, h appears independently through the dependence on the centre of mass of the flow. We therefore need to introduce an equation of state for ϕ. As we have assumed incompressibility we use $\phi = \text{const}$. In most of our experiments the measured height was well defined as the flows had a sharp interface. However, for the very fast flows, a small saltating region appeared at the surface. Taking a median value of the height profile removes most of the saltating grains from the data, and our effective h records the height of the surface of the dense region in the middle of the flow.

Using these simplifications in the x momentum evolution (equation (4.7)) we obtain

$$\frac{s_2}{s_1^2}\frac{\partial\left(h\widehat{u}^2\right)}{\partial x} + \frac{\partial}{\partial x}\left(\frac{1}{2}g\cos\theta h^2\right) = gh\sin\theta - hF. \tag{4.28}$$

Here, we define the retarding force on the slice of material per unit area$\times$ density as F. In terms of the basal and wall tractions we have

$$F = 2\frac{h}{W}\psi_x + \tau_x. \tag{4.29}$$

Rewriting this in terms of the surface velocity u_s , we obtain the evolution equation

$$\left(s_2 - \frac{s_1^2}{\mathrm{Fr}^2}\right) u_\mathrm{s} \frac{\mathrm{d}u_\mathrm{s}}{\mathrm{d}x} = g \sin\theta - F. \tag{4.30}$$

By drawing an analogy between the resistive force F and a Coulomb friction law (as in chapter 2), we can define a *total friction* coefficient μ_t as

$$\mu_t = \frac{F}{g\cos\theta}. \tag{4.31}$$

In steady, fully-developed flows the acceleration is by definition 0, and $\mu_t = \tan\theta$. The factor $s_2 - s_1^2\mathrm{Fr}^{-2}$ multiplying the advective acceleration in equation (4.30) gives some indication of the range of validity of the assumption of time-steady flow. For $\mathrm{Fr} > s_1 s_2^{-1/2}$, the downslope coordinate x behaves as a modified time coordinate and the flows are super-critical, with the upstream conditions left unaffected by downstream conditions. When $\mathrm{Fr} < s_1 s_2^{-1/2}$, the flow is sub-critical and it is determined by the downstream conditions. In both cases, the existence of a time-steady state, and hence the validity of equation (4.30), will depend on the boundary conditions. However, we note that for small changes of the height as in our experiments, the term proportional to Fr^{-2} is small and can be neglected.

One more definition needed to explain our results is the average, or bulk inertial number I_b. We can use typical values for the local shear rate $|\dot{\gamma}| = u_\mathrm{s}/h$ and the basal pressure $P = \rho g h \cos\theta$ to define the bulk inertial parameter as

$$I_b = \frac{u_\mathrm{s} d}{\sqrt{g h^3 \cos\theta}} = \frac{\mathrm{Fr}}{s_1 n}. \tag{4.32}$$

In our experiments I_b, is in the range $0.1 < I_b < 2.7$, throughout which the flow remains in the dense regime. The upper limit of this range is much larger than in previous studies, which have typically focused on the range $I_b < 0.5$ (MiDi, 2004; Forterre & Pouliquen, 2008).

Data Preparation

In order to study the acceleration of the flow it is necessary to calculate the derivative of the velocity data. Doing this directly amplifies noise, so the data is first fitted with the form in equation (4.33). Median averaging of the surface velocity was chosen in order to neglect the effect of outliers. The functional form used for the fit is

$$u_s^2 = u_0^2 + \frac{\delta}{\gamma}\left(1 - e^{-\gamma x}\right), \tag{4.33}$$

for some constants u_0, δ and γ. This form can represent convergence to a constant velocity state for large γx as $u_s^2 = u_0^2 + \frac{\delta}{\gamma}$. For positive γ, this velocity is what would be attained in an infinitely long chute, barring any phase transition. Constant acceleration (or deceleration) is also captured for small γx since $u_s^2 = u_0^2 + \delta x + O\left((\gamma x)^2\right)$. This fitted all of the data for appropriate choices of u_0, δ and γ. Many other choices would doubtless also have worked without affecting the results. Using this fit, the total friction μ_t is given by

$$\mu_t = \tan\theta - \frac{\delta}{2g\cos\theta} e^{-\gamma x}\left(s_2 - \frac{s_1^2}{\mathrm{Fr}^2}\right), \tag{4.34}$$

where s_1 and s_2 are assumed to take values given by a Bagnold profile for the rough base and a plug flow for the smooth base. The height data was also fitted using a similar functional form that replaces u^2 with h. The results of the fit for h and u_s can be seen as solid lines in figures 4.5(a) – 4.5(d).

4.3 Results

Data were collected for inclinations $30^\circ \leq \theta \leq 55^\circ$ with intervals of around 2° and for fluxes $2\,\mathrm{kg\,s^{-1}} \leq q \leq 20\,\mathrm{kg\,s^{-1}}$ with intervals of around $2\,\mathrm{kg\,s^{-1}}$. The total number of experiments for each base is approximately 120 and each experiment consists of measurements taken at 10 positions down the chute. A total of just under 2400 sets of measurements were taken in total.

We observed a number of different flow regimes besides the fully dense regime that we were expecting. The phase diagrams in figure 4.1 show the character of the flows as the inclination θ and the mass flux q change. The mass flux has been non-dimensionalised using the scaling $\rho_p w d\sqrt{gd}$.

Figure 4.1(a) shows that over the smooth base two regimes were observed. At a fixed inclination and for a sufficiently high mass flux the flows were dense and accelerating, however for slightly lower mass fluxes an instability occurred whereby

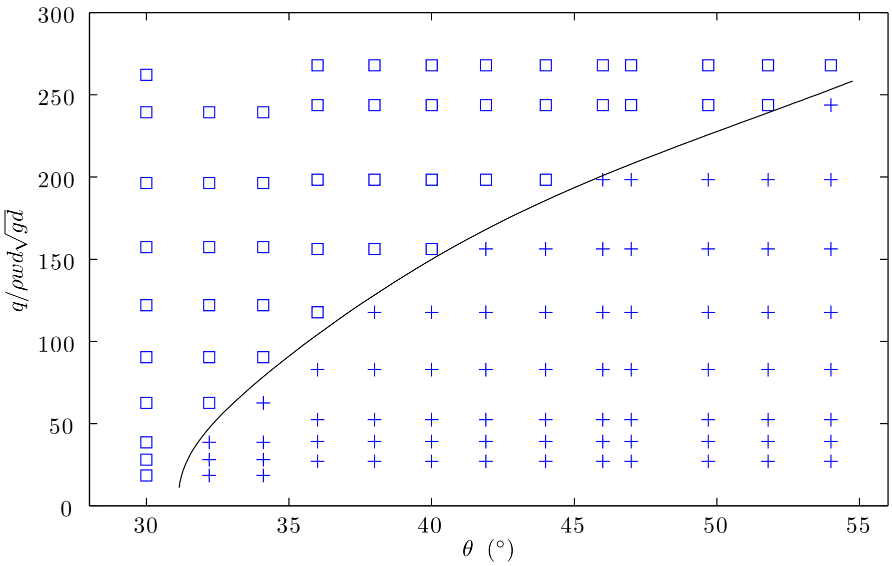

(a) Smooth Base

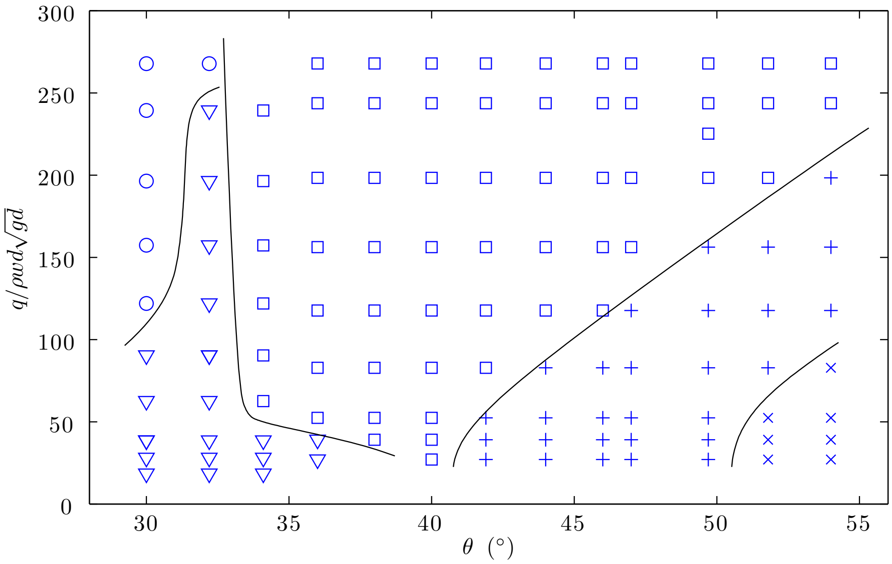

(b) Rough Base

Figure 4.1: *Phase diagram for flows over rough and smooth bases. Each base has around 130 experiments performed, with each experiment consisting of 12 sets of measurements. ($\bigtriangledown$) Constant velocity flows, ($\square$) Accelerating, Dense Flows, ($+$) Flows with separation at walls, ($\times$) Low density flows, ($\circ$) Superstable heap formation (see text for details.)*

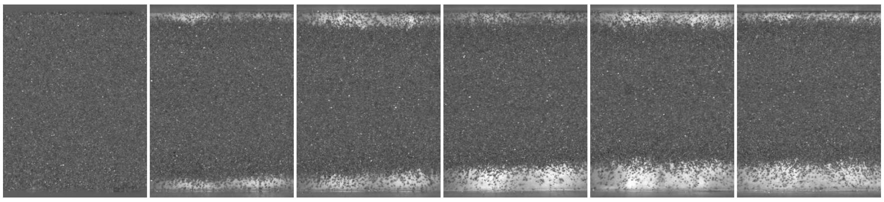

Figure 4.2: *Lateral inelastic collapse. Adjacent panels are separated by 0.25* m. *Increasing x from left to right.*

the flow detached from the walls in a type of transverse inelastic collapse (pictured in figure 4.2). This will be discussed further in section 4.4.1. The majority of flows on the rough base also fell into one of these two regimes. The rough surface also produced a number of regimes not seen on the smooth base (figure 4.1(b)). For flows over the lowest inclinations, the velocity was constant down the slope. At these low inclinations sufficiently high mass fluxes produced a superstable heap at the base (Taberlet *et al.*, 2003) and the chute quickly overflowed. Superstable heaps are stationary or creeping regions that form at the base of the chute for inclinations $\theta > \theta_2$ and are stabilised by the flow on top of them. When the mass source is cut off these regions start to flow and eventually the chute empties.

No constant velocity flows were observed for the smooth base, as the friction angle on the smooth base was lower than the lowest inclination investigated.

For the highest inclinations and for low mass fluxes, a low-density regime was observed whereby the entire flow became agitated. These flows did not have a well-defined surface and so PIV and height data were not available. The flows discussed here, unless otherwise specified, lie in the dense, accelerating regime. We did not notice any bistable regions of the parameter space though we did not look for these in detail.

4.3.1 Dense Flow

The flows over smooth bases showed higher average surface velocities than over rough bases, which is to be expected since a smooth surface gives less resistance. The typical surface velocity profile development for each base can be seen in figure 4.3. Each line represents a time-averaged velocity profile at a given point on the slope. For both flows depicted, it can be seen that the material is accelerating

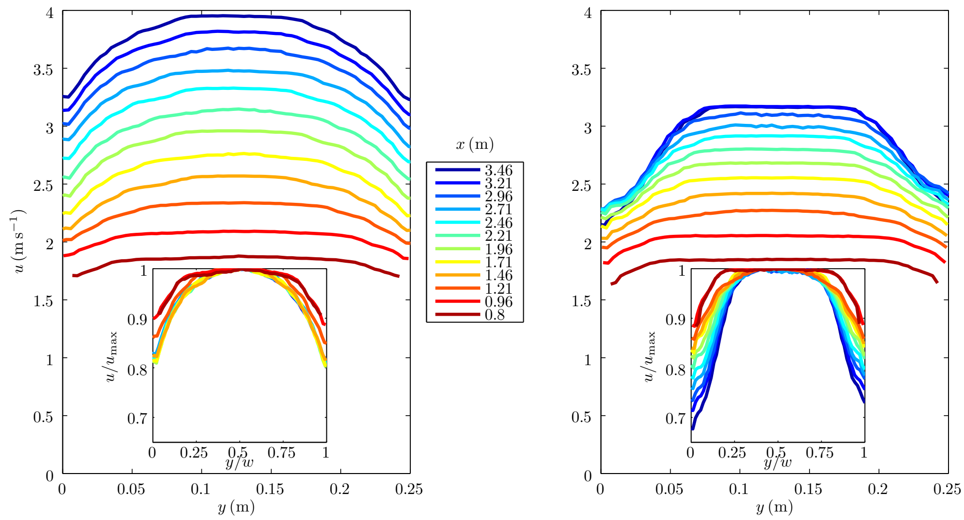

(a) Smooth Base (b) Rough Base

Figure 4.3: *Evolution of the time-averaged transverse velocity profile as the material accelerates down the slope. The flow parameters are* $\theta = 40°$ *and* $q = 19.1\,\mathrm{kg\,s^{-1}}$. *Inset shows* $u/u_{\max}$ *against* y/w.

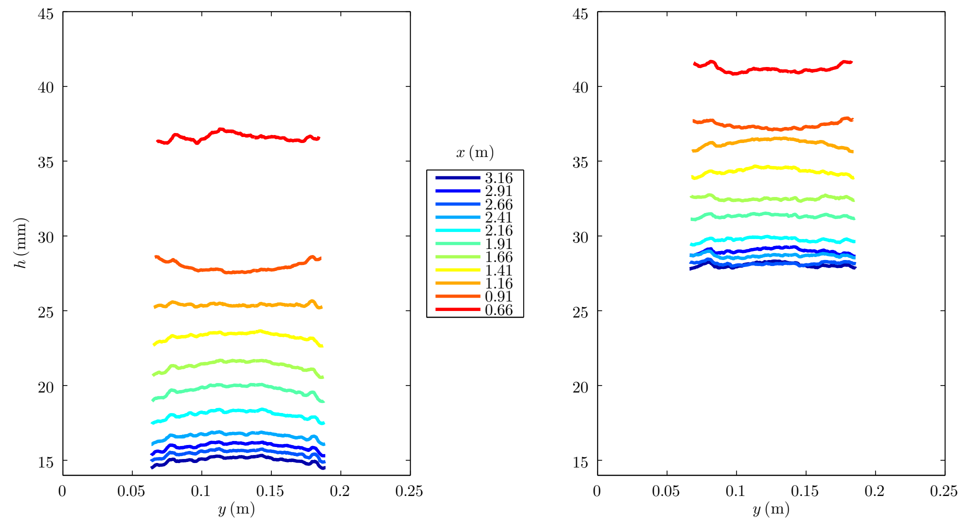

(a) Smooth Base (b) Rough Base

Figure 4.4: *Evolution of the time-averaged transverse height profile as the material accelerates down the slope. The flow parameters are* $\theta = 40°$ *and* $q = 19.1\,\mathrm{kg\,s^{-1}}$. *No height data was available at the edges.*

as it progresses down the slope.

A striking result was the effect of the basal surface on the shape of the velocity profile at the free surface. Figure 4.3 shows flows with the same control parameters (q, θ) exhibiting qualitatively different surface profiles. Flows over the smooth bases invariably had a profile with a gradual and continuous change in velocity gradient across the chute, whereas the flows over the rough base developed a region in the centre of the chute with no lateral variation. This region is flanked by two shear zones, one near each wall, with the velocity varying linearly with distance from the boundary. This type of behaviour is usually found in confined flows; in a vertical chute, the stress in the centre of the flow is less than the yield stress and so a plug region forms with a shear band at the wall of fixed width, typically of size $5 - 10d$. Flows over both basal surfaces exhibit a non-constant acceleration.

The insets of figure 4.3 show each velocity profile normalised by its peak velocity. In the smooth case, the effect of the shape of the initial condition is transient over a distance of around 1.5 m after release. After this point, the shape of the profile remains steady in time, implying the y dependence of f is constant. In the rough case however, the slip velocity at the wall tends to a limit, while the central, plug-flow region carries on accelerating. This implies a non-self-similar shape and therefore the s_n change as the flow develops.

Figure 4.4 shows the height evolution for the same flows as figure 4.3. The variation of the height across the slope is minimal, typically less than $2d$. Height data for the edges of the flow were not systematically available due to the limited width of the laser sheet, however, the edges were checked periodically and showed no significant deviation in height from the centre. As the flow accelerates down the slope, conservation of mass causes the height to decrease. The surface velocities over a rough base are typically lower and, by this principle, the flow is deeper for the same q over the smooth base.

Flows for which $\theta < \theta_2$ showed no acceleration along the chute, maintaining constant velocity and height throughout. No non-accelerating flows were observed for flows over the smooth base, as the $\theta_{1,2}$ were outside of the investigated range.

For the accelerating flows, although the cross-slope velocity profiles are qualitatively different between the bases, there is no qualitative difference in the development of u_s down the slope. Comparing figure 4.5(b) to figure 4.5(a) and figure 4.5(d) to 4.5(c), we see the same general behaviour from both surfaces: gradually changing acceleration accompanied by the reduction in flow height enforced by mass conservation. For both surfaces we see a general trend of increasing velocity for both increasing q and θ. Figure 4.6 plots the volume fraction multiplied by the shape parameter s_1, calculated using the expression $q = \rho\phi s_1 w h u_s$. This, in all cases, is in the range $0.3 - 0.7$. A Bagnold profile has $s_1 = 3/5$, so for a typical volume fraction of $\phi = 0.6$ we should expect to see a value $\phi s_1 = 0.36$. This is indeed the case for the rough base, indicating that the Bagnold profile assumption is reasonable in the calculation of the friction coefficient. Higher values of $s_1\phi$ indicate the presence of some slip developing at the basal surface.

For plug flows, we expect $\phi s_1 = 0.6$ which is closer to the value seen on the smooth base. However, values seen in figures 4.6(c) and 4.6(a) show that the observed values are slightly lower than predicted, indicating that some curvature is present in the z direction and the basal slip velocity is therefore less than the mean surface velocity. This is to be expected since the plug-like profile is a zeroth order approximation of the flow. Variation in ϕs_1 down the slope is small.

The different bases produced different behaviours with respect to the bulk friction coefficient. For the rough base, a Bagnold depth dependence has been assumed in the calculation of μ_t in equation (4.30). The precise choice of depth dependence does affect the calculated value slightly. Since the difference in s_2 at extremes of Bagnoldian and plug flow is a factor of approximately 2, we may safely say that the deviation of μ_t from the equilibrium value of $\tan\theta$ can at most be affected by this much. However, the qualitative behaviour remains unchanged by the assumed depth dependence. Figure 4.7(a) shows that on a rough base, μ_t varies from around 0.55 to 1.1. The inset of figure 4.7(a) shows that the ratio $\mu_t/\tan\theta$ is less than the steady-state value of 1 for all flows, and no lower than around 0.8. The very lowest values of μ_t are attained for low inclinations, where the flows are steady. The friction balances gravity in these flows despite the inclination being above the angle of maximal resistance θ_2, as the sidewalls give an extra frictional contribution. At higher inclinations, we see a dependence on q appearing: the lower the value of the flux q, the lower the bulk Fr, and the smaller the range of μ_t down the slope. For a given Froude number and inclination, the

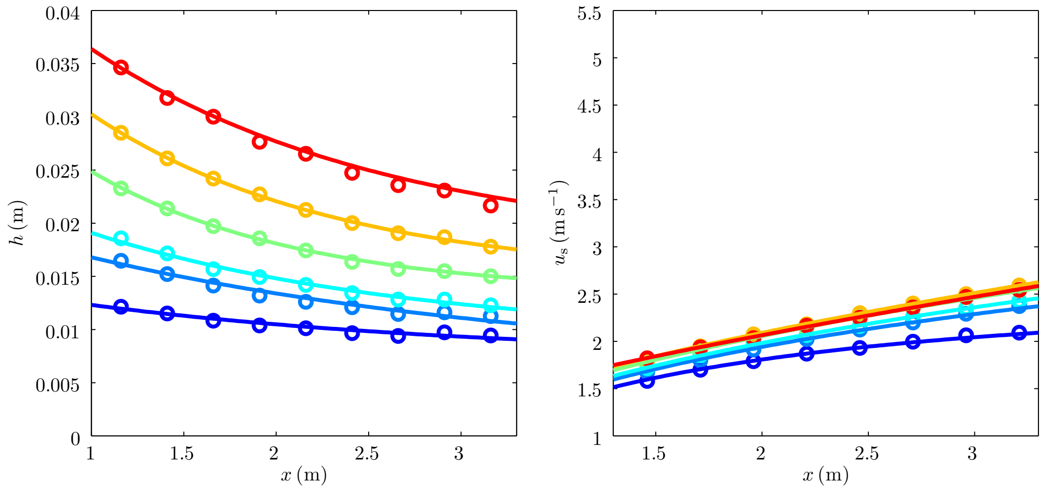

(a) Varying q at $\theta = 32.2°$ on the smooth surface.

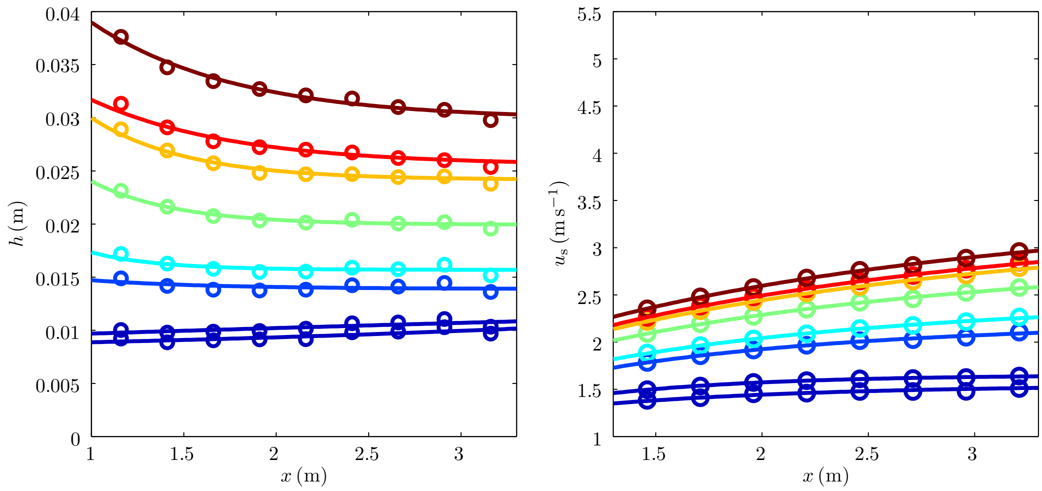

(b) Varying q at $\theta = 38°$ on the rough surface.

Figure 4.5: *Effect on the development of the average height of the flow h and the maximum surface velocity u_s as the flux q is varied for a specific inclination θ on the rough and smooth bases.*

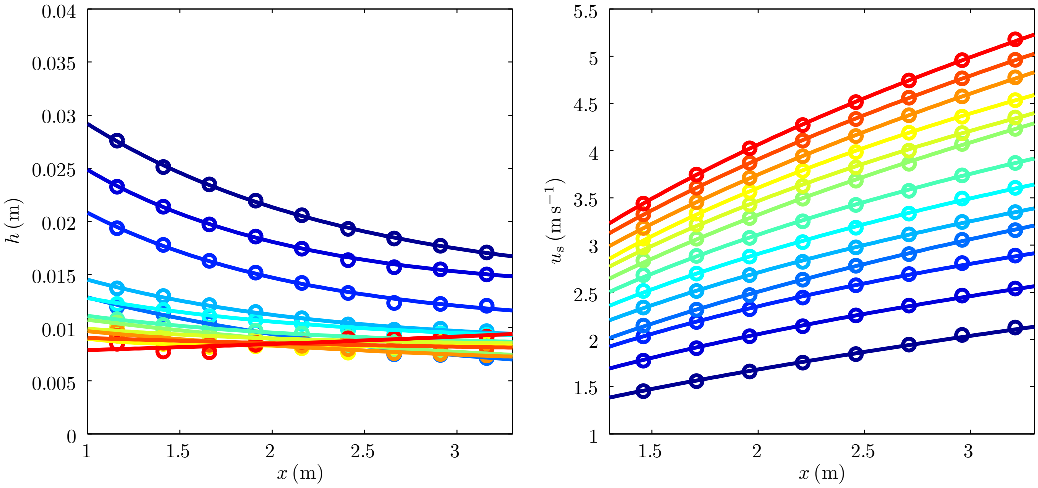

(c) Varying inclination for $q = 11\,\mathrm{kg\,s^{-1}}$ on the smooth surface.

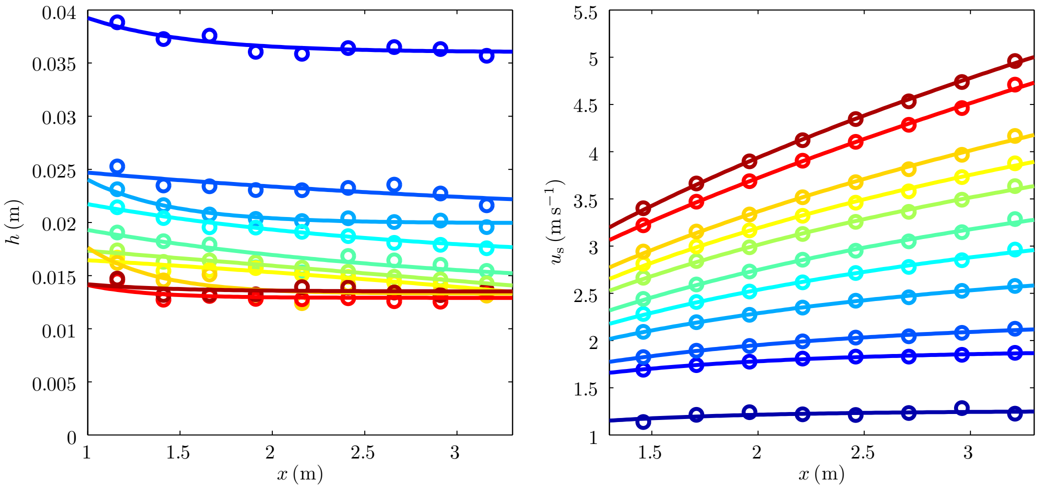

(d) Varying inclination for $q = 11\,\mathrm{kg\,s^{-1}}$ on the rough surface.

Figure 4.5: *Effect of varying the inclination θ at a specific q on the rough and smooth bases.*

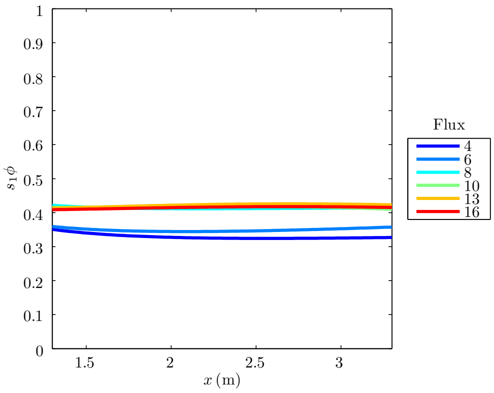

(a) Varying q,$\theta = 32.2°$, Smooth

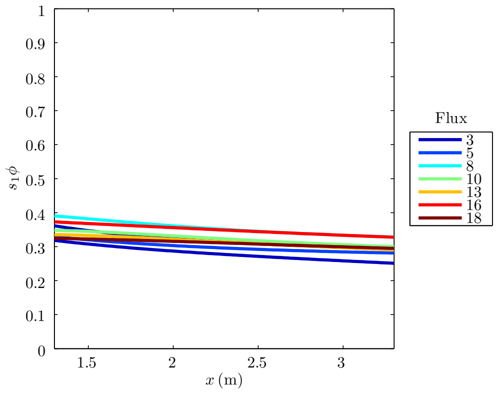

(b) Varying q,$\theta = 38°$, Rough

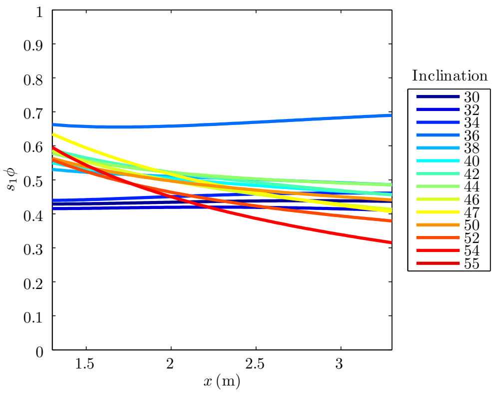

(c) Varying θ, $q = 11\,\mathrm{kg\,s^{-1}}$, Smooth

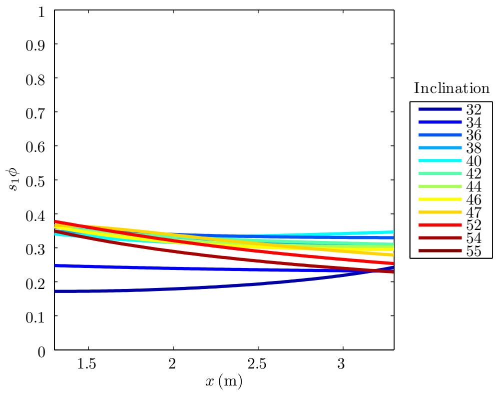

(d) Varing θ, $q = 11\,\mathrm{kg\,s^{-1}}$, Rough

Figure 4.6: *Variation of $s_1\phi$ on both surface types as q, θ and x are varied for specific values of q and θ.*

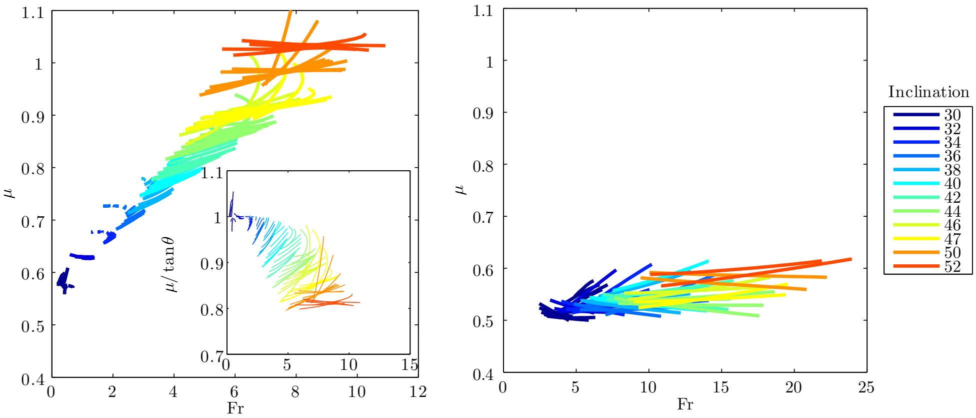

(a) Rough base (b) Smooth base

Figure 4.7: *The total friction* μ_t *as a function of* Fr. *Coloured by inclination. A Bagnold depth dependence is assumed for flows over the rough surface, and a plug flow for the smooth surface. Inset shows* μ_t *divided by the value attained for a non-accelerating flow,* $\tan\theta$*.*

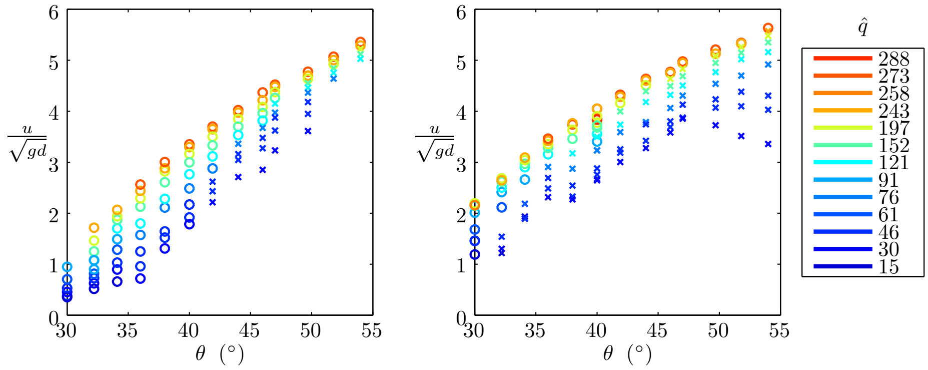

(a) Rough Base (b) Smooth Base

Figure 4.8: *Non-dimensional velocity* $\frac{u}{\sqrt{gd}}$ *at the end of the chute as the inclination* θ *and the flux* q *vary. Flows that are dense across the entire width are denoted by* ($\circ$)*, and flows that have undergone transverse inelastic collapse are denoted by* ($\times$)*.*

highest values of μ_t are seen for the flows with smaller flow heights. A qualitative explanation can be given in terms of the dilatancy. The grains close to the rigid rough surface experience a higher resistance to flowing due to the increased ordering and entanglement of the material near a rigid surface (Pouliquen, 1999*b*; Pouliquen & Renaut, 1996).

Figure 4.7(b) shows that on a smooth base, there is only a weak variation of $0.5 < \mu_t < 0.6$ for all Fr. This is slightly larger than the maximal friction angle obtained from the h_{stop} measurement of $\mu_t = 0.45$. This disparity is possibly due to the addition of wall friction. The flux dependence over the smooth base is more complicated than for the rough base, and is briefly discussed in section 4.5.

Figure 4.8 shows the velocity of the material at the end of the chute as a function of the inclination θ. The exit velocity for a given inclination is monotonically increasing with the flux, and is reflected in the decreasing value of μ_t as the flux increases. For terminal velocities in very long chutes one can set μ_t as a constant and assume Fr is large at equilibrium. We can then integrate equation (4.28) to obtain

$$\frac{1}{2}u_{\text{s}}^2 = \frac{1}{s_2}\left(\sin\theta - \mu_t\cos\theta\right)xg + \frac{1}{2}u_0^2, \tag{4.35}$$

4.4 Secondary effects

4.4.1 Inelastic collapse

When the flows are sufficiently energetic, a phenomenon similar to inelastic collapse occurs whereby a dense region in the centre of the chute is flanked by two high energy, low ϕ regions. For a given inclination, the value of q at which this occurs is lower on a smooth base than on a rough base. This is possibly due to the rough base dampening the high energy particles at the boundary. Since the interaction with the boundary in this regime is different to that of the fully dense flows, a direct comparison in terms of μ_t becomes meaningless, and so these experiments have been excluded from figure 4.7(b). The data denoted by crosses in figure 4.8 show the values of θ and q for which the flow visibly separates from the walls before the material exits the chute. At a fixed inclination, the separation disappeared for sufficiently high mass fluxes. We discuss this phenomenon in more detail in chapter 5.

4.4.2 Surface waves

Shallow flow systems are subject to instabilities known as roll waves or Kapitza waves (Forterre, 2006), owing to the tendency of deeper regions to move faster. This is typified by the flow rule in equation (2.32). For the flows investigated here, these waves occurred at angles near θ_2 for moderate flow rates. The space–time plot in figure 4.9 shows the amplitude of the waves on a slope of 32.2° at a mass flux of $5.9\,\mathrm{kg\,s^{-1}}$. The time-averaged height has been subtracted at each position, and the general trend of decreasing height as the flow develops down the slope is apparent. The colour difference has been normalised such that white corresponds to a 5 mm deviation above the mean height and black represents a 5 mm depression. Waves appear soon after exiting the hopper with an amplitude of around 2–3 mm and a wavelength of 404 mm. Half way down the slope, at 2.05 m after release, the amplitude has increased by a factor of two and the wavelength has increased slightly to 564 mm. The last reading, which shows little surface variation, would suggest that the flow has crossed some threshold and the disturbance has reached equilibrium amplitude. The linear theory presented in Forterre & Pouliquen (2003) gives a stability threshold of $\mathrm{Fr} \gtrapprox 0.7$, above which the flow is susceptible to these surface waves. The phase speed of the waves is in agreement with the velocity calculated using PIV to within 5%.

4.4.3 Convection currents

Figure 4.10 shows typical behaviour for the horizontal velocities at the surface of a flow over a rough base. There is a down-welling at the walls which is accompanied by an up-welling around 2 cm toward the centre, reminiscent of wall-cooling. Such patterns have been observed before but they are contrary to the inferred flow field in studies such as Savage (1979). We see that in figure 4.10 the horizontal velocity is of the order of 1% of the downstream velocity. The maximum seen across all of our data was less than 5%.

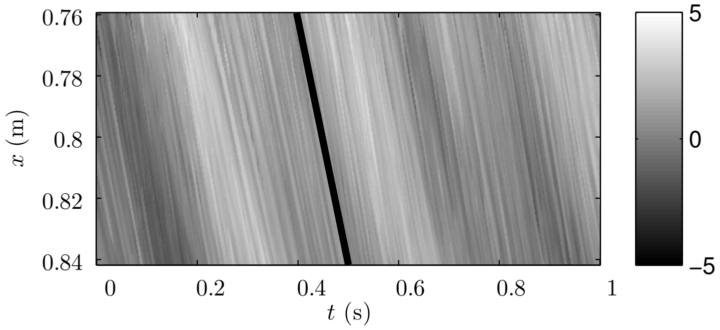

(a) $x = 0.8\,\mathrm{m}$, $v = 0.8\,\mathrm{m\,s^{-1}}$, $h = 0.047\,\mathrm{m}$, $\mathrm{Fr} = 1.35$

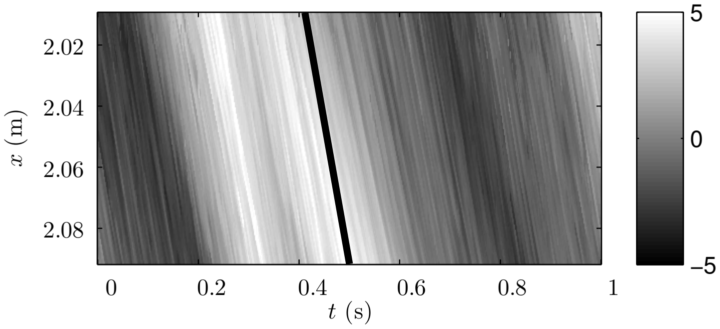

(b) $x = 2.05\,\mathrm{m}$, $v = 0.94\,\mathrm{m\,s^{-1}}$, $h = 0.037\,\mathrm{m}$, $\mathrm{Fr} = 1.68$

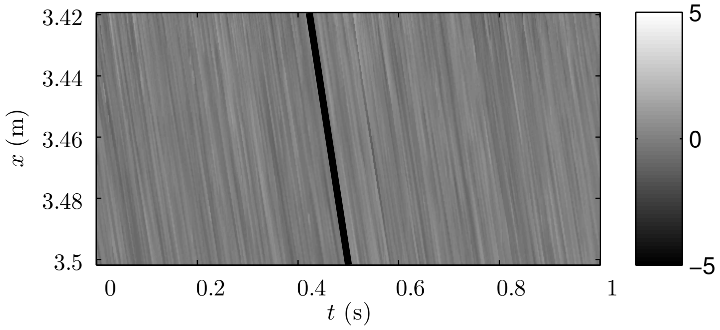

(c) $x = 3.46\,\mathrm{m}$, $v = 1.06\,\mathrm{m\,s^{-1}}$, $h = 0.030\,\mathrm{m}$, $\mathrm{Fr} = 2.18$

Figure 4.9: *Variation in height at $\theta = 32.2^\circ$ $q = 5.9\,\mathrm{kg\,s^{-1}}$. The colour represents a deviation about the mean in mm. The black lines indicate the calculated velocity from PIV measurements, showing that the waves' group and phase velocities are equal.*

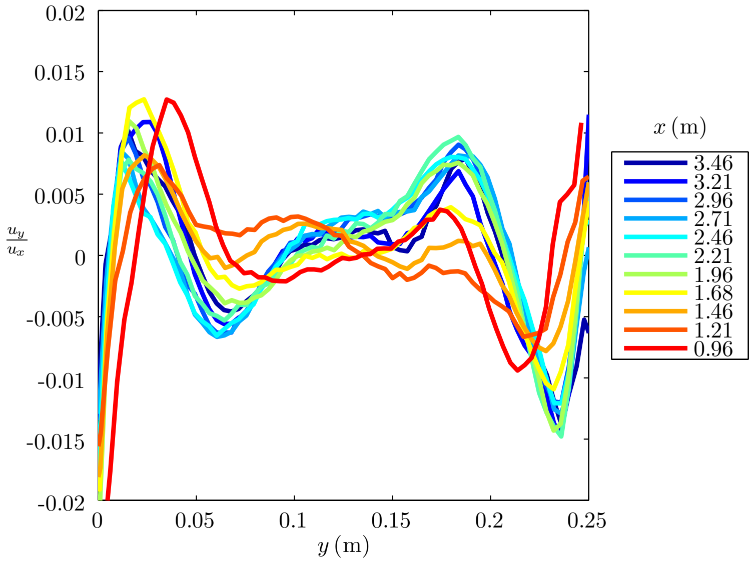

Figure 4.10: *Surface horizontal velocity normalised by the mean downstream velocity for a flow on a rough base with* $\theta = 44°$ *and* $q = 13\,\mathrm{kg\,s^{-1}}$.

4.4.4 Longitudinal vortices

Figure 4.11 shows the flow over a rough base with $\theta = 40°$ and $q = 5.5\,\mathrm{kg\,s^{-1}}$. Approximately 3 m after the sand is released, peaks in the downstream velocity develop, similar to those seen by Börzsönyi *et al.* (2009) and Forterre & Pouliquen (2001). A linear stability analysis using the kinetic theory of Lun *et al.* (1984) was performed by Forterre & Pouliquen (2001) and was used to predict the formation of the longitudinal vortices. The quantitative agreement with experimental data was limited, but this was expected as the kinetic theory in its original form is ill-suited to high volume fractions. However, using an analogy with Rayleigh-Bénard convection, it was clear that since the equations possess terms very similar to those for a Newtonian compressible thermofluid, the overturning mechanism could be captured. Since at a rough boundary fluctuations of the grains are produced by the working of the shear on the stress, a rough base modelled with a Fourier heat conduction law acts as a heat source with a cold, dense region above.

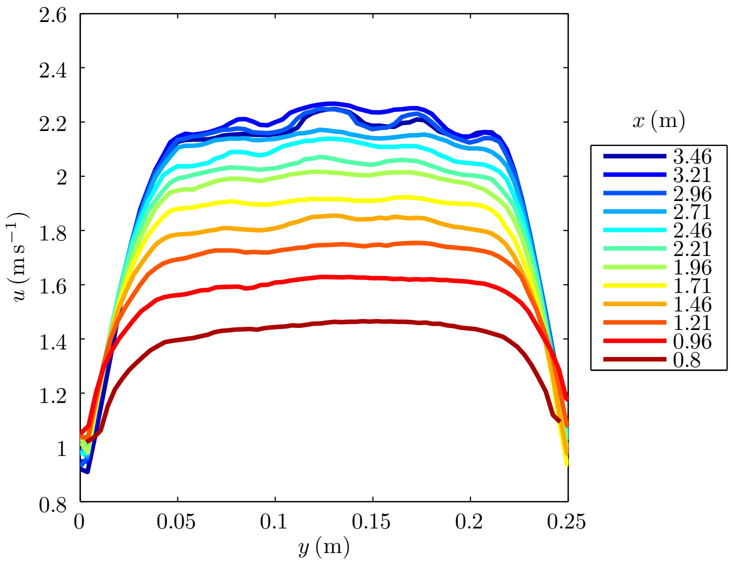

Figure 4.11: *The formation of longitudinal vortices on a rough base with* $\theta = 40°$ *and* $q = 5.5\,\mathrm{kg\,s^{-1}}$*. The height decreases monotonically from 17*mm *at the top of the chute to 11*mm *just before the exit.*

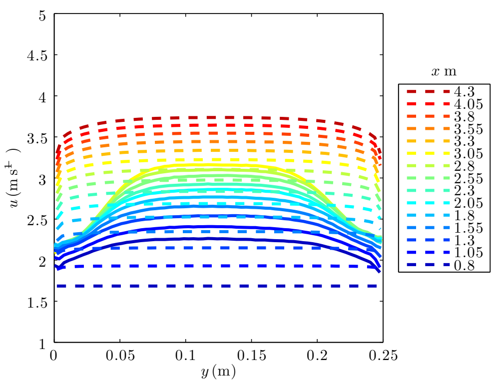

(a) Surface velocities

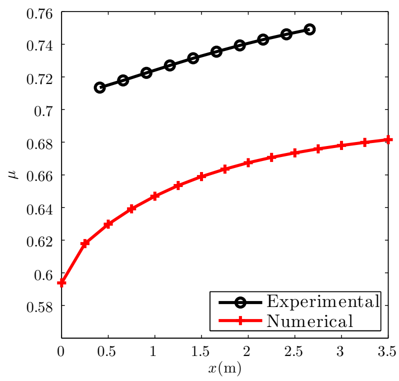

(b) Total friction μ_t

Figure 4.12: *Experimental and numerical friction and velocity over a rough base at* $\theta = 38°$ *and* q =*17.8*$\mathrm{kg\,s^{-1}}$ *using parameters* $\mu_1 = 0.54$, $\mu_2 = 0.68 = \tan(34°)$ *and* $I_0 = 0.3$. *Panel (a) shows the surface velocity profiles as it changes down the slope (i.e. as* x *increases) of both the experiments (solid lines) and the results of the finite volume code presented in chapter 2. It can be seen that the* $\mu(I)$ *rheology predicts an incorrect shape of profile. Panel (b) shows that the observed experimental friction is far higher than that predicted using the* $\mu(I)$ *rheology.*

4.5 Discussion

The $\mu(I)$ rheology has been developed and validated primarily for equilibrium flows with low I. However, the transverse surface velocity profiles that are produced by the simulations exhibit a qualitative difference to non-equilibrium flows observed experimentally. The numerical calculations show that there is invariably a smooth change of gradient over the entire width of the chute in the $\mu(I)$ rheology, as opposed to the experimental profiles on the rough base which have three linear regions. A comparison between the numerical and experimental flows on an inclination slightly higher than θ_2 is shown in figure 4.12. We see that the total friction μ_t for the experimental data is much higher than than the total friction predicted using the $\mu(I)$ rheology.

For inclinations below the maximum friction angle, good quantitative agreement of the average velocity u_s and total friction μ_t can be achieved by changing the rheological parameters from their experimental values. It is also possible to closely match the slip velocity at the wall by changing the wall friction coefficient. Any change of μ_w only has a small effect on the average velocity since its effect is weighted by the aspect ratio h/W (see equation (2.58)), and can therefore be independently chosen to match the wall velocity.

This comparison with experiments of accelerating flows and high I shows a poor agreement with our data. One crucial difference is the existence of the limiting value of friction in equation (2.58) as the flow develops and thins. For this rheology, which takes its parameters from h_stop experiments, the limiting value is independent of the inclination of the flow. A comparison between the numerical results in figure 2.13 and the data presented in figure 4.7 strongly suggests that experimentally this is not true. For inclinations where $\theta > \tan^{-1}\mu_2$, the $\mu(I)$ rheology predicts a total friction value of μ_2. However, we observe steadily increasing values much larger than those measured in the h_stop experiments.

Unless explicitly mentioned, all experimental data presented here appear dense at the free surface. Without this property, accurate measurements could not be made with our equipment. We can indirectly examine the averaged volume fraction by using the equation for global conservation of mass $q = s_1 u_\mathrm{s} h w \phi \rho$. However, care must be taken with the unknown shape parameter s_1 in order to gain information about the volume fraction. The parameter s_1 is the product of

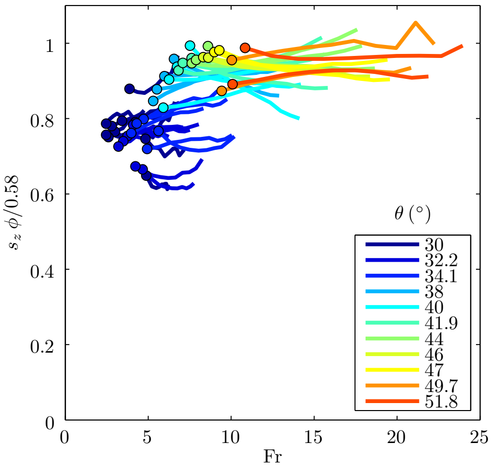

(a) Smooth base

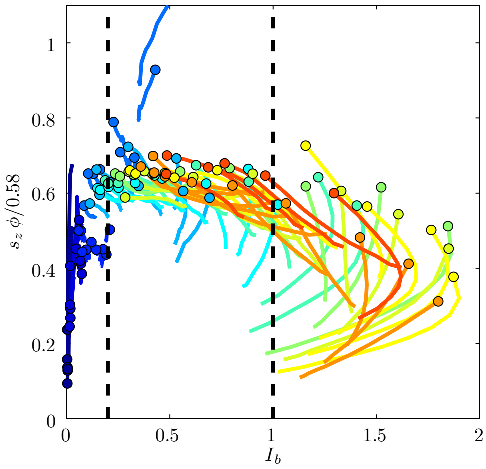

(b) Rough base

Figure 4.13: *Plot of* $s_z\phi/0.58$*, coloured by inclination. The dots indicate the measurement at the top of the chute. The rough case is plotted against* I_b*, and the smooth against* Fr*. The lines in (b) indicate the region where a Bagnold profile is likely.*

two contributions: one from the z depth dependence and from the y transverse dependence i.e. $s_1 = s_y s_z$. We define s_y as

$$s_y = \int \left.\frac{u}{u_s}\right|_{z=0} \mathrm{d}y, \tag{4.36}$$

i.e. a function of the velocity profile at the surface. We can then use this to calculate the product $s_z\phi$.

Figure 4.13 shows $s_z\phi$ normalised by a packing fraction of 0.58, a typical volume fraction as measured by Louge & Keast (2001). A value of 1 indicates a plug-like depth dependence, which figure 4.13(a) suggests is a reasonable approximation for $\theta > 36°$ on the smooth base. Lower inclinations have a lower value of s_z, indicating more curvature of the profile. Indeed, for the lowest inclinations a value of 0.6 is attained, suggesting that a Bagnold profile is also possible for a smooth base.

The rough base exhibits a larger range of s_z as can be seen in figure 4.13(b). At the very lowest inclinations, the value of s_z is small and suggests the presence of a static region at the base of the flow, similar to those seen in Taberlet *et al.*

(2003). These are only seen for inclinations below the maximum friction angle θ_2. For inclinations $> 36°$ and $I_b < 1$, $s_z\phi$ remains very close to 0.6, suggesting a Bagnold profile. In this region, there is a slight decrease with I as seen before by Forterre & Pouliquen (2008) and Baran *et al.* (2006), owing to the packing fraction decaying as I increases. For higher values of I_b, the flow becomes slightly more dilute at the top surface and a slip velocity develops at the base. It must be noted that for smaller values of I_b the flows have a very well defined surface, with exceedingly few saltating particles. A combination of these two factors gives rise to the large variations in $s_z\phi$, with its value ranging from more than 0.6 to less than 0.2.

Despite the flow remaining dense in the accelerating regime, the grains are not acting in the frictional manner described by the $\mu(I)$ rheology. To first order, the grains are acting as a pseudo-viscous fluid: the resistance of the fluid is roughly proportional to Fr (see figure 4.7(a)), rather than being bounded above by μ_2.

There are a number of possibilities that could account for the extra resistance required to reconcile the rheology with the experimental data. One of them is that the pressure is strongly non-isotropic. If the lateral pressure is much greater than that in the vertical direction, the frictional force at the wall will be much larger. Another possibility is the effect of air drag on the particles at the surface. The drag force on a spherical particle is given by a Stokes drag modified by a turbulent drag factor (see Börzsönyi & Ecke, 2006)

$$F_{\mathrm{drag}} = 3\pi\mu_{\mathrm{air}} d v c(v), \tag{4.37}$$

where μ_{air} is the dynamic viscosity of air and $c(v)$ is given by $c(v) = 1 + 0.15(vd\rho_{\mathrm{air}}/\mu_{\mathrm{air}})^{2/3}$. This formulation has been used to successfully predict the terminal velocities of a number of types of grains in Börzsönyi & Ecke (2006). Taking the expression (4.37) and forming the ratio to the gravitational force gives the relative magnitude of the drag effect

$$\frac{F_{\mathrm{drag}}}{mg} = \frac{18\mu_{\mathrm{air}} v c(v)}{d^2\rho}. \tag{4.38}$$

The velocity at which the drag is equal to the gravitational forcing is around $7.5\,\mathrm{m\,s^{-1}}$ but only affects those particles saltating away from the bulk above the

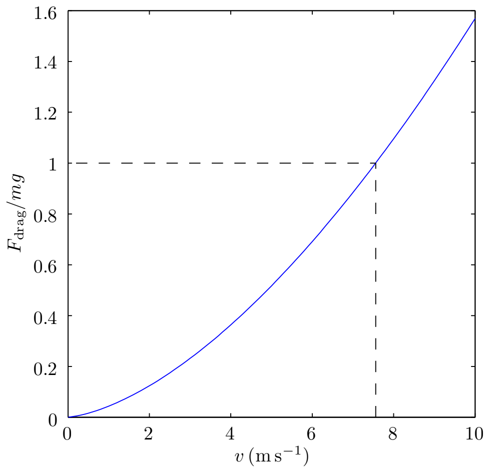

Figure 4.14: *The relative effect of gravity and the turbulent air drag on a spherical particle falling vertically in an ambient fluid.*

free surface. The corresponding Reynolds number is 750. Figure 4.14 shows the size of this ratio as the velocity varies. After the particles are ejected, they rejoin the flow shortly afterwards under gravity, and so this prediction of the terminal velocity is an upper bound and will not be reached in practice. This effect is also reduced by the flowing grains shearing the air immediately above. This means that the ambient fluid is not at rest, the relative velocities are lower and the drag is reduced. Another air-induced effect is the stress exerted by the stationary air on the free surface of the flow. However, a Prandtl boundary layer analysis reveals that this effect is small, and is around 0.1% of the gravitational forcing (see Börzsönyi & Ecke, 2006, for more details).

It is perhaps pertinent to note that the kinetic theory of Lun & Savage (1987), which is compared to the $\mu(I)$ rheology in Forterre & Pouliquen (2008), is not able to predict such high total friction coefficients either.

The h_{stop} definition of μ_1 and μ_2 combines properties of the flowing grains and the bed. It may be that at high I the nature of the flow near the surfaces changes and that it can generate much larger effective friction. Different regimes, such as the "supported" regime of Taberlet *et al.* (2007), have been observed, though they found roughly the same friction.

The pseudo-viscous effect for large I suggests that including higher order terms as an extension to the $\mu(I)$ rheology might be a good approximation. Such a form is

$$\mu(I) = \frac{\mu_1 I_0 + \mu_2 I + cI^2 \left(\frac{d}{h}\right)^\alpha}{I_0 + I}, \tag{4.39}$$

where the constants a, b, c and α are used as fit parameters. This form captures the general linear behaviour of μ for large I but is unable to capture the second-order dependence on either q or θ. The result of the fit can be seen in figure 4.15(a).

Plotting μ as a function of either Fr or I_b leaves unresolved dependencies on both q and θ. There are three non-dimensional groups in the problem, namely Fr, n, and θ, which can be used to find a scaling law. Defining a combination of the first two as

$$I_\alpha = \frac{\mathrm{Fr}}{n^\alpha} \tag{4.40}$$

gives a modified version of I_b which collapses the data over q for each inclination for a choice of $\alpha = 1/3$ for accelerating flows. The fit is shown in figure 4.15(b) which suggests a linear dependence between $\mu/\tan\theta$ and $I_{1/3}$

$$\frac{\mu}{\tan\theta} = a(\theta) I_{1/3} + b(\theta) \tag{4.41}$$

for some choices of $a(\theta)$ and $b(\theta)$. The data suggest that a and b share an asymptote as well as the position at which their gradient tends to zero and as such, the functional form of the h_{stop} curve in equation (3.21) is well suited to this. We can write

$$a(\theta) = B\left(\frac{\tan(\phi_2) - \tan\theta}{\tan\theta - \tan(\phi_1)}\right) \tag{4.42}$$

where, upon fitting, $B = 0.03$, $\phi_1 = 23.1°$ and $\phi_2 = 55.9°$. This gives the representation

$$\frac{\mu}{\tan\theta} = a(\theta)\left[1.5 + I_{1/3}\right] + 0.75. \tag{4.43}$$

This relationship removes the friction angles deduced from h_{stop} experiments from the rheology and replaces them with two other generalised friction angles. The larger angle corresponds to the point after which $\mu/\tan\theta$ is constant, and is coincidentally the highest inclination for which experiments were carried out. At these high inclinations, μ saturates at around $0.8\tan\theta \approx 1.1$ which is much higher than the upper friction coefficient $\mu_2 \approx 0.6$ as measured from h_{stop} experiments.

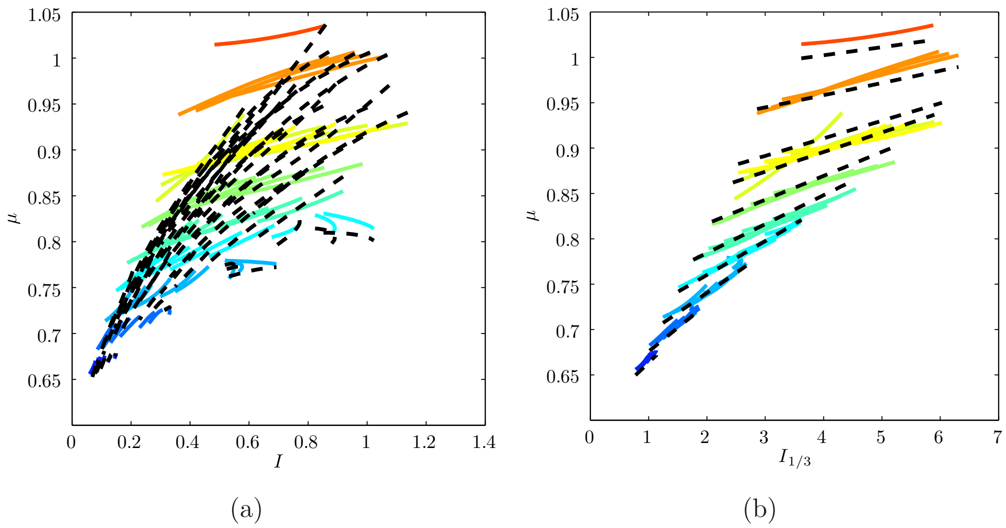

Figure 4.15: *Fitting the total friction* μ_t *(a) Fit with* I^2 *extension to the* $\mu(I)$ *rheology. Solid lines are the experimental data, black, dashed lines are the fit curves. The fitting parameters were* $\mu_1 = 0.58$, $\mu_2 = 0.82$, $I_0 = 0.37$, $c = 0.0015$, $\alpha = -2$. *(b)* μ *plotted against* $I_{1/3}$ *(time-steady flows removed). Black, dashed lines give fit of data using the* θ *dependence in equation* (4.43).

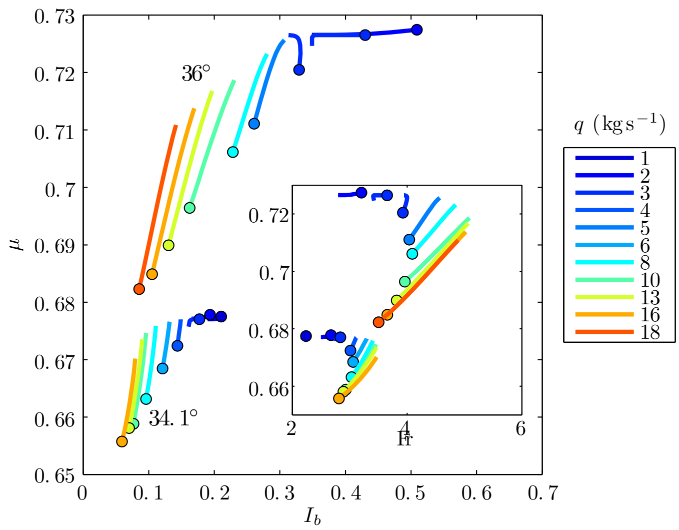

Figure 4.16: *Behaviour of total friction* μ_t *at low inclinations as a function of* I_b *and* Fr. *Dot indicates measurement at top of chute.*

In order to reconcile this analysis with previous studies, it is necessary to investigate the angles for which equilibrium states exist in more detail. We plot μ as a function of I_b for two inclinations in figure 4.16 and against Fr in the inset. The first inclination, $\theta = 34.1°$, is just below the angle of vanishing h_{stop} $\theta_2 = 34.2°$, and the second one above at $\theta = 36°$. At the lowest mass fluxes, both inclinations indeed exhibit flows with a constant friction coefficient. For the lower inclination, these flows are not accelerating, as constant Fr (or equivalently I_b) is achieved down the slope. At the higher inclination, Fr and I_b decrease as the flow progresses. The start point for each flow is marked with a dot. The values of μ for these flows are in agreement with the values recorded in the h_{stop} experiments, and therefore also agree with the numerically-investigated rheology. A slight complication is introduced as μ is no longer a single-valued function of either Fr or I_b, possibly due to the stabilising influence of the sidewalls. The change in μ at $\theta = 36°$ as q varies is around 7%, and drops to 4% for 34.1°. It is also interesting to note that accelerating flows for these low inclinations are collapsed over q when using $I_{1/3}$ as the appropriate non-dimensional number, whereas the flows with constant μ are not. Steady μ flows for $\theta < \theta_2$ are well explained by the $\mu(I)$ rheology as can be seen in figure 4.17. These flows are shown to follow the broad pattern predicted by the $\mu(I)$ rheology although there is some discrepancy. This discrepancy can partially be attributed to the presence of side walls. Including a sidewall friction such as that in the numerical model of chapter 2 suggests that

$$\mu_t = \mu_w \frac{h}{w} + \mu_b(I), \tag{4.44}$$

however fitting this functional form to the data in figure 4.17 with constant μ_w does not give good results. This expression does however gives some indication of why the same μ_t can exist for different I_b in steady flows i.e. through the varying height changing the total friction. It should be noted that the value of μ_2 taken from the h_{stop} experiments presented in figure 3.20 does not give a particularly good fit to the data in figure4.17. A slightly higher value of $\mu_2 = 0.8$ has been used instead.

In contrast, the accelerating flows need an extra rheological contribution to explain the behaviour. It is proposed that $I_{1/3}$ gives the appropriate scaling for

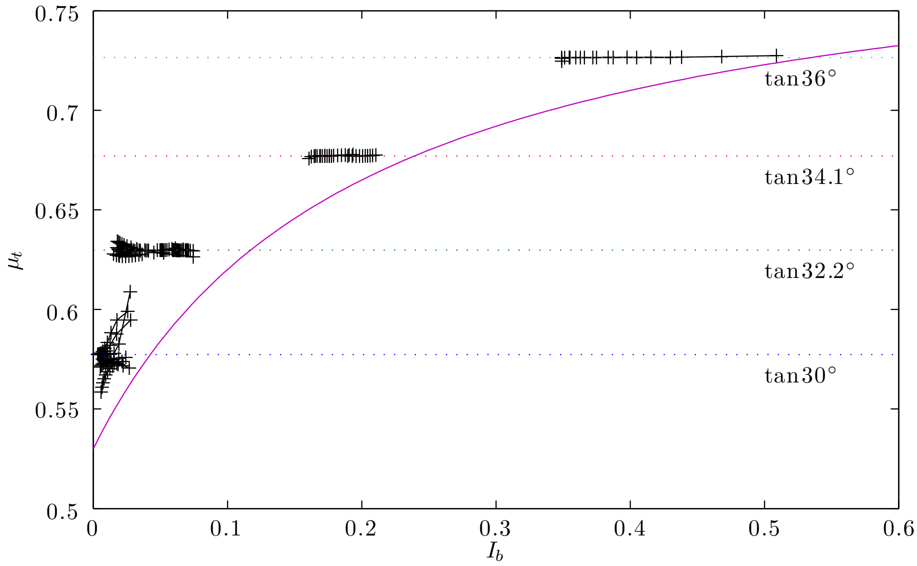

Figure 4.17: *Constant velocity flows for low inclinations on the rough base. Note there are a number of admissible I for each inclination possibly due to the effect of sidewall friction, thus making a best fit using the $\mu(I)$ equation unsuitable. The solid line represents a typical $\mu(I)$ curve with $\mu_1 = 0.53$, $\mu_2 = 0.8$ and $I_0 = 0.2$. These parameters gave a reasonable fit. Using the h_{stop} measurement for μ_2 did not give a good fit to the data.*

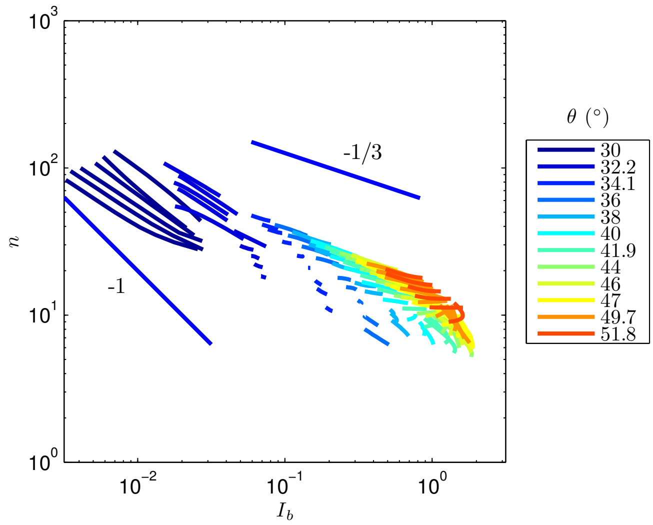

Figure 4.18: *Log plot of n against I_b for the rough base.*

these extra contributions.

A further indication of a difference in regime can be seen in figure 4.18, which shows a log-log plot of the dependence of h/d on I_b. Manipulation of the $\mu(I)$ equations (2.32) and (3.21) gives

$$I_b = -\alpha n^{-1} + \beta \left(\frac{\tan\theta - \mu_1}{\mu_2 - \tan\theta} \right). \tag{4.45}$$

The low inclinations for which this rheology is expected to work does exhibit a slope of gradient -1, but quickly changes as the inclination increases. The accelerating flows exhibit a behaviour such that $I_b \sim n^{-3}$. Given that μ is no longer simply a function of a parameter such as I_b, and different scalings are required to collapse the accelerating and constant μ regimes, it is possible that other flow variables such as granular temperature are needed to fully describe the system.

The form proposed in equation (4.43) predicts that the flow cannot reach a steady velocity above $\theta = \phi_2$. Below this threshold, the terminal state is given by $I_{1/3} = 0.25/a(\theta) - 1.5$. Above this threshold, the total friction μ is always less than the maximum value $\mu = 0.75 \tan\theta$, resulting in a constantly accelerating flow.

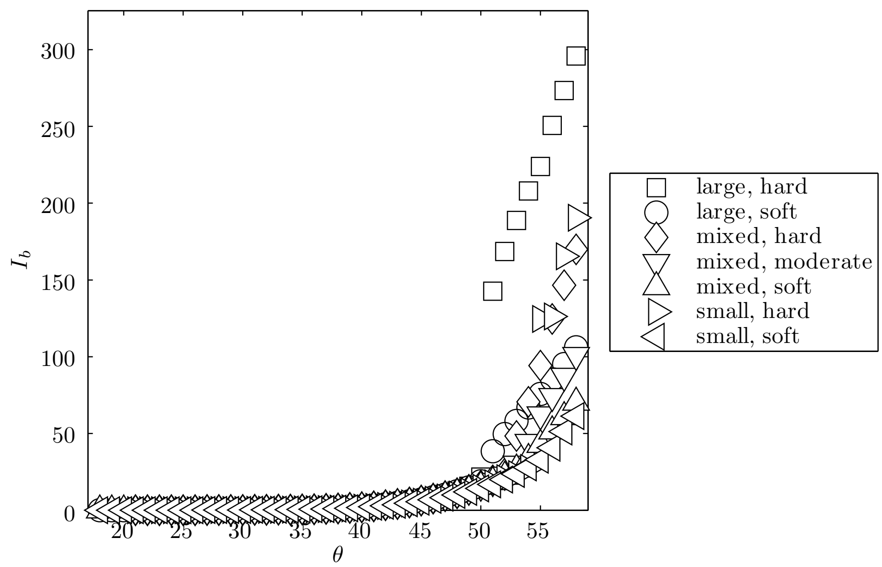

Figure 4.19: *Terminal state of DEM flow simulations using different particle species. The time-steady state value of I_b is plotted for various q and θ. Reproduced from Holyoake & McElwaine (2011), using the method described in Börzsönyi* et al. *(2009).*

However, DEM simulations for flows on high angles suggest that non-accelerating states can exist, although they are not dense throughout their depth. The code used to produce these results is a soft particle model using a damped linear spring for the normal force and a Coulomb friction for the tangential force. The method is the same as that explained in Börzsönyi *et al.* (2009). The particles in the simulation have an inter-particle friction coefficient of 0.5 and coefficient of restitution 0. The particle stiffness was chosen to ensure that the maximum particle overlap in a head-on collision was less than 1% of the particle diameter. The basal surface is formed by a mix of two types of particles in a random configuration. Figure 4.19 shows the steady state value of I_b for multiple θ, q, and particle species. At these high values of I_b, the particle stiffness and size become important as the dissipation during inelastic collisions provides another mechanism for energy dissipation. For lower inclinations, the variation in terminal I_b is very small between different particle species. For the high inclination flows, the final state is periodic. The flow separates from the base and shortly after falls, colliding with the base and dissipating energy. This allows $\mu \to \tan\theta$, at least in an averaged sense. In order

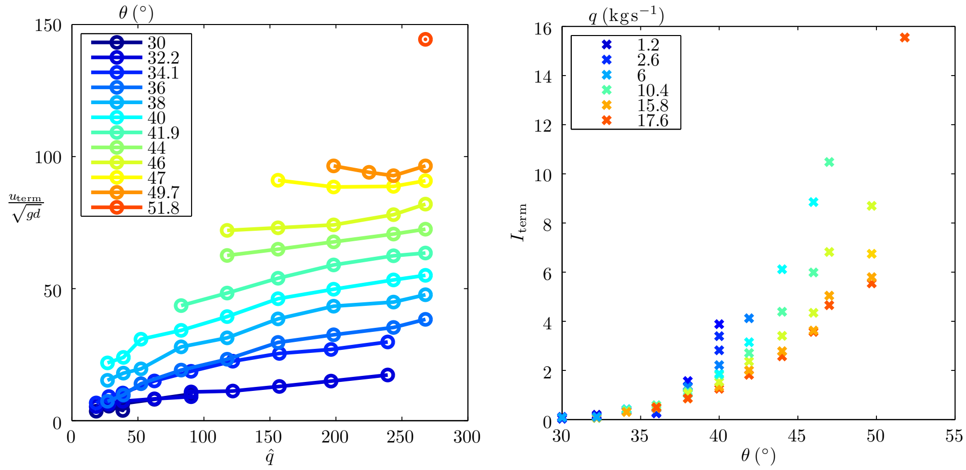

(a) (b)

Figure 4.20: *(a) The non-dimensional terminal velocity of full-width flows on a rough base as predicted by the fit formula* (4.33)*. Each line represents the terminal velocities at a given inclination as the flux varies. (b) The terminal value of I, I_{term} as it varies with q and θ. The value of h used in the calculation is calculated from q, assuming a constant ϕ.*

to replicate this in the lab, the chute would need to be many kilometers long and, at these speeds, air drag would be important. It is also not clear if the ambient fluid would have a significant effect on the flow in this state.

The fitting function in equation (4.33) can also be manipulated to give a prediction of whether a terminal velocity v_{term} exists. If $\gamma > 0$, then v_{term} can be calculated by $v^2_{\text{term}} = u_0^2 + \delta/\gamma$. For flows with a constant velocity in the chute, v_{term} is taken directly from the data. Although care must be taken when extrapolating data outside of the observed range, all but one of the terminal velocities were less than double the velocity at the end of the chute. This indicates that it is not unreasonable to expect that the flow, when at the extrapolated velocity, is in a dense state similar to how it is observed in the chute, and so the extrapolated terminal state is a likely outcome. If the flow undergoes a phase transition then the development is likely to be substantially different to the extrapolated development.

Figure 4.20 shows the terminal velocity v_{term} and terminal inertial number I_{term} (when they exist) for flows over the rough base. Figure 4.20(a) shows v_{term} as a function of the control parameters θ and q. A clear structure is shown where the terminal velocity is a strong function of the inclination, especially at high inclinations. Indeed, for flows over 51.8°, no steady flows were predicted by the extrapolation, perhaps indicating that there is still an upper limit to the friction, albeit much higher than the values measured from h_{stop} experiments. The dependence of v_{term} on the mass flux q is also increasing. However, as q increases, the dependence weakens suggesting that the terminal velocity will become independent of the mass flux (and therefore the flow height). This is possibly due to the wall friction giving an increased contribution as the flow deepens.

The second subfigure 4.20(b) shows the terminal value of the inertial parameter I_{term} as a function of θ. If I is indeed the only parameter that governs the flow then we would expect total collapse of the data in this graph. However, there is still significant spread. Plotting the data in terms of $I_{1/3}$ as in figure 4.15(b) does not significantly improve the collapse of the data either.

The predicted values of the normalised steady state mass hold-up $\tilde{n} = n\phi/0.58$ can be seen in figure 4.21. In contrast to the $\mu(I)$ rheology, which predicts that flows on inclinations $\theta > \theta_2$ should have an indefinite, linear acceleration, we see that steady states are possible in this region. Also shown is the shaded region underneath the h_{stop} curve, in which a heap will form with a flowing layer on top of it. At the other end of the space, for high inclinations and small $\tilde{n}$, we see the predicted steady state for the separated flows. As no data was available for the dilute flows (as n is ill-defined), the boundaries of this area of the phase plane were estimated.

There are no data for very low fluxes $q < 1\,\text{kg}\,\text{s}^{-1}$ as the apparatus tended to produce a low energy, uneven saltating state, which is initiated by the drop from the hopper to the chute, making n ill-defined.

The flows over a smooth base did not exhibit such a rich range of behaviours. The data set was much smaller as inelastic collapse affected a large proportion of the flows, and has therefore been excluded from most of the analysis. Figure 4.7(b) shows that μ_t is invariably lower than on the rough base, as the smooth base gives less resistance. The range of μ seen over the small base is much lower, and is almost uniform for all Fr. This fits in well with the h_{stop} data, which only gave a difference of 0.2° between θ_1 and θ_2. As a result, the $\mu(I)$ model with

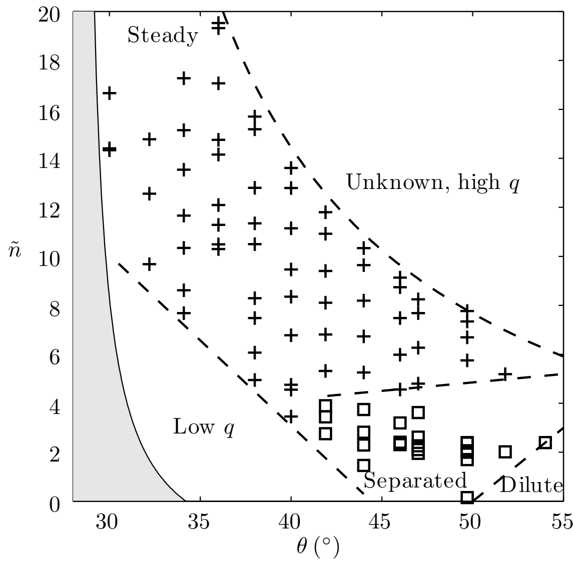

Figure 4.21: *Phase diagram showing how the predicted terminal mass hold up $\tilde{n}$ and θ vary on a rough base. (+) indicates flows with a predicted constant velocity terminal state and (□) indicates flows that have a predicted steady state, but have separated at the wall. No data exists for the dilute flows as n is ill defined there. There are also no data for low flow rates q as the apparatus was sensitive to cross slope variation in the initial condition for very thin flows. The shaded area shows where $h < h_{\text{stop}}$ and heap flow occurs.*

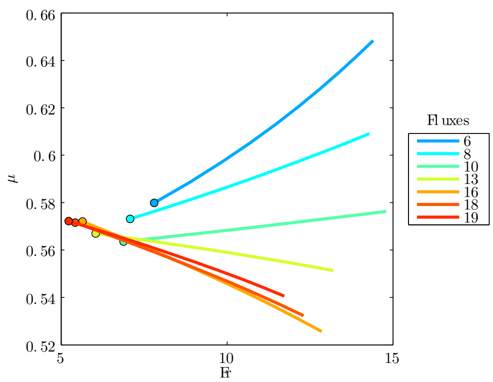

Figure 4.22: *A plot of μ on a smooth base, inclination 40° for varying fluxes. Dots indicate measurement at top of the chute.*

constant μ gives good agreement with the data. It it not clear if the flows on the smooth base will approach a terminal velocity in the same way as the rough base. Since the acceleration of these flows is approximately linear, the fit described by equation (4.33) is degenerate for three parameters, meaning that γ, and therefore the extrapolated terminal velocity, is very sensitive to small amounts of noise.

However, this zeroth order, sliding block model cannot capture the cross-slope velocity variation. As the flow accelerates, mass conservation dictates that if ϕ stays constant, then the height must decrease and the flow must elongate. This elongation will then excite an internal flow structure, generating transverse gradients in the stress and ultimately the cross-slope velocity profile seen at the surface.

Figure 4.22 shows an interesting dependence of μ on the mass flux for the smooth base. Low mass fluxes demonstrate the expected behaviour of μ increasing with Fr. However, as the mass flux increases, the gradient of this slope decreases until it becomes negative. This effect is seen for all of the fully dense flows investigated here. Having a negative gradient of $\mu(\mathrm{Fr})$, indicates that in this regime the flows will accelerate faster and faster until a flow transition occurs or other forces come into effect.

4.6 Conclusion

Previous work on granular flows has concentrated on $I < 0.5$ (MiDi, 2004). The $\mu(I)$ rheology and the flow rule $\mathrm{Fr} = \alpha + \beta \frac{h}{h_{\mathrm{stop}}}$ have been successful in predicting the dynamics of such flows. However, they suggest that flows on slopes steeper than $\theta = \tan^{-1} \mu_2$ will accelerate at a constant rate. Our experiments show that these models are inaccurate for larger θ and that steady flows may be possible on much steeper slopes. As such, this is an important prediction that should be tested in the future with different apparatus. We see a maximum total friction value of $\mu_t \approx 1.1$ which is much bigger than the value of $\mu_2 \approx 0.6$ derived from measurements of h_{stop}. We analyse the potential effect of air drag on the surface particles and conclude that it will have only a small effect. We also explore other scalings that collapse the total friction for flows that were observed to be in an accelerating mode.

A number of interesting instabilities were also observed. We found density instabilities where a dense core in the middle of the chute is flanked by dilute regions which grow in size down the chute. This process is similar to the inelastic collapse phenomenon seen in the literature and is explored in more detail in chapter 5.

We also saw a transition where the entire bulk of the flow becomes energised, unstable and dilute. A transverse velocity profile instability in the form of longitudinal vortices was also seen for intermediate inclinations.

Flows over the smooth base are well-modelled by constant total friction. Although there was some complicated variation with the Froude number and the flow depth, it was small compared to the range of the total friction on the rough base. However, a significant cross slope velocity variation was observed that is incompatible with standard granular models (such as Savage-Hutter), which presume a plug flow over smooth surfaces. Development of a model to capture these effects remains a subject for future work.

5

Inelastic Collapse

5.1 Introduction

In this chapter we examine an instability that occurs over a large portion of the phase space explored by our experiments in chapter 4. For low mass fluxes on a given inclination, the flow collapses into a dense central region flanked by two low density, high temperature regions. We made a brief mention of this in section 4.4.1 and we examined in which portion of the phase space this phenomenon occurs, as shown in the phase diagram 4.21. A typical flow that undergoes this transition can be seen in figure 5.1.

A number of similar phenomena have been observed in granular media before. Perhaps most fundamental in nature are the numerical investigations of Benedetto & Caglioti (1999) who observed one-dimensional collapse for sufficiently inelastic particles in which the end state had all particles touching in one chain. Numerical simulations of two-dimensional assemblies of particles have been observed to undergo clustering, which is an instability whereby growing inhomogeneities in the density field occur (Alam & Hrenya, 2001; Goldhirsch & Zanetti, 1993; McNamara

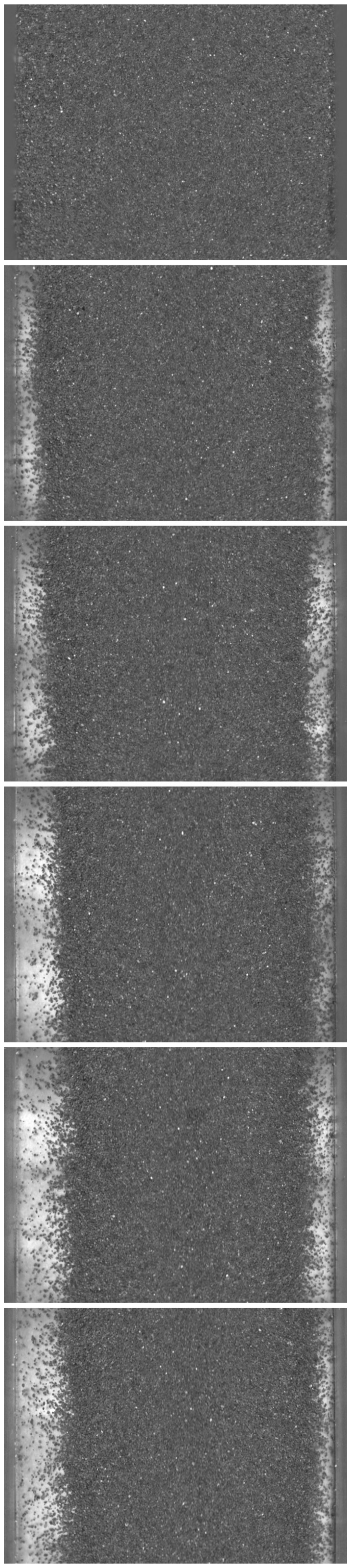

Figure 5.1: *A typical separated high-speed flow on the smooth base. The flow invariably starts occupying the entire width of the chute. The shear at the wall produces thermal agitation causing the volume fraction to drop and a dense core to remain. We use the term inelastic collapse to describe this phenomenon.*

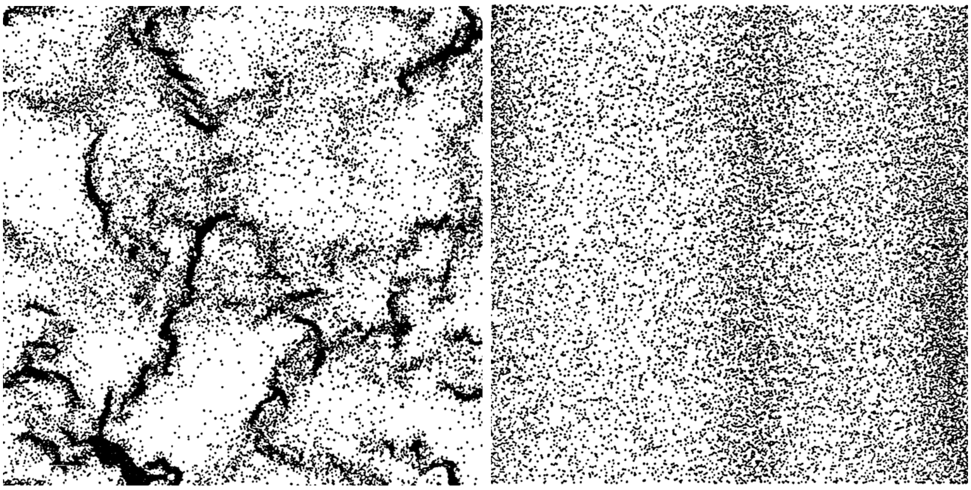

(a) Clustering (b) Stripe formation

Figure 5.2: *Clustering and stripe formation of inelastic particles. Reproduced from simulations by Goldhirsch & Zanetti (1993)*

& Young, 1994). Heuristically, this instability is the result of small fluctuations in the density field, where the density is slightly larger than the normal value. As a result, the collision rate of the particles increases, and therefore the rate of energy dissipation in the area also increases. As a result, and in contrast to a normal gas, both the temperature and the pressure decrease as the density increases. This effectively creates a sink where the energy of other particles colliding with the cluster gets absorbed and the size of the dense cluster increases. Clustering is often a precursor to inelastic collapse, where the particles undergo an infinite number of collisions in an finite amount of time, i.e. remain in continuous contact with each other. As a result, the particles will move as a plasticly deforming agglomeration unless other particles with sufficient energy collide with the group and break it up.

As the application of rheologies based on the Coulomb friction law (such as the $\mu(I)$ rheology) is unsuitable for low density flows, we turn to the granular kinetic theory of Lun *et al.* (1984), supplemented by the mean-field boundary conditions of Forterre & Pouliquen (2002). Chute flows have been investigated using this theory before (Ahn *et al.*, 1992; Ahn & Brennen, 1992; Anderson & Jackson, 1992), with some success for collisional flows. However, these studies have focused on two-dimensional flows, such that only a depth dependence is captured. This makes this work of limited relevance for describing the lateral variation that we observe experimentally.

Forterre & Pouliquen (2002) broke the transverse symmetry by extending this theory to look at the formation of longitudinal vortices which they argue are analogous to Rayleigh-Bénard convection. In their analysis, however, the flow was assumed to be infinitely wide, and so sidewalls played no role in governing the flow. A linear perturbation analysis was performed on a steady solution of the equations, the result of which gives good qualitative agreement with their experimental observations of vortical structures aligned with the flow. In our analysis, we look to include the effect of the walls on the flow and expect at most a qualitative agreement with our experimental data, as the kinetic theory in its basic form is known to have limitations in dense regions (Tan & Goldhirsch, 1997).

Recent adaptations of the kinetic theory include the use of a heuristically derived correlation length (Jenkins & Berzi, 2010) to account for the overestimation of the inelastic dissipation at high ϕ. Alternatively, critical state theory from soil mechanics (Berzi *et al.*, 2011) can also be used to correct the predictions for dense flows. However, these two modifications add a computational complication not necessary to capture the qualitative basic behaviour of our experimental observations. We proceed using the theory of Lun *et al.* (1984) with the addition of boundary conditions used in Forterre & Pouliquen (2002).

5.2 Background

The flows we have investigated are low temperature and dense and so a Coulomb rheology is, in principle, appropriate. However the presence of low density regions imply that locally the production of heat at the walls by the shear and the inelastic dissipation are no longer balanced. This would indicate that in order to model this phenomenon we must include the evolution of the temperature in a suitable theory. In low density areas of the flow the particles are strongly agitated, and the dominant momentum transfer mechanism are collisional rather than frictional contacts. This, traditionally, is named the kinetic or collisional regime. The dominance of collisional transport between grains suggests that a statistical physics description may be suitable. As such, we introduce a transport equation for the granular temperature, which plays a similar role to the thermodynamic temperature in standard kinetic theory. This temperature is distinct from the thermodynamic temperature discussed in the introduction, but is quantified in a similar way. The granular temperature T is, in general, the covariance tensor of the grain velocities.

Some of the first micro-mechanical studies of this regime were presented almost simultaneously by a number of people, e.g. Lun *et al.* (1984) and Jenkins & Savage (1983) to name but two. These theories were motivated by the studies of Chapman & Cowling (1939) pertaining to the dynamics of dense gases. However, there is a key difference between a granular gas and a thermal gas, namely the inelasticity of the collisions. As such, a granular gas must be subjected to a constant flux of energy in order to maintain its excited, collisional state, otherwise the gas will quickly condense to a dense flow. The kinetic energy contained in the granular temperature is then given by the balance between inelastic dissipation, the work of the shear on the strain and a heat flux. Naturally, the character of the boundaries can also determine whether there is a net production or dissipation of energy there. There are typically two different ways to input energy into such a flow to maintain the collisional regime. We can do this either by vibrating the walls, by shearing the material along a surface by applying a body force. The particles then bounce off the surface, transferring their momentum parallel to the surface to the direction normal to it. In both cases, a flux of temperature is created at the wall. In our experiments we generate temperature by shearing the flow along the walls.

5.3 Theory

The temperature T, which is crucial to expressing the equations of a granular thermo-fluid, is defined as $T = \frac{1}{3} < \delta u^2 >$, where δu are the random velocity fluctuations about the mean value. Following Jenkins & Richman (1985) we have assumed an isotropic temperature which is given by

$$T = \frac{1}{3}\left(\langle \boldsymbol{u}^2\rangle - \langle \boldsymbol{u}\rangle^2\right). \tag{5.1}$$

In the presence of gravity, the standard hydrodynamic equations are modified by an inelastic dissipation term γ, which means that the energy equation is non-conservative. The equations are derived by considering the collisional flux of mass, momentum and energy in a control volume. They are

$$\frac{\mathrm{D}\rho}{\mathrm{D}t} = -\rho\boldsymbol{\nabla}\cdot\boldsymbol{u}, \tag{5.2}$$

$$\frac{\mathrm{D}\left(\rho\boldsymbol{u}\right)}{\mathrm{D}t} = \rho\boldsymbol{g} + \boldsymbol{\nabla}\cdot\boldsymbol{\sigma}, \tag{5.3}$$

$$\frac{3}{2}\frac{\mathrm{D}\left(\rho T\right)}{\mathrm{D}t} = \boldsymbol{\sigma}\boldsymbol{:}\,\boldsymbol{\nabla}\boldsymbol{u} - \boldsymbol{\nabla}\cdot\boldsymbol{q} - \gamma. \tag{5.4}$$

The rate of change of the temperature is governed by three terms. The first, $\boldsymbol{\sigma}\colon\boldsymbol{\nabla}\boldsymbol{u}$, represents the production of T due to the work of the stress over the shear. The second term represents the flux of the fluctuation energy, and the third is a dissipative term caused by the inelastic nature of the grains' collisions.

The difference with normal thermodynamics appears in the form of the constitutive relations. Lun *et al.* (1984) modelled the granular material as a compressible Newtonian liquid with variable viscosity. As such, the stress tensor takes the form

$$\boldsymbol{\sigma} = -\left[p(\phi,T) - \xi(\phi,T)\boldsymbol{\nabla}\cdot\boldsymbol{u}\right]\boldsymbol{I} + 2\eta(\phi,T)\boldsymbol{S}. \tag{5.5}$$

The deviatoric part of the stress is

$$\boldsymbol{S} = \frac{1}{2}\left(\boldsymbol{\nabla}\boldsymbol{u} + \boldsymbol{\nabla}\boldsymbol{u}^{\top}\right) - \frac{1}{3}\left(\boldsymbol{\nabla}\cdot\boldsymbol{u}\right)\boldsymbol{I}, \tag{5.6}$$

for some functions p, ξ and η.

At this point, we take the simplest possible model that might model the phenomena and as such we assume that the flow is unidirectional and takes the form

$$\boldsymbol{u} = (u(y), 0, 0), \tag{5.7}$$

which represents a depth-wise plug as there is no depth dependence. This is motivated by our surface measurements of the velocity, which show that in the y direction the velocity is small compared to the downstream direction as can be seen in figure 4.10 on page 115. In this case, the conservation of mass is trivially satisfied with $\nabla \cdot \boldsymbol{u} = 0$.

The kinetic rheology also specifies the heat flux $\boldsymbol{q}$ and the internal dissipation γ as

$$\boldsymbol{q} = -\kappa(\phi, T)\nabla T, \tag{5.8}$$

$$\gamma = \frac{\rho_p}{d} f_5(\phi) T^{3/2}. \tag{5.9}$$

Here, we have adopted a classic Fourier heat diffusion for the flux $\boldsymbol{q}$, with the non-constant thermal diffusivity denoted by κ. However, a full model also takes a further contribution from the term $\nabla\phi$ into account. However this term only serves to increase the computational complexity while giving only a negligible increase in accuracy (Forterre & Pouliquen, 2002; Woodhouse *et al.*, 2010), and so we neglect it.

As in classical gases, the pressure p, the viscosity η and the thermal conductivity κ are functions of the local density (or, equivalently, the volume fraction ϕ) and the temperature T. They are given by

$$p(\phi, T) = \rho_p f_1(\phi) T, \tag{5.10}$$

$$\eta(\phi, T) = \rho_p d f_2(\phi) T^{1/2}, \tag{5.11}$$

$$\kappa(\phi, T) = \rho_p d f_3(\phi) T^{1/2}. \tag{5.12}$$

The dimensionless functions f_i are given in table 5.1. We note that the dissipation (which does not occur in classical studies of gases) is dependent on the inelasticity of the particles through the coefficient of restitution e. In practice, for dense assemblies of grains the tangential slip caused by relative spinning motion also dissipates energy, but the current theory neglects this.

These functions contain a dense gas correction in terms of the radial distribution function. We choose the form given by

$$g_0(\phi) = \left(1 - \frac{\phi}{\phi_m}\right)^{-\frac{5}{2}\phi_m}, \tag{5.13}$$

as in Lun & Savage (1986). This form is suitable for free-surface flows since the resulting equations have no singularity as $\phi \to 0$ (Forterre & Pouliquen, 2002).

$$
\begin{aligned}
f_1(\phi) &= \phi + 4e'\phi^2 g_0(\phi)\\
f_2(\phi) &= \frac{5\sqrt{\pi}}{96}\left[\frac{1}{e'(2-e')}\frac{1}{g_0(\phi)} + \frac{8}{5}\frac{3e'-1}{2-e'}\phi + \frac{64}{25}e'\left(\frac{3e'-2}{2-e'} + \frac{12}{\pi}\right)\phi^2 g_0(\phi)\right]\\
f_3(\phi) &= \frac{25\sqrt{\pi}}{16e'(41-33e')}\left[\frac{1}{g_0(\phi)} + \frac{12}{5}e'(1+e'(4e'-3))\phi\right.\\
&\qquad \left. + \frac{16}{25}e'^2\left(9e'(4e'-3) + \frac{4}{\pi}(41-33e')\right)\phi^2 g_0(\phi)\right]\\
f_5(\phi) &= (1-e^2)\frac{12}{\sqrt{\pi}}\phi^2 g_0(\phi)\\
f_6(\phi) &= \frac{\pi\sqrt{3}}{6\phi_m} g_0(\phi)\\
f_7(\phi) &= (1-e_w^2)\frac{3\sqrt{3}\pi}{12\phi_m}\phi g_0(\phi)
\end{aligned}
$$

Table 5.1: *Dimensionless constitutive functions $e' = \frac{1}{2}(1+e)$. The wall-particle restitution is given by e_w.*

With the assumptions made above, the stress tensor reduces to

$$
\boldsymbol{\sigma} = \begin{bmatrix} -p & \eta\dfrac{\partial u}{\partial y} & 0 \\ \eta\dfrac{\partial u}{\partial y} & -p & 0 \\ 0 & 0 & -p \end{bmatrix}. \tag{5.14}
$$

We further simplify the equations by using a depth-integrated approach. We do this by assuming that $T = T(y)$ and $\phi = \phi(y)$, and therefore there is no variation through the depth. The vertical momentum balance then yields a hydrostatic balance given by

$$
p = (h-z)\phi\rho_p g\cos\theta. \tag{5.15}
$$

We take the average value of the pressure to set the relationship between ϕ and T according to equation (5.10)

$$
\bar{p}(\phi, T) = \frac{h}{2}\phi\rho_p g\cos\theta = \rho_p f_1(\phi)T. \tag{5.16}
$$

The depth integrated y-momentum gives

$$\frac{h^2}{2}\phi\rho_p g\cos\theta = c_0 \tag{5.17}$$

across the chute. The x-momentum equation is slightly more complicated

$$0 = \rho_p g\phi\sin\theta h + h\left(\eta u'\right)' - \tau, \tag{5.18}$$

with the basal shear stress given by $\tau = \sigma_{xz}|_{z=0}$.

Finally, the last field equation is given by the temperature evolution, which simplifies to

$$0 = h\eta u'^2 + h\left(\kappa T'\right)' + q_b - h\gamma. \tag{5.19}$$

Here, we have defined the basal flux as $q_b = \boldsymbol{q}.\boldsymbol{e}_z|_{z=0}$.

The problem is closed by specifying the tractions and the heat flux at the walls and the basal surface. We do this by adopting the approach of Forterre & Pouliquen (2002) and imposing boundary conditions on the mean field. A more physically grounded approach such as that of Woodhouse *et al.* (2010) imposes boundary conditions using the surface roughness to quantify the parallel to normal momentum transfer. As we have seen this phenomenon on a smooth base, the complexity added by using this more rigorous physical argument is would not add to the understanding of the problem. As the boundaries are stationary, we define the properties in terms of the flow velocity at the wall:

$$\boldsymbol{t}\cdot\boldsymbol{\sigma}\cdot\boldsymbol{n} = \eta^\star(\phi, T)\left|u\right|, \tag{5.20}$$

$$\boldsymbol{q}\cdot\boldsymbol{n} = \boldsymbol{u}\cdot\boldsymbol{\sigma}\cdot\boldsymbol{n} - \gamma^\star(\phi, T). \tag{5.21}$$

The function $\eta^\star$ is given by

$$\eta^\star(\phi, T, \psi) = \psi\rho_p f_6(\phi)T^{1/2}. \tag{5.22}$$

This includes the factor ψ which is to be treated as a fit parameter. It is related to the rate of conversion of momentum from the wall-tangential to the wall-normal direction, and so larger values of ψ are to be expected for rougher walls. Forterre & Pouliquen (2002) gave typical values for this in the range 0.05–0.1. The boundary dissipation is given by

$$\gamma^\star(\phi, T, e_w) = \rho_p f_7(\phi, e_w) T^{3/2}, \tag{5.23}$$

and is a function of the coefficient of restitution between the particles and the wall.

Using these quantities we may write the basal stress and basal heat flux as

$$\tau = \sigma_{xz} = \eta^\star(\phi, T) u, \tag{5.24}$$

$$q_b = u\tau - \gamma^\star = u^2\eta^\star - \gamma^\star. \tag{5.25}$$

The walls are treated in the same way such that, at $y = 0$, the boundary conditions are

$$\eta u' = \eta^\star u, \tag{5.26}$$

$$-\kappa T' = u^2\eta^\star - \gamma^\star. \tag{5.27}$$

We exploit the symmetry of the flow to write the derivatives of u' and T' at the midpoint of the chute as 0

$$u' = 0, \tag{5.28}$$

$$T' = 0. \tag{5.29}$$

The final condition, which will be used to specify c_0, can take one of two forms. We can either choose to specify the total mass in the simulation as the flows are steady, or specify the mass flux. It was found that specifying the mass flux lead to a numerical instability where h increased without bound and ϕ decreased. We therefore specify the mass

$$m = \rho_p \int_0^w h\phi \, \mathrm{d}y. \tag{5.30}$$

We solve in terms of the non-dimensional quantities below

$$u = \sqrt{gd}\widetilde{u} \quad \ell = d\widetilde{\ell} \quad \boldsymbol{\sigma} = \rho_p g d \widetilde{\boldsymbol{\sigma}} \quad T = gd\widetilde{T}, \tag{5.31}$$

where ℓ is any length. For ease of notation, the tildes will be omitted from now on. Non-dimensionalizing in such a way as to keep all quantities of a similar order enables the solver to converge more rapidly. We use a three-point stencil to evaluate both first and second derivatives such that solutions are of order δy^2. If the grid resolution is N then we have a square algebraic system of $4N+1$ variables that can be solved using a non-linear matrix solve routine in MATLAB.

A sensible initial guess for the solution must be supplied to the solver if convergence is to be successful. Such an initial value can be formed by considering the effect of the sidewalls as a perturbation of the background flow. As such, we solve the above equations with $\partial_y = 0$ to obtain values for h, ϕ, T and u. Writing the total mass in the simulation as

$$m = \phi h N \frac{w}{Nd} = c\phi^{1/2} w, \tag{5.32}$$

we solve for the steady angle in terms of ϕ

$$\tan^2\theta = \frac{\psi f_6 \left[\frac{m}{w}(1-e^2)\frac{f_5}{\phi} + (1-e_w^2) f_7\right]}{f_1^2}. \tag{5.33}$$

Using this, we can calculate the steady states for different slope angles. An example of this can be seen in figure 5.3, which shows that two states can exist for a given pressure over a limited range of angles.

5.4 Data preparation

In order to extract the width of the dense core from the experimental data, we use a variety of image processing techniques. We have two edges that we need to detect: the position of the wall and the edge of the dense region. As the smooth basal surface is reflective, we can determine the low volume fraction areas of the flow by the increased intensity of the image in this region.

We detect the walls by averaging over all pictures at a given position on the chute and employing Sobel vertical-edge detection, which produces a binary image. This is usually ill-defined so we morphologically open the image with a large vertical line before closing it again with a small disk. This produces an area of the image that is a few pixels wide. Taking the horizontal average of the locations

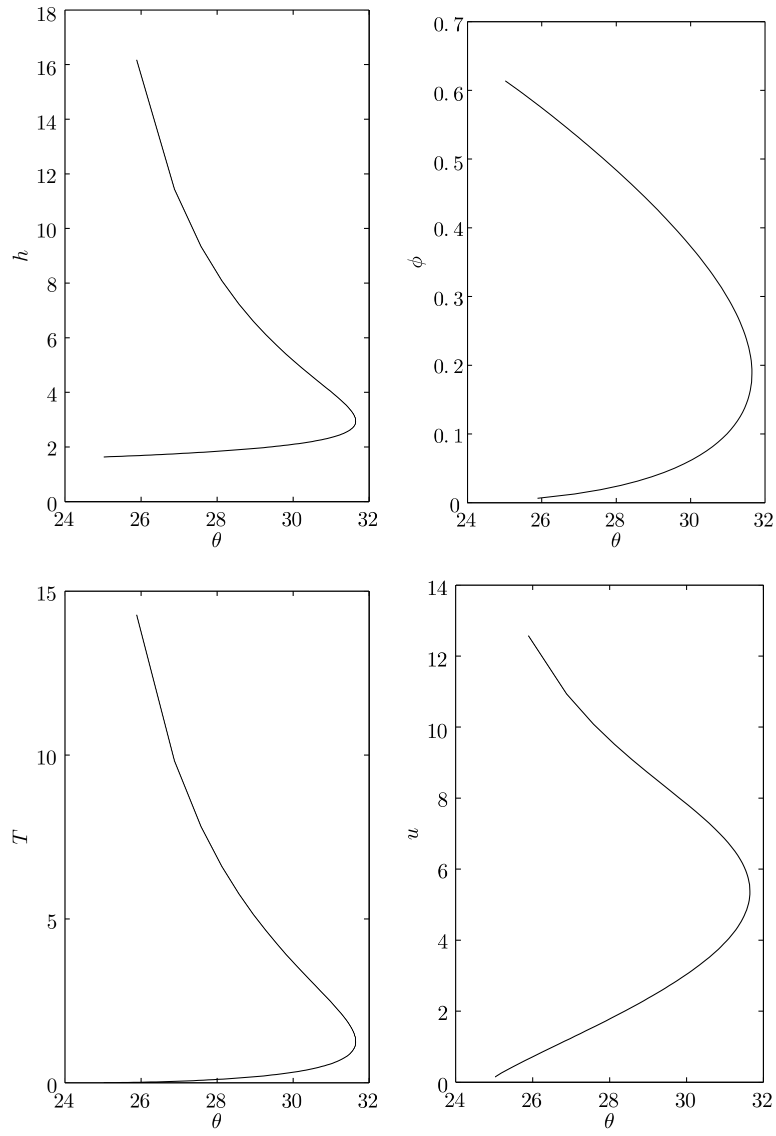

Figure 5.3: *Results for applying kinetic theory to a flow with no sidewalls (i.e. no lateral variation)* $e = 0.5$, $e_w = 0.5$, $\psi = 0.1$ *and* $c_0 = 1.28$

of this region gives the location of the wall very accurately. This can easily be verified by eye.

Detecting the edge of the dense region is somewhat trickier. There are a number of reasons for this. First, the edge is not well-defined as, in practice, there is a smooth transition in the volume fraction from the dense core to the sparse edge regions. We first take a time-averaged picture of the chute when the dense region occupies the entire width. Removing the remaining high-frequency noise from this image leaves an even illumination map that is devoid of any grain level fluctuations. We then take this illumination map and divide an average of pictures taken further down the slope by it. Dividing this averaged image with the illumination map clearly marks where the base can be seen through the particles. Normalising this essentially gives an averaged picture at a position down the slope with good contrast and a clear transition from the dense to the sparse region.

We then fit a regularised 2D step function with variable transition width to give a representative width of the dense area. If the x coordinate of the centre of the image is given by x_0 then we define the local coordinates in the image as $\xi = x - x_0$ and $\zeta = y$. We can then write the greyscale intensity of the image as $I = I(\xi, \zeta)$. Fitting the functional form

$$I = \frac{\alpha_2 - c}{2} \tanh\left(\frac{\zeta - (\beta_2 \xi + \gamma_2)}{\lambda_2}\right) - \frac{\alpha_1 - c}{2} \tanh\left(\frac{\zeta - (\beta_1 \xi + \gamma_1)}{\lambda_1}\right), \qquad (5.34)$$

allows us to extract the width of the flow. The fit parameters here are given by α_i, β_i, λ_i and c.

The width of the flow w at x is then given by $w(x) = (\beta_2 - \beta_1)(x - x_0) + (\gamma_2 - \gamma_1)$. However in figure 5.4 we plot the flow width averaged over the x-range of the image ($\sim 20\,\mathrm{cm}$ at a given position down the chute. Effectively giving $w(x_0) = \gamma_2 - \gamma_1$ for each x_0. This, as with our velocity data in previous chapters characterises the flow collapse over ~ 10 points down the slope.

5.5 Results

The evolution of the width of the dense region for flows that undergo inelastic collapse can be seen in figure 5.4. We see that the flow invariably starts attached

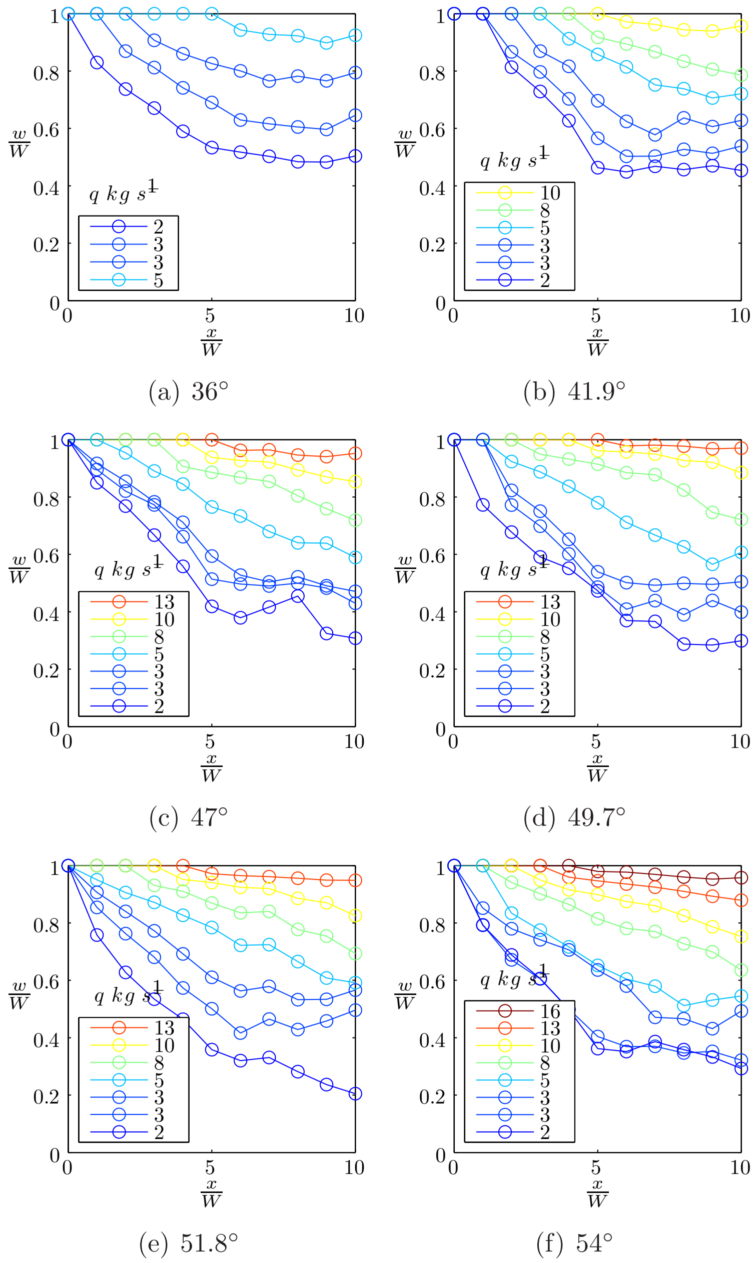

Figure 5.4: *The width of the flow w, normalised by the chute width W as the flow progresses down the slope for various inclinations and mass fluxes on the smooth base.*

to the walls and detaches once the shear at the wall is sufficiently strong. The width of the high density region appears to tend to a limit.

The numerical solution to the equations are defined by three control parameters. For a fixed inclination, these parameters are the total mass hold up m, the momentum transfer coefficient ψ and the particle–wall restitution coefficient e_w. The ability of the solver to find a solution was very sensitive to the initial guess. The procedure outlined above produced valid solutions for most masses, but the solver did not find a solution for low mass holdups i.e. there was a minimum m below which no solutions could be found.

Choosing an appropriate combination of ψ and e_w that makes the wall a heatsink produced continuous, smooth solutions that converged rapidly. However, these predicted a dense region at the walls and a sparse region in the centre of the chute — the opposite of what we have observed experimentally. Choosing a combination of ψ and e_w such that the walls have a net flux of heat away from the boundary (as in our experiments) produced solutions with a numerical boundary layer. This was fixed at 3 points for all resolutions, the same size as our stencil. A boundary value solver was also tried with similar results. This grid dependence means that our simple model does not capture the essential properties of our experiments.

We have also observed this phenomenon of a dilute region appearing at a boundary at the basal surface. On a rough base, this manifests itself at high inclinations ($> 46°$) and the effect can be seen through the total friction μ. When the separation occurs, μ is relatively small when compared with lower inclinations (see figure 5.7), and also becomes independent of the Froude number and the mass flux.

The thickness and character of this basal layer is governed by a complicated dependence on other flow parameters. DEM simulations of flows allowed to reach equilibrium show that the nature of the basal layer depends strongly on the inclination. Figure 5.6 shows the results of time-steady flows containing different sized particles, one large, one small and an equal mixture of the two by volume (The ratio of the diameters being 1.5). The vertical density profile is well-fitted

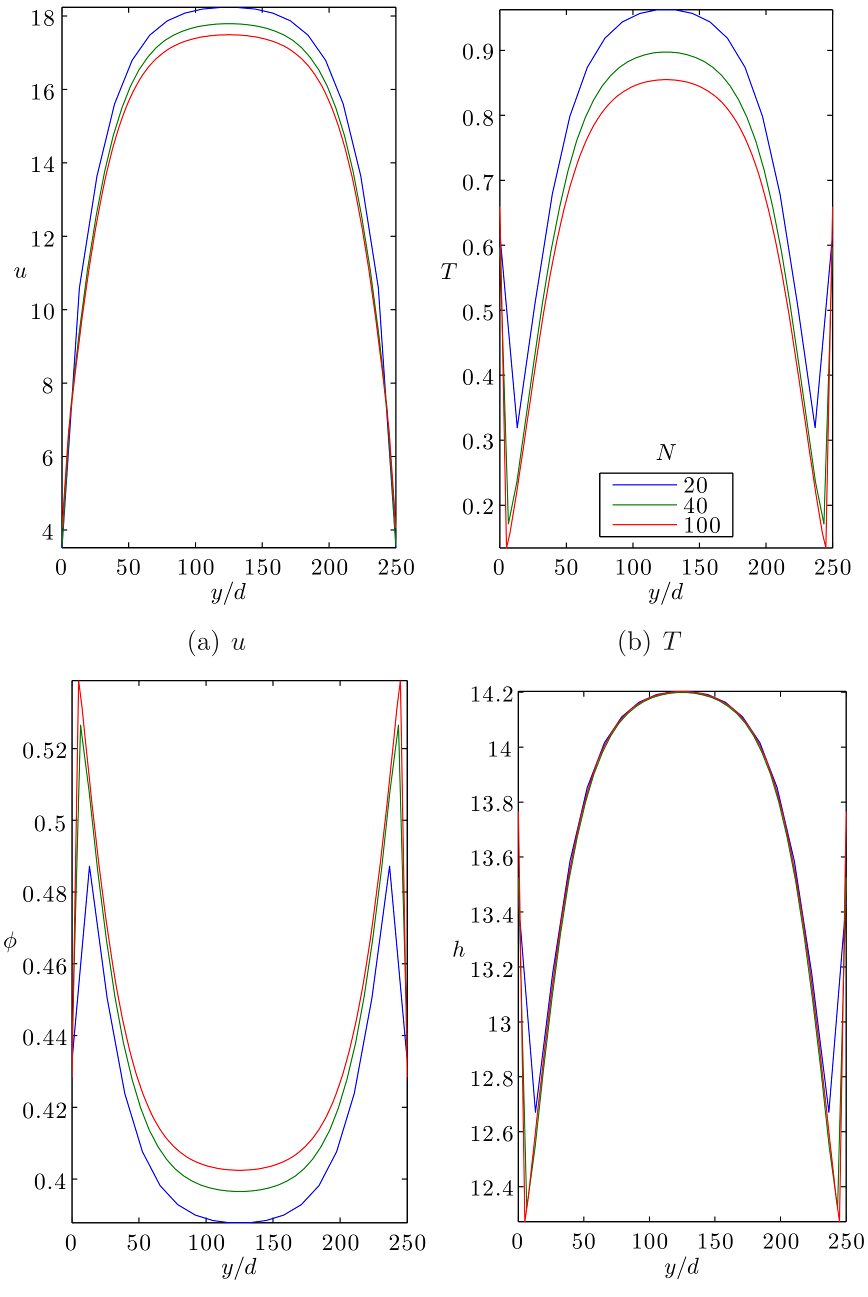

(a) u

(b) T

(c) ϕ

(d) h

Figure 5.5: *Results of computation for inelastic collapse using kinetic theory. The parameters used are* $m = 1500$, $e = e_w = 0.6$, $\theta = 25°$, $\psi = 0.05$. *The solution is to machine precision, but the discontinuity of the gradient suggests that the solver has not found a valid solution. The location of the discontinuity is dependent on the resolution.*

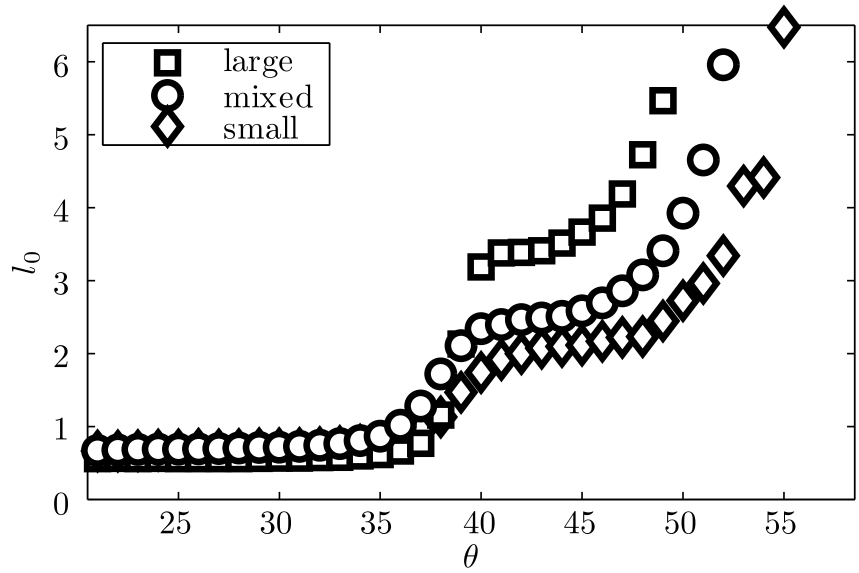

Figure 5.6: *Height of the low density layer at the basal surface in DEM simulations allowed to reach a fully developed state. Small particles have $d = 4/5$, large particles have $d = 6/5$, mixed consists of an equal volume of each particle type. Reproduced from Holyoake & McElwaine (2011).*

by the regularised step function

$$\phi(z) = \frac{1}{2}\left[\tanh\left(\frac{z - z_0}{l_0}\right) - \tanh\left(\frac{z - z_1}{l_1}\right)\right],$$

which gives regions of approximately constant volume fraction. At the base, a low density shear layer of thickness l_0 supports a high density passive overburden. For all particle species, the thickness was shown to be monotonically increasing with the slope angle. There are two transition points that can be seen, one where the layer first separates from the base, and a second one above which the height of the layer increases rapidly with the inclination until the entire flow becomes diffuse and kinetic. This density inversion phenomenon and the velocity independence of the friction coefficient have also been reported experimentally in Taberlet *et al.* (2007). However, in contrast to Taberlet *et al.* (2007), such flows were seen for high inclinations, far above θ_2, indicating that a much larger energy input is needed for our material to maintain a supported state, possibly due to the increased rolling resistance and therefore the increased dissipation caused by

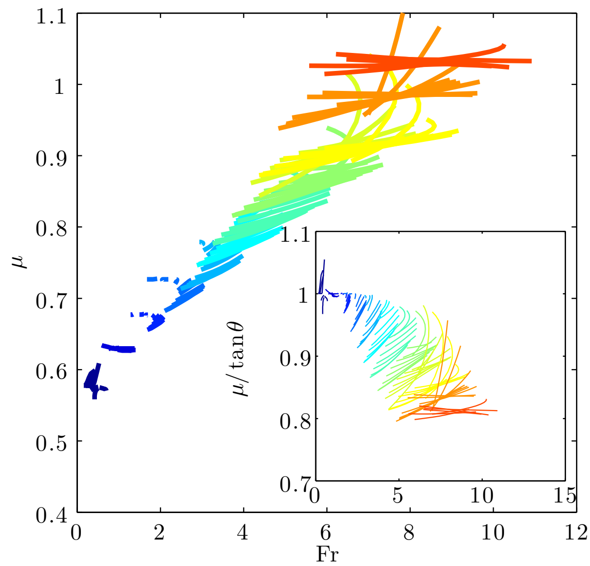

Figure 5.7: *μ_t as a function of* Fr*. Coloured by inclination. The constant friction at high inclinations is in agreement with numerical simulations of Taberlet* et al. *(2007) for a flow supported on a highly agitated, sparse, basal layer.*

the irregularity of our particles' shape.

For our steepest flows on the rough base, as seen in figure 5.7, the friction is constant. This is in agreement with the numerical simulations of Taberlet *et al.* (2007) who identify that the basal layer gives a constant effective basal friction which is independent of velocity. For sufficiently high inclinations and low mass fluxes the agitation of the grains by the surfaces is large enough for the entire flow to be in the dilute regime (see figure 4.1). These very energetic flows over the rough base ($\theta > 52°$, $q \lesssim 2\,\mathrm{kg\,s^{-1}}$) have been excluded from all of the analysis in this thesis as the saltating particles form an ill-defined surface, and hence neither height or velocity data are available.

5.6 Conclusion

In this chapter we have looked at a phenomenon whereby the flow of a granular material undergoes a collapse with a dense central region appearing, flanked by two low density regions. The experimental data suggest that the width of the dense region of the flow tends to a limit as the particles progress down the slope.

We attempt to model this phenomenon using a simplification of the granular kinetic theory of Lun *et al.* (1984). We model the interaction with the walls as a heat flux generated by the slip velocity, modelled as a Fourier heat conduction law. However, the appearance of a numerical boundary layer, the discontinuity of the gradients, and the grid dependence of the solution suggest that our model is ill-posed. The drastic assumptions of constant velocity, density and temperature profiles through the depth may be the culprit. A fuller model based on the kinetic theory equations that do a true depth-averaging, or a two-dimensional calculation, may be more successful in capturing the behaviour.

We see a similar effect at the basal surface where the flow is supported on a highly agitated basal layer. This is also seen in DEM simulations. These flows exhibit a constant friction coefficient which is much higher than the maximum friction calculated using h_{stop} experiments. This could have important consequences when modelling avalanche run-out.

6

Conclusions and Extensions

The aim of this thesis has been to study rapid granular flows in an inclined chute. We have reviewed a frictional model that has given good agreement for equilibrium flows where the inclination is no higher than $\theta_2 = \tan^{-1} \mu_2$. Typically such flows have inertial number $I < 0.5$ (MiDi, 2004). We have investigated flows on much higher angles whilst remaining in the dense regime.

Dense chute flows that take a long distance to relax to equilibrium present an experimental difficulty in that, if the evolution is to be tracked, then measurements must be made either at multiple times or at multiple points down the slope. We have used a recirculation mechanism to sustain flows indefinitely. These are time-steady and therefore allow us to make multiple measurements of the flow using one set of equipment and enabling us to track the evolution. Our key finding is that the flows exhibit a much larger value of the total friction than previously observed. This makes it incompatible with theories such as the $\mu(I)$ rheology, as the comparison between a numerical solution and our experimental data shows.

Further to this, extrapolation of the data on the rough base suggests that steady flows are possible with $\theta > \theta_2$. This is a strong prediction to be tested in the future on different apparatus. For inclinations slightly bigger than θ_2, we do see steady states. This is possibly due to the effect of wall friction. However, it seems unlikely that wall friction can account for the much larger total friction at higher angles. We have found good collapse for the data by considering the effect of the dimensionless height on the scaling, however, it is not clear how this relates to the structure of the local rheology, or indeed if a local rheology is appropriate for such flows.

On the smooth base, the flows are well modelled by a constant value for the total friction. Although some dependence on the Froude number is exhibited, it is complicated and small compared to the absolute value of the friction.

We have developed a finite volume code for solving the $\mu(I)$ rheology. A number of different numerical techniques were used to try and solve the problem, but unfortunately the equations were unstable for higher order schemes.

We have also observed a number of interesting instabilities including roll waves and longitudinal vortices. However, over the region of the phase space covered in our experiments, the most prolific was the lateral inelastic collapse instability, which appears to be the result of a net heat flux from the walls into the flow. We have attempted to investigate this numerically using a simplified, one dimensional adaptation of the granular kinetic theory, but this was susceptible to numerical problems at the boundaries and no physical solution was found.

For the flows on inclinations at the steepest limit (55°), we found that for the lowest mass fluxes both bases exhibited a fully dilute, collisional regime. Regrettably, no experimental data was extractable from these experiments as the height is ill defined which also meant that velocities were not extractable from the data using our measurement systems.

There are a number of key issues raised by the investigations presented here which, if addressed, would contribute significantly to the understanding of granular materials.

The important issues regarding the high value of the maximum friction coefficient are the following:

- Is there an upper limit of μ_t for a high speed granular material and if so, what is it?
- What is the physical mechanism that gives such high effective friction?

- What is the function dependence of μ on I for large I and what is the correct way to incorporate h, θ and other system variables?

The difference in shape of the velocity profile over the rough and smooth bases also remains undescribed. It is not clear why changing the basal condition effects a change in the lateral velocity profile when the wall conditions are kept the same. It is possible that a non-local rheology such as that proposed by Pouliquen & Forterre (2009) is needed to account for the wall effect in the interior of the flow.

Lastly, the phenomenon of the inelastic collapse should help to characterise the role of boundaries in a granular flow. It is surprising to see that, even with smooth walls and base, a large heat flux into the interior appears, causing the flow to become dilute. This phenomenon almost certainly changes the interaction of the fluid with the walls, which would result in a different value of the measured total friction. It is not clear if this effect could be accounted for by a modification to a frictional rheology or not.

It is hoped that the substantial body of software that has been written to calibrate the measurement systems and automate the process of data collection will be used in further investigations of granular flows in the chute. For this reason, a limited overview has been included in the appendices.

In all, we hope that this dissertation has posed some interesting questions for the field of rapid granular flows and that it may go some way towards contribruting to a fuller description of them.

Appendix

A

Operative Guide

Introduction

In this appendix we give an overview of the steps needed to collect and process data using the measurement systems described in chapter 3. The software is written primarily in MATLAB, but we also process some data using Digiflow, DAMTP's in-house data acquisition software.

This guide gives an approximately chronological order for setting up and calibrating the systems, and afterwards collecting and processing the data.

This appendix only documents the top level commands needed to get useful data from the chute. It is hoped that the comments in the lower level functions and their context within the high-level functions should be enough to explain their purpose.

Equipment Needed

Video System

PC Hardware

The video system has a number of separate subsystems. The PC responsible for collecting the video should be equipped with a BitFlow data acquisition card with a daughter board. The daughter board is responsible for generating the flash pulses.

It is recommended to have a computer upstairs for data collection, and another computer downstairs with a remote desktop capability. This is necessary so that, after altering the position of the traverse, it is not necessary to go upstairs to restart the data collection process.

Camera and traverse

The camera used is a JAI-CL M4+, which will need to be correctly set up both within DigiFlow and the SysReg utility, which is usually found on the Desktop. This should be mounted approximately 70 cm above the chute base so that a 25 mm lens will capture the entire width of the chute. The f-stop should be set to around 5.6, which provides a good range of contrast.

Illumination system

The illumination system consists of four banks of LEDs. Each bank is connected to its own amplifier. These should be powered by a bench power supply capable of supplying 20 V at around 2 A.

The daughter board in the PC should be connected to a separate circuit board or *splitter* which serves to divide the signal to each amplifier.

In order to achieve an even illumination across the field of view of the camera, it should be noted that there is a jumper on each amplifier that changes the mode from signal switching to permanently on.

Laser triangulator

The laser triangulator head should be attached to the milled aluminium attachment that sits in the groove of the material used to fabricate the traverse chassis. The control box should be attached somewhere securely where there is no risk of the cables getting caught and pulling it to the ground.

To record the illumination pulses in the height profiles, the synchron socket on the back of the control box must be connected to the illumination system. This requires another circuit board, which is powered using a dedicated 3.3 V power supply. This is connected to the synchron socket and also to the splitter.

The triangulator should be connected to a separate PC as per figure 3.7. It should be checked before starting that the triangulator can record valid data from the basal surface up to the highest flows that will be observed.

Optionally, an LED connected to the PC's serial port can be connected to alert the user when the triangulator has stopped collecting data. This can speed up the collection process when conducting a large number of experiments consecutively.

Loom

This should contain the four LED cables, a power supply for the camera, the camera data lead and the laser triangulator data lead. These should be connected securely such that, as the traverse moves the length of the chute, it will not get caught on the scaffolding. If it gets caught, it is surprisingly hard to spot when performing an experiment.

Video and height calibration equipment

In order to calibrate the PIV system and remove parallax effects, a stiff, thin board must be overlaid with a chequerboard pattern. This must be sufficiently large to cover the portion of the chute that is visible by the camera. The board must also be sufficiently large so as to intercept the laser sheet from the triangulator. In this portion it is recommended to use plain paper of a similar brightness to the sand. The plain paper will help to give a more reliable mean height from the triangulation measurements.

In addition to this, a number of boards of different thicknesses are needed to place under the patterned board to alter the distance between the camera and the calibration pattern.

Weight calibration

This requires a nylon bag with a snoot which should be able to be tied off. If calibrating with the chute at high inclinations $> 45°$, then this should also have a scaffold chassis to prevent the bag from sagging. The bag should be connected to the crane scale and crane using a nylon harness. To control the position of a bag, a rope should be attached to the railings and the bag. Preferably, the rope should not be made of natural fibre, as this will erode and eventually snap.

It may also be necessary for a second rope to keep the bag in a suitable lateral position as the crane cannot go sufficiently far in the y direction.

The existing weight calibration can be read using the function `deg2kg` which takes the aperture size in degrees and converts it to an equivalent mass flux.

Notes before starting

In this section we describe the necessary software infrastructure used to store the data. This will be referred to throughout this manual.

The MATLAB code makes heavy use of two shell variables. These can be defined in your `.bashrc`, so that they are accessible to other programs other than MATLAB. They are

- `DIRDATA`: for processed data,
- `DIRDATARAW`: for raw data.

Each task has a directory contained within one of these two variables, i.e. the video raw data is kept in `DIRDATARAW/video` and the velocity is contained within `DIRDATA/velocity`.

Every file obeys a fixed naming convention:
`prefix-year-month-day-number{-subnumber}-suffix{-filenumber}{.fileextension}`
where the prefix is usually given by the experiment. In our case, we take the prefix as `rchute`. The suffix describes the type of data contained within, i.e. video,

velocity, height etc. Some examples are:

- `rchute-2008-07-31-06-video`
- `rchute-2008-08-02-01-01-video-0092.png`
- `rchute-2008-08-02-01-01-video.png`

where `subnumber`, `filenumber` and `fileextension` are optional parameters. Note that `filenumber` requires a `fileextension`.

When coding in MATLAB, the various parts of the file names can be separated and reassembled using the functions `exp_file_separate.m` and `exp_file_construct.m`.

Throughout the software, dates are of the form `yyyy-mm-dd` and times of the form `hh:mm:ss`.

It is also recommended to transfer software from the laboratory computer system to the DAMTP unix system using rsync, which helps to ensure no data is lost and keeps data transfer times to a minimum. To use this, `putty` key exchange must be set up.

Lastly, it is recommended that the MATLAB and Digiflow code is stored in a versioning repository. Any changes to the Laser triangulator or `weigher` software should also be committed to the repository.

Data is collected at 25 cm intervals from the bottom of the chute. We also record data at a point 266 cm from the bottom of the chute which is the upper limit of the travel of the traverse. If any data is collected at other points, the software will interpolate any calibration data as suitable.

The *lab side* of the chute is the side that is nearest to the centre of the AFF which the wall side is the opposite side.

Each basal surface has a code. The smooth base is enumerated as 0 and the rough base is enumerated as 1. Extra surfaces can be added in `surftype.m`.

Starting and stopping the chute

To start the recirculation mechanism, the large main power switch on the left must be turned on. Next, the ventilation system must be initiated by pressing the green button near the large ventilation units. Then, the power switch on the main panel may be turned on. At this point, it should be ensured that the 0 value of rotary encoder corresponds to a fully closed aperture in the hopper.

This needs to be done each time as the rotary encoder does not record changes in the aperture size when the power is off. Then, the red button can be pressed to initiate the bucket conveyor and initialize the screw feed. The screw feed rate can be changed using the blue and yellow push buttons.

To set up a steady flow, select the aperture size and wait until sand enters the overflow. At this point, the amount of sand in the hopper remains constant and the flow should have reached a steady state. If the sand backs up into the overflow from the collection hopper, the rate of the screw feed needs to be reduced to prevent backfilling into the bucket conveyor system.

To stop the system, reduce the rate of the screw feed until it has stopped and then turn off the bucket conveyor as the mass flux in the chute reduces to 0. Allow the ventilation system to run until no more sand is flowing.

If, for any reason, there is a risk of the sand backing up into the bucket conveyor, shut off the screw feed at the earliest opportunity. If it can be avoided, do not press the red emergency shut off buttons as turning the bucket conveyor on when it is full stresses the motor and will cause damage.

Calibration Routines and Software

Before any data is collected the systems must be calibrated. It is important to do this before data is collected as the software will automatically choose the last set of calibration data that was measured before the data is collected.

Mass flux calibration

As the particles degrade, it will be necessary to periodically check if the mass flux varies. The bag, crane, crane scale and two restraining ropes will need to be set up as described in the previous section. The crane scale needs to be connected to a computer via a USB-RS232 converter so that data may be collected. The `weigher` software in the SVN repository will need to be installed before progressing.

To begin, the bag will need to be hanged from the crane scale using a nylon sling. One rope must be tied to the hand rails on the balcony to bring the bag slightly closer to the wall side so that it is central to the chute and all of the material is captured. The second restraining rope is used to bring the bag away from the chute exit while a steady flow is set up. The snoot at the base of the bag must be tied up securely at this point.

Once the flow has reached a steady state, make sure that the `weigher` program is running and release the knot on the restraining rope to allow the bag to swing under the end of the chute. When the mass on the crane scale reaches around 200 kg, release the knot restraining the snoot of the bag otherwise sand will pour onto the lab floor. Stop the `weigher` program and repeat as necessary.

Copy the files produced by this procedure to the `weigh` subfolder of the raw data directory. These may be read using the `wg_read_wgh01` MATLAB script.

Height calibration

As the height information is used in the video calibration, the height systems must be calibrated first. All data recorded for this should be put into the `DIRDATARAW/calib_height` directory.

First, the curvature of the chute must be recorded. This is done by recording height data using the software described in appendix C at the usual data collection points. It is recommended to record for a number of seconds to eliminate noise, and the resolution is not important. For the smooth base, the `method` in the file name should be `initial`, and for the rough base `initial-1`. In general, each base should have a set of `initial-n` files where `n` corresponds to the surface's enumeration.

Once the heights have been recorded and copied to the DAMTP filesystem, `calib_make_height` will produce a `mat` file in `DIRDATA/calib_height` with the important information.

Parallax calibration

We calibrate the video camera to remove parallax effects from the velocity calculation. Both the raw data and processed data are in subdirectories called `calibration`. This requires the chequerboard pattern board and the boards of varying thickness described above. Here, we record a picture of the calibration pattern at different heights. It should be ensured that the lab side of the chute should have complete squares — the chute is slightly less than 250 mm and so the squares on the wall side of the chute will be incomplete. The calibration pattern uses 25 mm squares, the postscript file for which can be found in the MATLAB software.

In digiflow, the `single_shots` program should be run whilst also running the laser triangulation software on the other PC. Digiflow will ask for the surface type, which should be an integer as described above and for the height that the chequerboard is currently at. This can be taken from the laser software screen directly, rather than recording a processing the file. Digiflow will automatically produce `bmp` files in the `calibration` directory in the relevant `users` directory on the `v:` drive.

Measurements should be taken at around 5–10 different heights. Once the data has been uploaded into the `calibration` subdirectory, the MATLAB program `calib_video_make` can be run to process the data into a usable calibration map. It is necessary to have the camera calibration toolbox from Caltech installed. (See `http://www.vision.caltech.edu/bouguetj/calib_doc/`)

The software will extract the corners of the squares and produce a `mat` file with the relevant calibration data in it.

Both height and video calibration data can be processed by running `calib_make` in MATLAB.

Video calibration

Video is recorded using the Digiflow macro `Capture_to_dfm`, which is the quickest way of writing the video data to disk. It must be checked what length of time the flash length set in the call to `camera_set_frame_straddle` corresponds to. This is done by using a photo transistor and oscilloscope to check the interval and flash length. This should then be used to calculate the velocity.

Once this calibration is done the user can begin to gather data.

Maintenance

The user should record the time that the chute was turned on and off, as this is used to track particle degradation and for general maintenance purposes.

When operating the chute, the user must be aware of a number of issues. The ventilation system must be checked periodically to see if the bags of dust are full. This should be done every 20 hours of experiment time.

There are a number of perishable elements of the recirculation mechanism. Perhaps the most important is the bucket conveyor belt. Large pieces of black rubber found in the sand should be taken to the technicians. If the occurrence of the rubber increases, the belt may need to be replaced.

There are also seals on the rotating parts of the chute that degrade after extended use of the chute. If dust is escaping, they will need to be replaced.

Data collection

Here we describe the typical routine followed when conducting an experiment. First, a steady flow should be set up. Then, the software controlling the laser scanner should be started with the `automatic` option set to 1, the `prefix` set to rchute and the `suffix` option set to height. Values for other options can be set according to the user's needs. The triangulator software will then wait for the PIV pulses to arrive and then start to record.

Then, the `capture_to_dfm` should be run within Digiflow through a remote desktop connection. This will then ask for details about the flow that is running. A sub-experiment is taken to mean an experiment at a different position on the chute, and an experiment corresponds to a mass flux / inclination combination and the files are named accordingly.

When Digiflow asks *Another subexperiment?*, if the user clicks yes, then the traverse should be moved to the next position. When the user is ready, the new x position should be entered and recording will start again. The laser scanner software will increment the sub-experiment number of the file automatically.

When a new experiment (i.e. the flow rate or inclination) changes, the laser software must be exited using `Ctrl-C`, and the experiment number changed manually (most convenient is using the `-en` switch on the command line). Digiflow will increment the experiment number if the user selects `yes` when prompted with `nNew experiment?`.

Once the experiment is complete, `dfm_png` in Digiflow should be run to convert the `dfm` files to `png`, a file that MATLAB is able to read. At this point, both the height data and the `png` files should be backed up to the DAMTP system with an appropriate rsync command.

The `png` files have the suffix `video` and are stored in the `video` subdirectory of the raw data directory.

PIV

A Digiflow macro, `auto_piv` has been written. It automatically looks for experiments in the `v:\user\NAME\video` directory that have not been processed into velocity data in `v:\user\NAME\velocity`. This can be run overnight with no user input. Again, when this has finished, the files should be copied to the DAMTP system in `DIRDATA/velocity`.

Velocity `dfi` files have the suffix `velocity` and can be read with the MATLAB script `df_dfi_read`.

Data consolidation

Once the height and velocity data have been copied to the DAMTP system, running `make_experiment` allows the user to select which experiments to process. This procedure collects the velocity data, transforms them according to the appropriate video calibration data and transforms the heights according the appropriate height calibration data. Instructions for recovering the data with the calibration applied to it can be found in this routine. After running `make_experiment`, the function `update_files` must be run to update the experiment database and the `experiment_all_average.mat` file.

The resultant data structure is written as a `mat` file to the `DIRDATA/experiment` directory. This can be loaded by providing the date and experiment number to the `load_experiment` function.

Data manipulation functions

A number of useful manipulation functions have also been written. The most pertinent ones are listed below.

`experiment_average_all` Averages all available experiments, performs an average and writes it to `expeiment_all_average.mat`. This is intended for quick and easy manipulation of the whole, averaged dataset. The file can be loaded by running `experiment_load_all`.

`experiment_average` Takes the struct in the `experiment` files and averages over time and space for the height and velocity data. Horizontal, vertical and temporal averaging dependent on the arguments.

`dfi_do_all` Takes a `dfi` file and transforms the velocity using the date in the file name to load the calibration data.

`experiment_category` Lists the user-supplied category for the experiment

`experiment_info` The information for a given experiment

`experiment_plot` Plots salient information for a given experiment. Takes a while to process.

`exp_hash` Collates all experiment information into a single file and prints it.

`plot_phase_space_covered` Plots the area of the phase space covered by the current experiments

B

Crane Scale Software

In this appendix we discuss the software written for the mass flux calibration routine in section 3.2.3 on page 59.

In order to calibrate the hopper aperture size with the mass flux, it was necessary to measure the mass captured in a bag over a period of time. The derivative of the mass-time curve then gives the mass flux. The first studies carried out on the chute by an undergraduate student suggested that the flow out of the hopper could be in one of many states for a given aperture size with variations of as much as 10% — a calibration curve for the hopper looked to be out of the question. However, measurements for flows at a fixed aperture size seemed not to indicate a large variability in the velocity or height. Visibly, the change in volume fraction could not account for the supposed variability in the mass flux, so the method of data acquisition was studied more closely.

In order to measure the mass flux an industrial crane scale supplied by Straightpoint (UK) capable of measuring up to 500 kg in 0.1 kg intervals through an RS232 interface. The software supplied with crane scale claimed to be capable of supplying a measurement frequency of 10 Hz. However, as the software designer decided to dump the measurement value in the cell of a spreadsheet of fixed name with a given date format, it was not only inconvenient to collect large amounts of data, the time at which the data arrived to the computer was only given to the nearest second.

The maximum mass flux that we recorded on the chute was in the region of $22\,\mathrm{kg\,s^{-1}}$. As the capacity of the bag was around 250 kg, this meant that the error induced by the finite sampling time alone was accounting for 9% variation in the readings, and so it was clearly necessary to develop software with an increased level of granularity.

The manufacturer and the supplier of the equipment refused to supply us with source code or alternative software without charging a significant amount, and so we decided to reverse engineer the protocol.

Initial investigations using a serial port traffic sniffer suggested that the crane scale was reading data at over 10 Hz, and that it was solely the software that was losing information. Indeed, researching the ATMega CPU and the strain gauge within the unit suggested that data rates this high were more than possible.

Some limited information was found regarding the basics of the closed-source protocol regarding the hand shake, but the codes to request the data were not available as they were probably specific to the manufacturer. After much decoding and with some luck, it was determined that the DWORDs

```
0xfe,0x01,0x8f,0x08,0x0e
```

to the serial port elicited an 11 byte response including a start, stop and parity bit.

Upon reversing the byte order and the endianness, a single precision number was produced which gives the weight on the stress gauge measured in tonnes. This was written to a file along with the time to the nearest millisecond.

File naming and general handling routines were also included to make data collection easier.

As a result of this reverse engineering, the error in the measurement between flows was less than 2%.

Description	File parameter	Switch	Default Value
COM Port	comport:	-cp	COM1
Name	name:	-nm	rchute
Suffix	suffix:	-sf	weigh
Series number	seriesnumber:	-sn	Auto
Number	experimentnumber:	-en	Auto

Table B.1: *Table of parameters for `weigher.exe`.*

Code Operation

A copy of the software can be found in the rchute SVN repository, and is entitled simply `weigher`.

The options in table B.1 can be supplied either on the command line or using a file called `settings.txt` stored in the current directory.

Series and experiment numbers are automatically incremented depending on the existing files in the current directory.

File Format

The file names have a format of

`name-date-series-seriesno-experimentno-suffix.wgh01`.

The content of the file is simply a series of pairs of `double` data types. The first of each pair gives the weight in kilograms and the second the time at which it was received.

These files can be read by `wg_read_wgh01.m`, and various utilities can be found in the `weigh` directory of the MATLAB chute software.

C

Laser Triangulation Software

This appendix is primarily intended as a technical reference for future users of the Micro-Epsilon laser triangulator that has been used to record the height data for the experiments in this thesis. The work described here constitutes a considerable part of the effort that went into producing this thesis, and so it has been included here. The existing documentation for the API which was supplied with the equipment is incredibly sparse and written in very poor English. We hope that this appendix will give some pointers on how the API has been used.

Since its inception, the software has been used frequently in the laboratory at DAMTP. Over the previous $2-3$ years, the software and the associated MATLAB utilities have been used by at least two Ph.D. students, two postdoctoral research associates and a number of undergraduates as part of summer research projects.

Motivation

The laser triangulator is a high bandwidth device capable of reading 256,000 points of data per second at double precision sustainably. However, the software supplied with it was not capable of operating the device at full capacity. The choice of data storage was to output each profile (up to 1000 points) in a separate Excel spreadsheet and, as a result, the data could not be written to the hard drive at the designed speed. It was also very cumbersome for processing data. Along with this, there was no facility to automatically rename files if a file of the same name already existed, which made the probability of data loss high and the process of running experiments consecutively without wasting time very difficult. This was a particularly important problem when working with the recirculating chute, as the particles degraded the longer the machine was kept on. Finally, the existing software was not capable of counting pulses from an external source, a feature which was needed for the synchronization with the video used for the particle velocities.

All these problems made it evident that custom software was required in order to make time critical experiments possible

Implementation

In order to ensure that the maximum bandwidth of the sensor was used, we chose to transmit the data in *container mode*, which is an asynchronous method of data transfer. A container is a data structure which contains multiple profiles. The scanner waits until the container is full and then transfers the whole container to the PC. As latency is introduced for each chunk of data being transferred, and the amount of latency is essentially fixed and not dependent on the size of the container, transferring larger blocks of data at a time keeps latency to a minimum. For example, if the laser is recording 1000 profiles per second and a container contains 1024 profiles, approximately 1 container will be received per second, and the latency of $\approx 5\,\mathrm{ms}$ will only be incurred every time a container arrives, thus reducing the response time by a factor of 1000 for the 1000 profiles transferred. We choose the number of containers, or the *container height*, such that the 128 MB buffer inside the scanner is as full as possible. In practice, maximum transfer rates can be achieved with a much smaller height.

The code is written in `C++` and is event driven. Loosely, we set a call back function (`NewContainer`) that is executed when the container arrives. This strips out the redundant data from the profiles and writes it to disk. The computer then waits until an event is set. We set the event when the required number of profiles have been received, or when the user presses `Ctrl-C`.

The set up of the laser scanner is done by writing a hex code to the profile rearrangement register (using the `SetFeature` function). The hexadecimal code is generated from the input arguments supplied by the user, which are discussed in the next section.

File Format

The output file format is subject to the naming convention given in appendix A. The file extension is `.lt03`, which is also contained within the header and can be read by the MATLAB function `ls_read` (which also reads older `lt01` and `lt02` files) or `ls_read_lt03`. The file handling utilities within the program automatically look for files with the current date in the name. The program increments the experiment number by one, until it finds a number for which there is no file of that name. In this way, no data will be re-written unless the user explicitly deletes the file first.

The header takes the following format

Name	Type	Size
File type	char	4
Averaged data	char	4
Note Size	int	1
Note	char	Note Size
Header size	int	1
Rate	int	1
Resolution	int	1
Shutter time	int	1
Idle time	int	1
Measuring Area	int	1

One field of note is the averaged data field which specifies whether the profile data have been written straight to the file or averaged first.

For non-averaged files the data are written as 16-bit integers. If we define the resolution (i.e. the number of data points) of the profile as r, then each profile contains $3r$ such integers. The first r integers contain the integer height data z_i, and can be converted to the real height data z in millimeters by

$$z = 0.005(z_i - 32768) + 250. \tag{C.1}$$

The next r integers give the x data, which can similarly be written as

$$x = 0.005(x_i - 32768). \tag{C.2}$$

The last 8 integers in the profile contain time stamp information. The function for extracting this information can be found in `ls_read`.

For averaged files, the scheme is slightly different. The position data is written as single precision floats (only the z coordinate) and the time information is extracted in the same way as before.

Modes of operation

Automation

There are three modes which control the time for which profiles are collected. They are controlled by the `-am` command switch or the `automatic:` option in the settings file.

```
automatic:  0
```

This value of the automatic parameter starts recording as soon as the program is executed and stops after (approximately) the number of profiles that the user has requested, using the `numberofprofiles:` or `-np` options. A value of 0 for the number of profiles will record until the user aborts the program.

`automatic: 1`

This mode considers externally generated pulses that are inputted using the synchron port on the laser scanner. The program waits until incoming pulses are received and then starts recording. When the pulses stop, the program keeps on recording until the number of seconds specified in the autosecs options `autosecs:` or `-aus` has expired. The program then increments the file name and starts recording in the new file when the pulses restart. Note: if pulses occur as the program is waiting for the autosecs interval to expire, then the data will be recorded until no more pulses are recieved and the interval counter will start again from 0, i.e. autosecs seconds must expire with no pulses in order for a new file to be opened.

This mode is recommended for collecting multiple sets of data when using the PIV system.

`automatic: 2`

A value of 2 for the automatic parameter simply records for the duration that the pulses exist, and exits when they have stopped.

Other Switches

Averaged mode

If the option `average:` or `-ap` is set then only the averaged data is written to the file. By default, all of the data is written. The points between `averagestart:` (`-as`) and `averageend:` (`-ae`) are included in the average. If the average of the whole profile is desired, then these can both be set to -1.

Shutter times

There are two options that control the exposure of the sensor. The exposure that gives the best result depends on the material and the lighting conditions. The program displays the percentage of valid points that it can see as it runs, and so the user should adjust the parameters accordingly. The first parameter is the `shutterauto:` (`-sa`). If this is set to a positive value, then the laser triangulator selects the shutter speed to receive the most number of valid points. For manual control, this parameter must be set to 0 and the exposure time can be set using the `shuttertime:` (`-st`) parameter, which is measured in units of 10^{-5} s.

Measuring area

The rate at which the laser can record data is limited by the area over which it has to scan. Generally speaking, the smaller the area, the higher the bandwidth. This is set using the `measurearea:` (`-ma`) property. It can take the values shown in figure C.1. If a significant number of points is being reported as invalid, this field should be altered appropriately. It is suggested that, before performing an experiment, the user estimates the maxima and minima of distances to be measured to ensure that valid data is recorded for the duration.

Other switches

The fields for `name:` (`-nm`), `suffix:` (`-sf`) `seriesnumber:` (`-sn`) and `experimentnumber:` (`-nm`) should be self explanatory, and are used in the naming convention described in the previous appendix.

The fields `rate:` (`-rate`) and `resolution:` (`-res`) specify the rate and resolution of the profiles. The rate is any positive integer < 1000 and the resolution must be a power of 2 such that it is greater than 64 and less than 1024.

A note can be specified using the `note:` (`-no`) option for small amounts of important information to be stored.

Finally, a facility was added, whereby an LED attached to pins 4 and 5 of an RS232 serial port turns on when data is being recorded. This is set using the option `ledcom:` (`-led`).

A default settings file `settings.txt` is shown in table C.1 to illustrate the format required. By default, the program will look for this file, but other files can be specified using the input file command switch `-if`.

A summary of available parameters can be seen in table C.3, and their command line alternatives can be seen in table C.4.

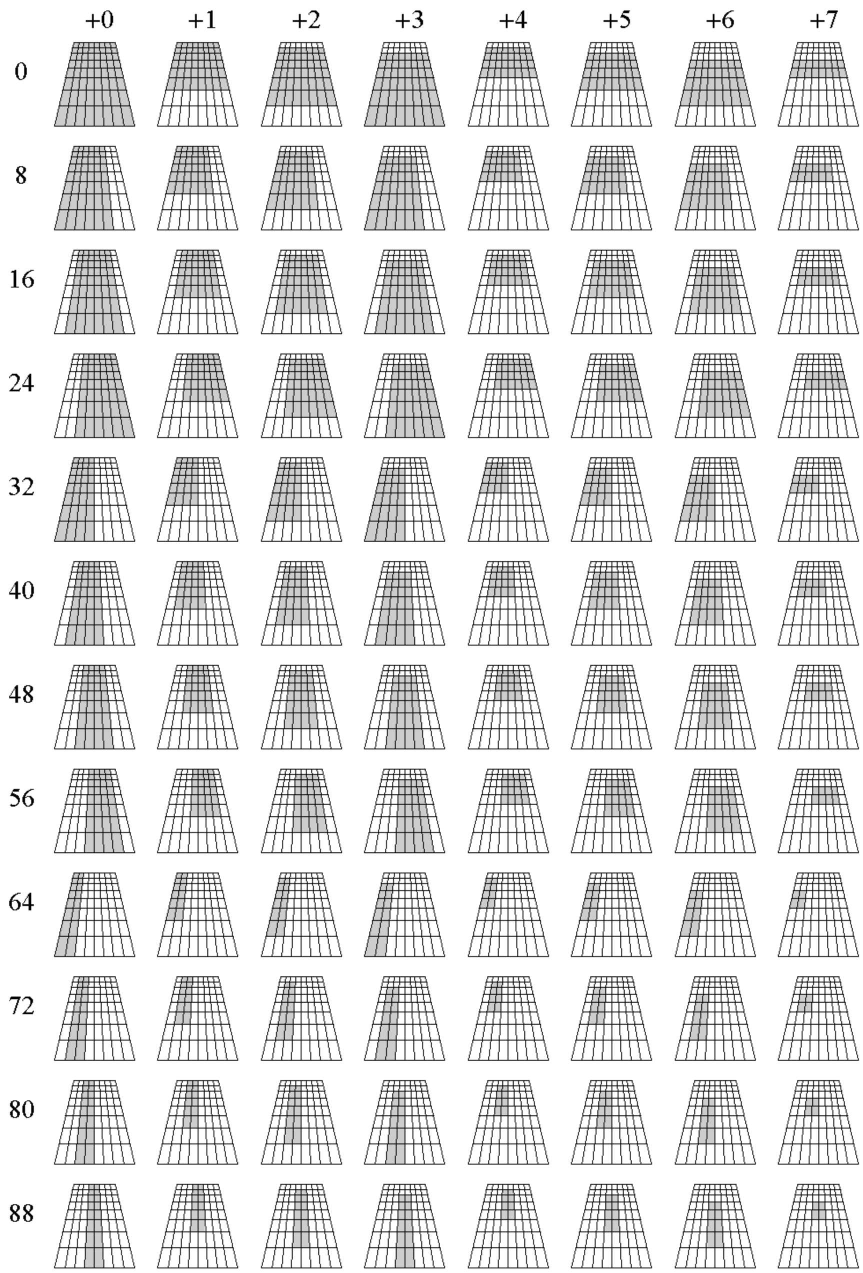

Figure C.1: *Measuring fields' codes for the laser.*

```
name: exciting_experiment
suffix: interesting_parameter
seriesnumber: 1
experimentnumber: 1
rate: 25
resolution: 1024
shuttertime: 500
average: 0
averagestart: -1
averageend: -1
containerheight: 64
numberofprofiles: 0
measurearea: 0
automatic: 0
autosecs: 1
ledcom: 0
note: ‘‘Details that you would forget otherwise’’
```

Table C.1: *Default* `settings.txt`

Table C.2: *Parameter description and units*

Parameter	range	description
name	$<$ 255 chars	Experiment Name
suffix	$<$ 255 chars	Measurement Type
seriesnumber	00 - 99	Experiment Series Number
experimentnumber	00 - 99	Subexperiment Number
rate	$<$ 1000	Number of profiles per second
resolution	2^n: $6 \leq n \leq 10$	Number of points per profile
shuttertime	depends on rate	Exposure time
average	1 or 0	Whether or not to average each profile
averagestart	0 - averageend	Point from which to average from
averageend	averagestart - resolution	Point from which to average to
containerheight	?	Number of profiles for laser to transmit to computer in packet (leave to default value)
numberofprofiles	≥ 0	How many profiles to capture ($0 = \infty$)
measurearea	0 - 95	Which area to measure - consult manual
automatic	0,1,2	See below
autosecs	$0 - \infty$	Time after signals stop to start capturing to another file and wait for another trigger
ledcom	0 - 1	Turn on an LED connected to COM2 when autosecs have expired
note	≤ 255	Note to put in header

Table C.3: *A reference table for laser scanner parameters.*

Switch	Parameter name
-nm	name
-sf	suffix
-if	input file (defaults to settings.txt)
-sn	seriesnumber
-en	experimentnumber
-rate	rate
-res	resolution
-st	shuttertime
-sa	shutter auto
-ap	average
-as	average start
-ae	average end
-ch	containerheight
-np	numberofprofiles
-no	note
-ma	measurearea
-am	automatic
-aus	autosecs
-led	led com
-h	print help

Table C.4: *Command line options for the laser scanner.*

D

Distance Ratio Method

In this appendix we present a brief summary of a method of segmenting grains in an image. As it was discovered that this method was not computationally efficient, it was discarded in favour of other methods. We examine the ratio of distance around the perimeter and the Euclidean distance between two points. We define the edge pixels of a cluster of grains as (x_i, y_i), where $1 \leq i \leq N$ and N is the perimeter length. We assume an 8-connected definition of an edge (i.e. include diagonal pixels) but the results remain qualitatively unchanged if a 4-connected definition is taken. The coordinates are ordered such that $|x_i - x_{i+1}| \leq \sqrt{2}$ and similarly for y.

We define

$$Q_{i,j} = \sum_{m=i}^{k} \sqrt{(x_{m+1} - x_m)^2 + (y_{m+1} - y_m)^2}, \tag{D.1}$$

where all suffices are taken modulo N. And k is defined so that it satisfies $k \equiv j-1 \pmod{N}$ and therefore $i < k < i + N$. Then, the *perimetric distance* is defined as

$$P_{i,j} = \min\{Q_{i,j}, Q_{j,i}\}. \tag{D.2}$$

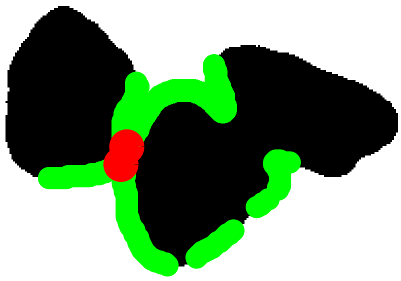

Figure D.1: *Points on boundary of clump of grains that are under the threshold. Red shows the point with the minimum value i.e. the point that the cluster will be split at.*

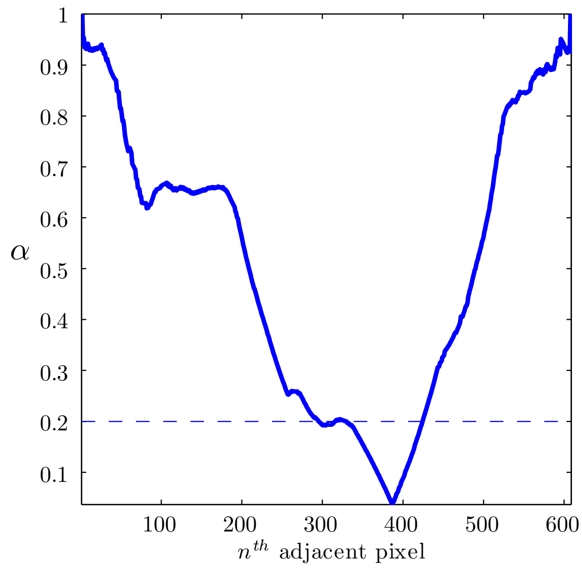

Figure D.2: *Ratio of distance to distance around perimeter of the pixel on the split point to the* n^{th} *pixel along the perimeter. The lowest value denotes the point at which to split the pixel. Dashed line indicates the value below which we choose to split the particle.*

This can be interpreted as the shortest distance between the i^{th} and j^{th} pixel around the perimeter. Then, using the conventional distance between the two points

$$D_{i,j} = \sqrt{(x_i - x_j)^2 - (y_i - y_j)^2}, \tag{D.3}$$

we construct the ratio

$$\alpha_{i,j} = \frac{D_{i,j}}{P_{i,j}}. \tag{D.4}$$

This ratio α is bounded above by 1 and below by 0. Low values are attained when there is a thin part of the shape with bulbous regions on either side. If a pair of points gives a particularly low value for this ratio, we split the shape in two between these points.

In order to do this sucessfully a threshold must be chosen such that if the minimum of α is below this threshold, we split the particles there. We see that for a circle, the minimum value attained by α is $1/\pi \approx 0.31$ hence choosing a number smaller than this will allow for some non circularity. Trial and error on a batch of images revealed that 0.2 produced a good level of segmentation for small clusters. A sample cluster and its split point can be seen in figure D.1.

Once a split point has been found for a cluster of grains, we then follow the same procedure on each of the new clusters. This process is then carried out until we reach a point where all clusters have no eligible candidate points on which to split the grains.

This approach to the problem works well if the clusters of particles have no more than around 10 particles in them. However, as the pictures usually have around 500 grains in them, there are clusters that have significantly more and therefore the recursive nature of the algorithm means that the computation time grows exponentially with the maximum cluster size. On a typical image the algorithm takes a prohibitively long time hence we elect to use one of the other techniques described in chapter 2.

Bibliography

Aharonov, E. & Sparks, D. 1999 Rigidity phase transition in granular packings. *Physical Review E* **60** (6), 6890.

Ahn, H. & Brennen, CE 1992 Channel flows of granular materials and their rheological implications. *Particulate Two-Phase Flow (ed. M. Roco). Butterworth-Heinemann* .

Ahn, H., Brennen, C.E. & Sabersky, R.H. 1991 Measurements of velocity, velocity fluctuation, density, and stresses in chute flows of granular materials. *Journal of Applied Mechanics* **58** (792), 12.

Ahn, H., Brennen, C.E. & Sabersky, R.H. 1992 Analysis of the fully developed chute flow of granular materials. *Journal of Applied Mechanics* **59**, 109.

Alam, M. & Hrenya, CM 2001 Inelastic collapse in simple shear flow of a granular medium. *Physical Review E* **63** (6), 061308.

Ancey, C. 2001 Dry granular flows down an inclined channel: Experimental investigations on the frictional-collisional regime. *Physical Review E* **65** (1), 011304.

Ancey, C., Coussot, P. & Evesque, P. 1999 A theoretical framework for granular suspensions in a steady simple shear flow. *Journal of Rheology* **43**, 1673.

ANDERSON, KG & JACKSON, R. 1992 A comparison of the solutions of some proposed equations of motion of granular materials for fully developed flow down inclined planes. *Journal of Fluid Mechanics* **241** (1), 145–168.

ARMSTRONG, B.R., WILLIAMS, K. & ARMSTRONG, R.L. 1992 *The avalanche book*. Fulcrum Publishing.

BAGNOLD, R.A. 1941 *The physics of blown sand and desert dunes.*. Methuen.

BARAN, O., ERTAŞ, D., HALSEY, T.C., GREST, G.S. & LECHMAN, J.B. 2006 Velocity correlations in dense gravity-driven granular chute flow. *Physical Review E* **74** (5), 051302.

BARDENHAGEN, SG, BRACKBILL, JU & SULSKY, D. 2000 Numerical study of stress distribution in sheared granular material in two dimensions. *Physical Review E* **62** (3), 3882.

BARTELT, P., SALM, B. & GRUBER, U. 1999 Calculating dense-snow avalanche runout using a Voellmy-fluid model with active/passive longitudinal straining. *Journal of Glaciology* **45** (150), 242–254.

BASSETT, D.S., OWENS, E.T., DANIELS, K.E. & PORTER, M.A. 2011 The influence of topology on signal propagation in granular force networks. *Arxiv preprint arXiv:1110.1858* .

BENEDETTO, D. & CAGLIOTI, E. 1999 The collapse phenomenon in one-dimensional inelastic point particle systems. *Physica D: Nonlinear Phenomena* **132** (4), 457–475.

VAN DEN BERG, EH, MEESTERS, A., KENTER, JAM & SCHLAGER, W. 2002 Automated separation of touching grains in digital images of thin sections. *Computers & geosciences* **28** (2), 179–190.

BERZI, D., DI PRISCO, CG & VESCOVI, D. 2011 Constitutive relations for steady, dense granular flows. *Physical Review E* **84** (3), 031301.

BEVERLOO, WA, LENIGER, HA & VAN DE VELDE, J. 1961 The flow of granular solids through orifices. *Chemical engineering science* **15** (3-4), 260–269.

Borgefors, G. 1986 Distance transformations in digital images. *Computer vision, graphics, and image processing* **34** (3), 344–371.

Börzsönyi, T. & Ecke, R.E. 2006 Rapid granular flows on a rough incline: Phase diagram, gas transition, and effects of air drag. *Physical Review E* **74** (6), 061301.

Börzsönyi, T., Ecke, R.E. & McElwaine, J.N. 2009 Patterns in Flowing Sand: Understanding the Physics of Granular Flow. *Physical review letters* **103** (17), 178302.

Brown, RL & Richards, J.C. 1970 *Principles of powder mechanics*. Pergamon press.

Campbell, C.S. 1990 Rapid granular flows. *Annual Review of Fluid Mechanics* **22** (1), 57–90.

Campbell, C.S. 2002 Granular shear flows at the elastic limit. *Journal of fluid mechanics* **465**, 261–291.

Chang, H.C. & Demekhin, E.A. 2002 *Complex wave dynamics on thin films*. Elsevier.

Chapman, S. & Cowling, TG 1939 The mathematical theory of non-uniform gases.

Chevoir, F., Prochnow, M., Moucheront, P., da Cruz, F., Bertrand, F., Guilbaud, J.P., Coussot, P. & Roux, J.N. 2001 Dense granular flows in a vertical chute. *Powder and Grains* pp. 399–402.

Cho, G.C., Dodds, J. & Santamarina, J.C. 2006 Particle shape effects on packing density, stiffness, and strength: natural and crushed sands. *Journal of Geotechnical and Geoenvironmental Engineering* **132**, 591.

van Cleef, J. 1991 Powder technology. *American Scientist* **79** (4), 304–315.

de Coulomb, C.-A. 1773 *Mémoires de mathématique et de physique*, , vol. 7. Académie Royale des Sciences (France) and Imprimerie Royale (France).

DA CRUZ, F., EMAM, S., PROCHNOW, M., ROUX, J.N. & CHEVOIR, F. 2005 Rheophysics of dense granular materials: Discrete simulation of plane shear flows. *Physical Review E* **72** (2), 21309.

DEBOEUF, S., DAUCHOT, O., STARON, L., MANGENEY, A. & VILOTTE, J.P. 2005 Memory of the unjamming transition during cyclic tiltings of a granular pile. *Physical Review E* **72** (5), 051305.

DEBOEUF, S., LAJEUNESSE, E., DAUCHOT, O. & ANDREOTTI, B. 2006 Flow rule, self-channelization, and levees in unconfined granular flows. *Physical review letters* **97** (15), 158303.

DELANNAY, R., LOUGE, M., RICHARD, P., TABERLET, N. & VALANCE, A. 2007 Towards a theoretical picture of dense granular flows down inclines. *Nature Materials* **6** (2), 99–108.

DENLINGER, R.P. & IVERSON, R.M. 2004 Granular avalanches across irregular three-dimensional terrain: 1. theory and computation. *Journal of geophysical research* **109** (F1), F01014.

DOUADY, S., ANDREOTTI, B. & DAERR, A. 1999 On granular surface flow equations. *The European Physical Journal B-Condensed Matter and Complex Systems* **11** (1), 131–142.

DRAKE, TG 1991 Granular flow: Physical experiments and their implications for microstructural theories. *Journal of Fluid Mechanics* **225**, 121–152.

DURAN, J. 2000 *Sands, powders, and grains: an introduction to the physics of granular materials*. Springer Verlag.

ECKART, W., GRAY, J. & HUTTER, K. 2003 Particle image velocimetry (piv) for granular avalanches on inclined planes. *Dynamic response of granular and porous material under large and catastrophic deformations Hutter K, Kirchner N Lecture Notes in Applied & Computational Mechanics* **11**, 195–218.

ERTAŞ, D., GREST, G.S., HALSEY, T.C., LEVINE, D. & SILBERT, L.E. 2001 Gravity-driven dense granular flows. *EPL (Europhysics Letters)* **56**, 214.

Faraday, M. 1831 On a peculiar class of acoustical figures; and on certain forms assumed by groups of particles upon vibrating elastic surfaces. *Philosophical Transactions of the Royal Society of London* **121**, 299–340.

Forterre, Y. 2006 Kapiza waves as a test for three-dimensional granular flow rheology. *Journal of Fluid Mechanics* **563**, 123–132.

Forterre, Y. & Pouliquen, O. 2001 Longitudinal vortices in granular flows. *Physical Review Letters* **86** (26), 5886–5889.

Forterre, Y. & Pouliquen, O. 2002 Stability analysis of rapid granular chute flows: formation of longitudinal vortices. *Journal of Fluid Mechanics* **467** (1), 361–387.

Forterre, Y. & Pouliquen, O. 2003 Long-surface-wave instability in dense granular flows. *Journal of Fluid Mechanics* **486** (-1), 21–50.

Forterre, Y. & Pouliquen, O. 2008 Flows of dense granular media. *Annu. Rev. Fluid Mech.* .

de Gennes, P.G. 1999 Granular matter: a tentative view. *Reviews of modern physics* **71** (2), 374–382.

Goldhirsch, I. 2003 Rapid granular flows. *Annual review of fluid mechanics* **35**, 267–293.

Goldhirsch, I. & Zanetti, G. 1993 Clustering instability in dissipative gases. *Physical review letters* **70** (11), 1619–1622.

Grant, I. 1997 Particle image velocimetry: a review. *Proceedings of the Institution of Mechanical Engineers. Part C. Mechanical engineering science* **211** (1), 55–76.

Gray, J. 2001 Granular flow in partially filled slowly rotating drums. *Journal of Fluid Mechanics* **441** (4), 1–29.

Gray, J. & Kokelaar, BP 2010 Large particle segregation, transport and accumulation in granular free-surface flows. *Journal of Fluid Mechanics* **652**, 105–137.

Gray, J., Tai, Y.C. & Noelle, S. 2003 Shock waves, dead zones and particle-free regions in rapid granular free-surface flows. *Journal of Fluid Mechanics* **491** (1), 161–181.

Gray, J. & Thornton, AR 2005 A theory for particle size segregation in shallow granular free-surface flows. *Proceedings of the Royal Society A: Mathematical, Physical and Engineering Science* **461** (2057), 1447–1473.

Gray, J., Wieland, M. & Hutter, K. 1999 Gravity-driven free surface flow of granular avalanches over complex basal topography. *Proceedings of the Royal Society of London. Series A: Mathematical, Physical and Engineering Sciences* **455** (1985), 1841.

Greve, R. & Hutter, K. 1993 Motion of a granular avalanche in a convex and concave curved chute: experiments and theoretical predictions. *Philosophical Transactions of the Royal Society of London. Series A: Physical and Engineering Sciences* **342** (1666), 573–600.

Gui, L. & Merzkirch, W. 2000 A comparative study of the mqd method and several correlation-based piv evaluation algorithms. *Experiments in fluids* **28** (1), 36–44.

Haff, PK 1983 Grain flow as a fluid-mechanical phenomenon. *Journal of Fluid Mechanics* **134**, 401–30.

Hanes, D.M. & Walton, O.R. 2000 Simulations and physical measurements of glass spheres flowing down a bumpy incline. *Powder technology* **109** (1), 133–144.

Harris, C. & Stephens, M. 1988 A combined corner and edge detector. In *Alvey vision conference*, , vol. 15, p. 50. Manchester, UK.

Hogg, AJ, Gray, J. & Cui, X. 2005 Granular vacua. *Powders and Grains* .

Holmes, A. 1930 *Petrographic methods and calculations with some examples of results achieved*. T. Murby.

Holyoake, A.J. & McElwaine, J.N. 2011 High-speed granular flows. Under review.

Hunger, O. & Morgenstern, NR 1984 High velocity ring shear tests on sand. *Geotechnique* **34** (3), 415–421.

Hutter, K. & Rajagopal, KR 1994 On flows of granular materials. *Continuum Mechanics and Thermodynamics* **6** (2), 81–139.

Hutter, K., Siegel, M., Savage, SB & Nohguchi, Y. 1993 Two-dimensional spreading of a granular avalanche down an inclined plane part i. theory. *Acta mechanica* **100** (1), 37–68.

Jackson, R. 1983 Some mathematical and physical aspects of continuum models for the motion of granular materials. In *Theory of dispersed multiphase flow* (ed. R.E. Meyer). Academic Press.

Jaeger, HM, Liu, C. & Nagel, S.R. 1989 Relaxation at the angle of repose. *Physical Review Letters* **62** (1), 40–43.

Jaeger, H.M., Nagel, S.R. & Behringer, R.P. 1996 Granular solids, liquids, and gases. *Reviews of Modern Physics* **68** (4), 1259–1273.

Janssen, HA 1895 Tests on grain pressure silos. *Zeits. d. Vereins Deutsch Ing* **39** (35), 1045–9.

Jenkins, JT 1992 Boundary conditions for rapid granular flow: flat, frictional walls. *Journal of applied mechanics* **59**, 120.

Jenkins, J. 2001 Boundary conditions for collisional grain flows at bumpy, frictional walls. *Granular gases* pp. 125–139.

Jenkins, J.T. 2006 Dense shearing flows of inelastic disks. *Physics of Fluids* **18**, 103307.

Jenkins, J.T. 2007 Dense inclined flows of inelastic spheres. *Granular Matter* **10** (1), 47–52.

Jenkins, J.T. & Berzi, D. 2010 Dense inclined flows of inelastic spheres: tests of an extension of kinetic theory. *Granular Matter* **12** (2), 151–158.

Jenkins, JT & Richman, MW 1985 Kinetic theory for plane flows of a dense gas of identical, rough, inelastic, circular disks. *Physics of Fluids* **28**, 3485.

Jenkins, JT & Savage, SB 1983 Theory for the rapid flow of identical, smooth, nearly elastic, spherical particles. *Journal of Fluid Mechanics* **130** (1), 187–202.

Johnson, C.G. & Gray, J.M.N.T. 2011 Granular jets and hydraulic jumps on an inclined plane. *Journal of Fluid Mechanics* **675** (1), 87–116.

Johnson, PC, Nott, P. & Jackson, R. 1990 Frictional-collisional equations of motion for particulate flows and their application to chutes. *J. Fluid Mech* **210**, 501–535.

Jop, P., Forterre, Y. & Pouliquen, O. 2005 Crucial role of sidewalls in granular surface flows: consequences for the rheology. *Journal of Fluid Mechanics* **541**, 167–192.

Jop, Pierre, Forterre, Yoel & Pouliquen, Olivier 2006 A constitutive law for dense granular flows. *Nature* **441**.

Kennedy, SK & Mazzullo, J. 1991 Image analysis method of grain size measurement. *Principles, methods, and application of particle size analysis* pp. 76–87.

Klaucke, I., Masson, D.G., Kenyon, N.H. & Gardner, J.V. 2004 Sedimentary processes of the lower monterey fan channel and channel-mouth lobe. *Marine geology* **206** (1-4), 181–198.

Komatsu, T.S., Inagaki, S., Nakagawa, N. & Nasuno, S. 2001 Creep motion in a granular pile exhibiting steady surface flow. *Physical review letters* **86** (9), 1757–1760.

Leighton, D. & Acrivos, A. 1987 The shear-induced migration of particles in concentrated suspensions. *Journal of Fluid Mechanics* **181** (1), 415–439.

Lois, Gregg, Lemaître, Anaël & Carlson, Jean M. 2005 Numerical tests of constitutive laws for dense granular flows. *Phys. Rev. E* **72** (5), 051303.

Louge, MY 2009 The significance of fundamental granular materials research to space exploration.

Louge, M.Y. & Keast, S.C. 2001 On dense granular flows down flat frictional inclines. *Physics of Fluids* **13**, 1213.

Lun, C.K.K. & Savage, SB 1986 The effects of an impact velocity dependent coefficient of restitution on stresses developed by sheared granular materials. *Acta Mechanica* **63** (1), 15–44.

Lun, CKK, Savage, SB, Jeffrey, DJ & Chepurniy, N. 1984 Kinetic theories for granular flow: inelastic particles in couette flow and slightly inelastic particles in a general flowfield. *Journal of Fluid Mechanics* **140** (1), 223–256.

Lun, C. K. K. & Savage, S. B. 1987 A simple kinetic theory for granular flow of rough, inelastic, spherical particles. *Journal of Applied Mechanics* **54** (1), 47–53.

Mac Namara, S. & Young, WR 1992 Inelastic collapse and dumping in a one-dimensional granular medium. *Phys. Fluids* **4**, 496.

Mangeney, A., Bouchut, F., Thomas, N., Vilotte, JP & Bristeau, MO 2007 Numerical modeling of self-channeling granular flows and of their levee-channel deposits. *J. Geophys. Res* **112**.

Mangeney-Castelnau, A., Vilotte, JP, Bristeau, MO, Perthame, B., Bouchut, F., Simeoni, C. & Yerneni, S. 2003 Numerical modeling of avalanches based on saint-venant equations using a kinetic scheme. *J. Geophys. Res* **108** (2527), 4.

McNamara, S. & Young, WR 1994 Inelastic collapse in two dimensions. *Physical Review E* **50**, 28–31.

Meyer, F. 1994 Topographic distance and watershed lines. *Signal Processing* **38** (1), 113–125.

MiDi, GDR 2004 On dense granular flows. *The European Physical Journal E: Soft Matter and Biological Physics* **14** (4), 341–365.

Nakagawa, M., Altobelli, SA, Caprihan, A., Fukushima, E. & Jeong, E.K. 1993 Non-invasive measurements of granular flows by magnetic resonance imaging. *Experiments in fluids* **16** (1), 54–60.

Nedderman, R.M. 2005 *Statics and kinematics of granular materials*. Cambridge Univ Press.

Nedderman, RM, Tuzun, U., Savage, SB & Houlsby, GT 1982 The flow of granular materials–i:: Discharge rates from hoppers. *Chemical Engineering Science* **37** (11), 1597–1609.

Ogawa, S., Umemura, A. & Oshima, N. 1980 On the equations of fully fluidized granular materials. *Zeitschrift für Angewandte Mathematik und Physik (ZAMP)* **31** (4), 483–493.

Patton, JS, Brennen, CE & Sabersky, RH 1987 Shear flows of rapidly flowing granular materials. *Journal of Applied Mechanics* **54**, 801.

Phillips, R.J., Armstrong, R.C., Brown, R.A., Graham, A.L. & Abbott, J.R. 1992 A constitutive equation for concentrated suspensions that accounts for shear-induced particle migration. *Physics of Fluids A: Fluid Dynamics* **4**, 30.

Pouliquen, O. 1999*a* On the shape of granular fronts down rough inclined planes. *Physics of Fluids* **11**, 1956.

Pouliquen, O. 1999*b* Scaling laws in granular flows down rough inclined planes. *Physics of fluids* **11**, 542.

Pouliquen, O., Cassar, C., Jop, P., Forterre, Y. & Nicolas, M. 2006 Flow of dense granular material: towards simple constitutive laws. *Journal of Statistical Mechanics: Theory and Experiment* **2006**, P07020.

Pouliquen, O., Delour, J. & Savage, SB 1997 Fingering in granular flows. *Nature* .

POULIQUEN, O. & FORTERRE, Y. 2002 Friction law for dense granular flows: application to the motion of a mass down a rough inclined plane. *Journal of Fluid Mechanics* **453**, 133–151.

POULIQUEN, O. & FORTERRE, Y. 2009 A non-local rheology for dense granular flows. *Philosophical Transactions of the Royal Society A: Mathematical, Physical and Engineering Sciences* **367** (1909), 5091.

POULIQUEN, O., FORTERRE, Y & ST PHANE, L.E.D. 2002 Slow dense granular flows as a self induced process. *Challenges in granular physics* p. 153.

POULIQUEN, O. & RENAUT, N. 1996 Onset of granular flows on an inclined rough surface: dilatancy effects. *Journal de Physique II* **6** (6), 923–935.

RAJCHENBACH, J. 2003 Dense, rapid flows of inelastic grains under gravity. *Physical review letters* **90** (14), 144302.

RANKINE, W.J.M. 1857 On the stability of loose earth. *Philosophical Transactions of the Royal Society of London* pp. 9–27.

REYNOLDS, O. 1885 On the dilatancy of media composed of rigid particles in contact. *Philos. Mag. Ser. 5* **50**.

ROUX, J.N. & COMBE, G. 2002 Quasistatic rheology and the origins of strain. *Comptes Rendus Physique* **3** (2), 131–140.

RUSS, J.C. 2002 *The image processing handbook*. CRC Pr I Llc.

DE SAINT-VENANT, AJC 1871 Théorie du mouvement non-permanent des eaux, avec application aux crues des rivières et á l'introduction de marés dans leurs lit. *Comptes rendus des seances de l'Academie des Sciences* **36**, 174–154.

SAVAGE, S.B. 1979 Gravity flow of cohesionless granular materials in chutes and channels. *J. Fluid Mech* **92** (1), 53–96.

SAVAGE, S.B. 1984 The mechanics of rapid granular flows. *Advances in applied mechanics* **24**, 289–366.

Savage, SB & Hutter, K. 1989 The motion of a finite mass of granular material down a rough incline. *Journal of Fluid Mechanics* **199** (-1), 177–215.

Savage, SB & Hutter, K. 1991 The dynamics of avalanches of granular materials from initiation to runout. part i: Analysis. *Acta Mechanica* **86** (1), 201–223.

Schaeffer, D.G. 1987 Instability in the evolution equations describing incompressible granular flow. *Journal of differential equations* **66** (1), 19–50.

Schofield, A.N. & Wroth, P. 1968 *Critical state soil mechanics*, , vol. 1968. McGraw-Hill London.

Silbert, L.E., Ertaş, D., Grest, G.S., Halsey, T.C., Levine, D. & Plimpton, S.J. 2001 Granular flow down an inclined plane: Bagnold scaling and rheology. *Physical Review E* **64** (5), 51302.

Silbert, L.E., Landry, J.W. & Grest, G.S. 2003 Granular flow down a rough inclined plane: transition between thin and thick piles. *Physics of Fluids* **15**, 1.

Sveen, J. K. & Dalziel, S. B. 2005 A dynamic masking technique for combined measurements of PIV and synthetic schlieren applied to internal gravity waves. *Measurement Science and Technology* **16**, 1954–1960.

Taberlet, N., Richard, P., Jenkins, JT & Delannay, R. 2007 Density inversion in rapid granular flows: the supported regime. *The European Physical Journal E* **22** (1), 17–24.

Taberlet, N., Richard, P., Valance, A., Losert, W., Pasini, J.M., Jenkins, J.T. & Delannay, R. 2003 Superstable granular heap in a thin channel. *Physical review letters* **91** (26), 264301.

Tan, ML & Goldhirsch, I. 1997 Intercluster interactions in rapid granular shear flows. *Physics of Fluids* **9**, 856.

Thompson, P.A. & Grest, G.S. 1991 Granular flow: friction and the dilatancy transition. *Physical review letters* **67** (13), 1751–1754.

TREIMAN, AH & LOUGE, MY 2004 Martian slope streaks and gullies: Origins as dry granular flows. In *Lunar and Planetary Institute Science Conference Abstracts*, , vol. 35, p. 1323.

VOIGHT, B., JANDA, RJ, GLICKEN, H. & DOUGLASS, PM 1985 Nature and mechanics of the mount st. helens rockslide-avalanche of 18 may 1980. In *The 26th US Symposium on Rock Mechanics (USRMS)*.

WHITE, DJ 2003 PSD measurement using the single particle optical sizing (SPOS) method. *Géotechnique* **53** (3), 317–326.

WHITE, F.M. 1991 *Viscous fluid flow*, , vol. 66. McGraw-Hill New York.

WILLERT, C., RAFFEL, M., KOMPENHANS, J., STASICKI, B. & KÄHLER, C. 1996 Recent applications of particle image velocimetry in aerodynamic research. *Flow Measurement and Instrumentation* **7** (3-4), 247–256.

WOODHOUSE, M.J., HOGG, A.J. & SELLAR, A.A. 2010 Rapid granular flows down inclined planar chutes. part 1. steady flows, multiple solutions and existence domains. *Journal of Fluid Mechanics* **652** (1), 427–460.